

MASARYK UNIVERSITY
FACULTY OF SCIENCE

Ph.D. Thesis

BRNO 2019

JAN BENÁČEK

MASARYK UNIVERSITY

FACULTY OF SCIENCE

DEPARTMENT OF THEORETICAL PHYSICS AND ASTROPHYSICS

Particle-in-cell simulations and analytical study of the processes generating radio solar bursts

Ph.D. Thesis

Jan Benáček

Supervisor: prof. RNDr. Marian Karlický, DrSc.

Brno 2019

Bibliographic Entry

Author:	Jan Benáček Faculty of Science, Masaryk University Department of Theoretical Physics and Astrophysics
Title of Thesis:	Particle-in-cell simulations and analytical study of the processes generating radio solar bursts
Degree Programme:	Physics
Field of Study:	Theoretical Physics and Astrophysics
Supervisor:	prof. RNDr. Marian Karlický, DrSc.
Academic Year:	2018/2019
Number of Pages:	128
Keywords:	Sun; Radio zebras; Double plasma resonance; Particle-in-cell

Bibliografický záznam

Autor:	Jan Benáček Přírodovědecká fakulta, Masarykova univerzita Ústav teoretické fyziky a astrofyziky
Název práce:	Particle-in-cell simulace a analytická studie procesů generujících sluneční rádiové bursty
Studijní program:	Fyzika
Studijní obor:	Teoretická fyzika a astrofyzika
Vedoucí práce:	prof. RNDr. Marian Karlický, DrSc.
Akademický rok:	2018/2019
Počet stran:	128
Klíčová slova:	Slunce; Rádiové zebry; Dvojná plazmová nestabilita; Particle-in-cell

Abstract

Solar radio bursts with fine structures are used in diagnostics of the solar flare plasma. The zebra structures, that are fine structures of Type IV radio bursts, belong to the most important. The zebras are also observed in radiation from Jupiter and Crab nebula pulsar. In this doctoral thesis, we study the solar radio zebras from the theoretical point of view. We use analytical and numerical methods together with the three-dimensional electromagnetic particle-in-cell (PIC) simulations. This thesis starts with an overview of solar radio bursts and their characteristics. We describe the models of the solar radio zebras and present details of our improvement of the PIC model. We study various aspects of the main model of the solar radio zebras, the double plasma resonance instability. This model assumes a loss-cone type of distributions of the hot electron component together with a cold and dense background plasma. We mainly study the growth rates of the electrostatic waves, their saturation energies, and the frequency shifts of the growth rate peaks in dependence on the temperature of the background and the hot component. Our results are compared with zebra observations. Because in the upper-hybrid band, several types of waves can be unstable simultaneously, we propose a concept of the integrated growth rate, which is useful for comparison with the growth rate computed by the PIC model. Our results are published in *Solar Physics*, *Astronomy and Astrophysics*, and *Astrophysical Journal*, see our five papers at the end of this thesis.

Abstrakt

Sluneční radiová vzplanutí s jemnými strukturami se používají v diagnostice slunečního erupčního plazmatu. Zebra struktury, které jsou jemnými strukturami radiových vzplanutí typu IV, patří mezi nejdůležitější. Zebry jsou také pozorovány v záření Jupitera a pulzaru v Krabí mlhovině. V této doktorské práci studujeme sluneční rádiové zebry z teoretického hlediska. Používáme analytické a numerické metody společně s třídimenzionálním elektromagnetickým částicovým modelem. Práce začíná přehledem slunečních rádiových vzplanutí a jejich charakteristikami. Popisujeme modely slunečních rádiových zeber a prezentujeme vylepšení částicového modelu. Studujeme různé aspekty hlavního modelu slunečních rádiových zeber, dvojnou plazmovou nestabilitu. Tento model předpokládá horké elektrony s distribuční funkcí s únikovým kuželem společně s chladnou a hustou pozadovou plazmou. Studujeme zejména rychlost růstů energií elektrostatických vln, jejich saturační energie a frekvenční posuny maxim rychlostí růstů v závislosti na teplotě pozadové i horké komponenty. Naše výsledky jsou porovnány s pozorováním zeber. Protože v pásmu horně-hybridních vln může být několik nestabilních typů vln současně, navrhujeme koncept integrované rychlosti růstu, která je užitečná pro srovnání s rychlostí růstu, která je počítána částicovým modelem. Naše výsledky jsou publikovány v Solar Physics, Astronomy and Astrophysics, a Astrophysical Journal, viz pět našich prací v závěru této dizertace.

Acknowledgment

I would like to thank my family and friends for sustained support, my supervisor prof. RNDr. Marian Karlický, DrSc. for all the four years of collaboration and effective consultations, very quick responses to my questions and for the help with improvement of this thesis. I would like also to thank my non-official consultant Mgr. Miroslav Bárta, Ph.D. for the help with the PIC model improvements and the support during the conferences and workshops.

Contents

List of Publications	xiii
Introduction	xv
Symbols	xvii
Chapter 1. Solar Radio Emission	1
1.1 Radio emission mechanisms	3
1.1.1 Plasma emission	3
1.1.2 Gyrosynchrotron emission	5
1.2 Solar radio bursts	6
1.2.1 Type I bursts	7
1.2.2 Type II bursts	7
1.2.3 Type III bursts	8
1.2.4 Type IV bursts	9
1.2.5 Type V bursts	10
1.3 Fine structure radio bursts	10
1.3.1 Pulsations	11
1.3.2 Spike bursts	11
1.3.3 Fiber Bursts	11
1.3.4 Zebra pattern	13
Chapter 2. Solar Radio Zebra Models	17
2.1 The Double Plasma Resonance Instability Model	17
2.2 Whistler Generation Model	20
2.3 MHD Waves Model	21
2.4 Eigenfrequencies (Trapped Plasma Waves) Model	21
2.5 Interference Model	22
Chapter 3. Particle-in-Cell Model	25
3.1 Model Workflow	27
3.1.1 Field updates	30
3.1.2 Particle update	30
3.1.3 Current decomposition	32
3.1.4 Boundary conditions	32
3.1.5 Data storage	33
3.2 Domain Parallelisation and Other Code Improvements	33

3.3 Proposed future development	35
Chapter 4. Summary of my Results	37
4.1 Paper I: Temperature Dependent Growth Rates of the Upper-hybrid Waves and Solar Radio Zebra Patterns	37
4.2 Paper II: Brightness Temperature of Radio Zebras and Wave Energy Densities in Their Sources	39
4.3 Paper III: Double Plasma Resonance Instability as a Source of Solar Zebra Emission	40
4.4 Paper IV: Growth Rates of the Upper-Hybrid Waves for Power-Law and Kappa Distributions with a Loss-Cone Anisotropy	41
4.5 Paper V: Growth Rates of the Electrostatic Waves in Radio Zebra Models	43
Conclusions	45
Appendix A	47
Appendix B	55
Appendix C	69
Appendix D	79
Appendix E	95
References	105

List of Publications

Temperature dependent growth rates of the upper-hybrid waves and solar radio zebra patterns

J. Benáček, M. Karlický, L.V. Yasnov

Astronomy & Astrophysics, **598**, A106, (2017)

JB implemented the analytical equation, computed the growth rate, prepared the figures, participated in the writing of the manuscript and submitted the paper.

Brightness temperature of radio zebras and wave energy densities in their sources

L.V. Yasnov, **J. Benáček**, M. Karlický

Solar Physics, **292**, 163, (2017)

JB computed the saturation energies and energy transfer ratios, contributed to the manuscript preparation and submitted the paper.

Double plasma resonance instability as a source of solar zebra emission

J. Benáček, M. Karlický

Astronomy & Astrophysics, **611**, A60, (2018)

JB implemented the double plasma instability using PIC code, computed the instability for variety of parameters, analyzed the model results, prepared the figures, participated in the manuscript preparation and submitted the paper.

Growth rates of the upper-hybrid waves for power-law and kappa distributions with a loss-cone anisotropy

L.V. Yasnov, **J. Benáček**, M. Karlický, M.

Solar Physics, **294**, 29, (2019)

JB contributed to the manuscript preparation, the result discussion, and submitted the paper.

Growth rates of the electrostatic waves in radio zebra models

J. Benáček, M. Karlický

Astrophysical Journal, **881**, 21, (2019)

JB implemented the analytical equations, analytically computed the growth rates, developed an algorithm for the search of dispersion branches, prepared the figures, participated in the manuscript preparation and submitted the paper.

Introduction

Solar flares are the most energetic events in our Solar system, during which the energy can be released in the range $10^{30} - 10^{32}$ erg. This energy is released by a process called magnetic reconnection. Magnetic reconnection generally occurs when the oppositely directed magnetic field lines interact with others. They are dynamically changing their internal structure, and they are reconnecting towards the lower internal energy state. The energy difference is released in the form of the plasma heating, particle acceleration, plasma flows, waves and emission in the radio, optical, ultraviolet, soft and hard X-rays, and, in some cases, γ -rays. During the solar flares, the coronal mass ejections (CME) and the solar energetic particle events (SEPs) often occur. Both propagate through our heliosphere and, in some cases, they can reach the Earth, where they can damage satellites or electrical devices.

The solar radio bursts are observed during and after the solar flares. Because their radio flux is higher than the thermal radiation from the solar atmosphere, they are easily distinguishable. The radio bursts were originally divided into five types, according to their time after the start of the flare, their frequency range and the shape in the radiogram. They are broadband or narrowband. The narrowband are mainly fine structure bursts generated by the plasma emission mechanisms. They can help understand and diagnose the plasma during the flare.

The radio zebra structure is one of the most useful fine structures for a solar flare diagnostics. In the radio spectra, the zebras are formed by the simultaneously excited parallel emission stripes at nearly equidistant frequencies (Slotte, 1972, Chernov et al., 2012, Tan et al., 2012, 2014). There are many models of the radio fine structures (Rosenberg & Tarnstrom, 1972, Kuijpers, 1975, Zhelezniakov & Zlotnik, 1975a,c, Chernov, 1976, 1990, LaBelle et al., 2003, Bárta & Karlický, 2006, Ledenev et al., 2006, Kuznetsov & Tsap, 2007, Laptukhov & Chernov, 2009, Tan, 2010, Karlický, 2013). For more details, see the reviews by Zhelezniakov (1997) Chernov (2010), Chernov et al. (2014), Zheleznyakov et al. (2016), and Chernov et al. (2018). Among these models, the most commonly used model is based on the double plasma resonance (DPR), see for example Zheleznyakov et al. (2016).

In this thesis, we extend the double plasma resonance model from previous papers (Winglee & Dulk, 1986, Yasnov & Karlický, 2004) by many aspects. We compute the growth rates of the upper-hybrid and general electrostatic waves using the analytical theory and particle-in-cell (PIC) model. We use the Dory, Guest, & Harris (1965) (DGH), loss-cone kappa and power-law velocity distribution functions of the hot electrons. We also compute the saturation energies of the electrostatic waves. We analyze the growth rate peaks, their frequency shifts, and the dependency on the hot electrons and the background plasma temperatures. Based on the observation, the particle-in-cell simulation and the collisional damping, we estimate the efficiency of the transformation of the electrostatic waves into the electromagnetic radiation. Because in the double plasma resonance, many unstable waves can exist simultaneously, we analyze their growth rates. We propose the concept of the branch frequency “specific width” and the integrated growth rate that is in the agreement with the particle-in-cell simulations.

Thus, the obtained results are important not only for the study of the solar radio zebras and the double plasma resonance instability but also for the diagnostics of the solar flares, planetary atmospheres, and the laboratory plasma.

This thesis is structured as follows: first, used symbols are presented. In Chapter 1, we start with an introduction of the solar radio observations, solar radio bursts, and solar radio zebras. In Chapter 2, we present the radio zebra formation models, especially the double plasma resonance. Because one of the aims of this thesis was a parallelization of the particle-in-cell code in domains, details about the model itself and its improvements are in Chapter 3. A summary of our publications is in Chapter 4. The work is supplemented by Appendixes A–E, where our papers are presented.

Symbols

For better orientation in the text, we propose these mathematical symbols. They are used for description in the whole thesis. Because in the attached articles in Appendixes the symbol notation may differ, to avoid the mistakes, please, always check the current notation in each paper.

B	magnetic field
c	light speed
c_s	sound speed
e	electron charge
E	electric field
f	particle velocity distribution function
H	magnetic induction
i	imaginary unit
J	electric current
k	wave vector
l_w	length of absorption of whistler wave
m_e	electron mass
m_i	ion mass
n_b	electron beam density
n_e	electron density
n_h	hot electron density
n_σ	refractive index
P	period of oscillations
q	electric charge
r	position vector
s	harmonic number
T_b	brightness temperature
v	velocity vector
v_b	electron beam velocity
v_t	hot electron velocity
v_{tb}	background electron thermal velocity
Z	plasma function
v_ϕ	wave phase velocity
δ_{ij}	Kronecker delta
$\hat{\epsilon}$	permittivity tensor
ϵ_{ij}	components of permittivity tensor
ϵ_0	permittivity of vacuum
ϕ	electric potential

γ	growth rate
γ_{rel}	relativistic factor
γ_{σ}	absorption coefficient
Γ	integrated growth rate
λ_D	Debye shielding length
Λ	Coulomb logarithm
ω	frequency
ω_{pe}	plasma electron frequency
ω_{ce}	electron-cyclotron frequency
θ	loss-cone angle

Chapter 1

Solar Radio Emission

The facilities of the ground-based radio astronomical observations, like in optical observations, depend on the transparency of the Earth's atmosphere. For the cosmic radio waves, this frequency range is 15 MHz – 30 GHz (Kruger, 1979). The low-frequency limit is caused by the ionosphere and the high-frequency limit by the troposphere. In some special Earth's locations, this range is extended due to the low air humidity. E.g. ALMA is using its Bands 3-10 in range 84-950 GHz (ESO, 2019).

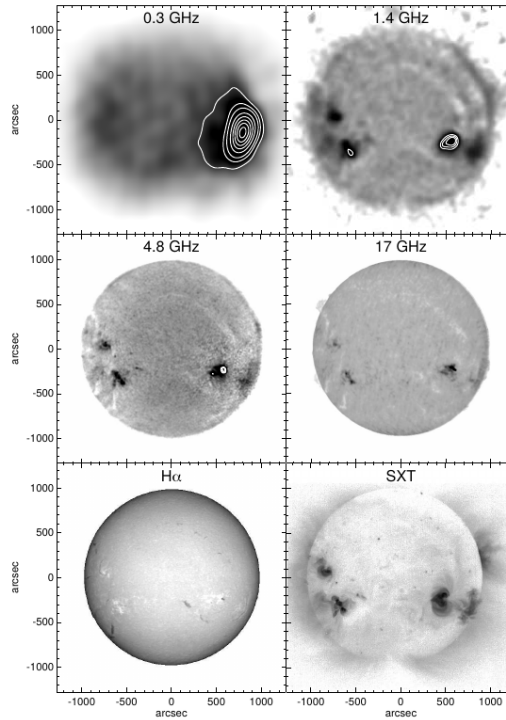


Figure 1.1: The Sun at different wavelengths on 7 November 1993. The resolutions are $220''$ at 0.3 GHz, $50''$ at 1.4 GHz, $12''$ at 4.8 GHz and 17 GHz. The 0.3–4.8 GHz are from Very Large Array telescope, 17 GHz is from Nobeyama Radioheliograph. White contours are brightness temperatures in the range $0.8\text{--}4.5 \times 10^6$ K. The bottom row is the comparison with $H\alpha$ from Big Bear Solar Observatory and X-Rays from Yohkoh/SXT instrument. The figure was taken from White (2001).

The observed wavelength strictly limits the spatial resolution of the solar observation. The sample of the radio observations is in range 0.3–17 GHz, $H\alpha$, and X-rays in Figure 1.1. The largest interferometric and spectroscopic instruments with not only solar targets include:

- Atacama Large Millimeter Array (ALMA) — a set of 66 radio telescopes observing at millimeter and submillimeter wavelengths (84–950 GHz). The construction and the operation are led by European South Observatory (ESO). The solar observation focuses on interferometric measurements of the structure of the quiet solar atmosphere, coronal holes, active solar regions, filaments, and energetic solar phenomena. One of the ALMA Solar nodes is located at Astronomical Institute at the Czech Academy of Sciences in Ondřejov (ALMA, 2019).
- Karl G. Jansky Very Large Array (VLA) — an interferometer consisting of 27 independent radiotelescopes with 25 m diameter dish. The VLA is observing in range 1–18 GHz. The solar observations focus on active regions. The telescope is maintained by the National Radio Astronomy Observatory (NRAO); VLA (2019).
- Low-Frequency Array (LOFAR) — the 48 LOFAR stations are located at several European countries observing at 20 000 Low Band Antenna (LBA) and High Band Antennas (HBA) in the range 10–80 MHz and 120–240 MHz, respectively. The antennas are omnidirectional, and the signals are combined using aperture syntheses. LOFAR was founded by Netherlands Institute for Radio Astronomy (ASTRON), and unlike others, it observes solar dynamic activities (LOFAR, 2019).
- Square Kilometer Array (SKA) — a fully international project which aims to cover 10^6 m^2 of observation area with radio antennas creating long-baseline interferometric array consisting of SKA-low array dipole antenna for low-frequency 50–350 MHz, SKA-mid array parabolic antennas in 350 MHz–14 GHz and SKA-survey array of 12–15 m dishes about 350 MHz–4 GHz. The first phase (SKA1), covering 10 % of antennas, should launch in 2023, second full phase (SKA2) in 2030 (SKA, 2019).

There are many radio interferometers, that are focusing only on the Sun and that have rich long-term history and partially or fully available datasets:

- Siberian Solar Radio Telescope (SSRT) — consists of 48 antenna array with 4–8 GHz operating frequency and 10 MHz instantaneous band (Lesovoi et al., 2017).
- Nançay Radio Heliograph — 47 T-shaped antennas in the range 150–450 MHz that can do imaging (NRA, 2019).
- Nançay Decameter Array (NDA) — 144 helical/conical antennas across $7\,000 \text{ m}^2$ in frequency range 10–100 MHz (Zhang et al., 2018).
- MUSER — radio interferometric array located in Mingantu Station in Inner Mongolia of China, MUSER I contains 40 antennas with 4.5 m dishes in range 0.4–2 GHz. MUSER II has 60 antennas with 2 m dishes with range 2–15 GHz.
- Expanded Owens Valley Solar Array (EOVSA) — consists of 13 antennas, each has 2 m dish. It observes in range 1–18 GHz with full Stokes parameters. The array size $1.08 \times 1.22 \text{ km}$ enables observations with angular resolution $57'' \times 51''$ at 1 GHz.

Apart from the interferometers, there are also the radiospectrographs. Many observations in this work come from Hiraiso Radio Spectrograph (HiRAS) and Ondřejov Solar Radio Telescopes.

The propagation of the radio radiation is internally limited by a collective behavior – oscillations of charged particles at angular plasma frequency

$$\omega_{pe} = \sqrt{\frac{n_e e^2}{m_e \epsilon_0}}, \quad (1.1)$$

where n_e is the electron number density, e is the electron charge, m_e is the electron mass and ϵ_0 is the permittivity of free space. The plasma frequency from Equation 1.1 can be approximated by

$$f_{pe}[\text{kHz}] = 9\sqrt{n_e[\text{cm}^3]}. \quad (1.2)$$

In the plasma, the electromagnetic waves at frequencies lower than the plasma frequency do not propagate and are damped. Plasma frequency plays an essential role in the observations of the plasma emission. If we suppose that the emission is primarily at the plasma frequency, we can estimate the height above the photosphere using a solar density model.

The second parameter influencing the plasma radiation is the electron (angular) cyclotron frequency

$$\omega_{ce} = \frac{eB}{m_e}, \quad (1.3)$$

where B is the intensity of magnetic field. The approximation of cyclotron frequency is

$$f_{ce}[\text{MHz}] = 2.8B[G]. \quad (1.4)$$

The radio emission is influenced by the magnetic field, if the angle between the magnetic field \mathbf{B} and wave vector \mathbf{k} is nonzero. The electromagnetic propagation is damped under the cyclotron frequency. The emission can be in the form of the electron-cyclotron maser (ECM) for the non-relativistic unstable distribution function of hot electrons, the gyrosynchrotron emission for mildly relativistic electrons and the synchrotron emission in the case of ultra-relativistic non-thermal electrons (White, 2001).

1.1 Radio emission mechanisms

There are only two main groups of the radio non-thermal emission from the Sun: the plasma emission and the gyromagnetic emission. Because at the Sun we assume the mildly-relativistic electrons, we choose from the three types of gyromagnetic emission only the gyrosynchrotron emission.

1.1.1 Plasma emission

The theory of plasma radio emission is a set of very complex, complicated, and often non-linear theories. The emission processes at the fundamental and the first harmonics frequencies together with different polarization types and with specific aspects of polarization are presented. They are closely connected with Type I, Type II, Type III, Type IV fine structures and other observations (Type-U, radio dots, ...).

The foundation of the plasma emission mechanism was laid by Ginzburg & Zhelezniakov (1958, 1959). They considered two emission mechanisms which they called “Rayleigh scattering”, later named “nonlinear scattering” (Tsytovich, 1966) or “enhanced bremsstrahlung” (Tidman & Dupree,

1965). Unlike the gyromagnetic emission, the plasma emission is a multi-stage process. The stages cover the generation of Langmuir waves, their non-linear evolution and the successive conversion into the electromagnetic radiation.

Melrose (1987) gave the following summary. The generation of the Langmuir turbulence (longitudinal electrostatic waves) for the unmagnetized plasma ($B = 0$) and for the bump-in-tail instability is described by the dispersion relation

$$\omega^2 = \omega_{pe}^2 + 3v_{tb}^2 k^2, \quad (1.5)$$

with the absorption coefficient

$$\gamma(\mathbf{k}) = -\frac{\pi e^2 v_\phi^2}{\epsilon_0 m_e \omega_{pe}} \frac{\partial f(v_\phi)}{\partial v_\phi}, \quad (1.6)$$

where ω is the wave frequency, ω_{pe} is the plasma frequency of the particles with density n_e , mass m_e and background thermal velocity v_{tb} , \mathbf{k} is the wave vector with size $k = 2\pi/\lambda$ where λ is wavelength, e is the electric charge, $v_\phi = \omega/k$ is the wave phase velocity, ϵ_0 is the permittivity constant for vacuum and the function $f(v)$ describes the distribution function of the electron stream. If the term $\frac{\partial f(v_\phi)}{\partial v_\phi} > 0$, the absorption is negative and the amplitude and the energy of the Langmuir waves is growing.

In the plasma, the electromagnetic waves are present together with the Langmuir waves. Their dispersion is

$$\omega^2 = \omega_{pe}^2 + k^2 c^2. \quad (1.7)$$

And in the magnetic loops, the ion-sound waves with the dispersion

$$\omega = kc_s, \quad (1.8)$$

where c is the speed of light and c_s is the sound speed, can be generated. Only the transverse waves with the frequency $\omega > \omega_{pe}$ can escape from the medium.

Non-linear effects modify the Langmuir waves. One of the relevant processes is the three-wave interaction. The waves are described by the frequencies $\omega_1, \omega_2, \omega_3$ and the wave vectors $\mathbf{k}_1, \mathbf{k}_2, \mathbf{k}_3$. The energy and the momenta conservation implies that

$$\omega_3 = \omega_1 + \omega_2, \quad \mathbf{k}_3 = \mathbf{k}_1 + \mathbf{k}_2, \quad (1.9)$$

must be fulfilled. The interaction can also do the conversion of the Langmuir waves by the thermal particles or the density fluctuations. In that case, one of the wave vectors in the three-wave process in Equation 1.9 is replaced by the fluctuation described by \mathbf{k}_f .

In the three-wave process, the fundamental F and the first harmonic H electromagnetic wave emissions are involved (higher orders are neglected). In the fundamental plasma emission, there is an interaction of the Langmuir wave L with the ion-sound wave S generating the electromagnetic transverse wave T in two forms

$$L + S \rightarrow T, \quad L \rightarrow T + S. \quad (1.10)$$

This processes allow us to compute the brightness temperature T_B of the beam region with the density n_b , when the energy of Langmuir waves reaches $W_L \approx \frac{1}{2} n_b m_e v_b^2$ and the emission of

electromagnetic waves is into the angle $\Delta\theta$

$$T_B \leq \frac{\frac{1}{2}n_b m_e v_b}{\pi(\Delta\theta)^2} \left(\frac{v_b}{f_p}\right)^3. \quad (1.11)$$

The harmonic emission is connected with the coalescence

$$L + L' \rightarrow T. \quad (1.12)$$

From the momenta conservation it follows that $\mathbf{k}_L + \mathbf{k}_{L'} = \mathbf{k}_T$ and $k_T \approx \sqrt{3}\omega_{pe}/c$ for the transverse wave $\omega \approx 2\omega_{pe}$. This implies that L and L' must be almost head on which gives specific conditions for the emission generation and the velocity distribution function (Melrose, 1983).

1.1.2 Gyrosynchrotron emission

The gyrosynchrotron mechanism is one of the broadband generating mechanisms of the radio bursts in the solar corona. An example can be the broadband Type IV bursts. The transition between the gyroemission for the non-relativistic plasma and the synchrotron emission for $\gamma_{rel} \gg 1$ is the gyrosynchrotron mechanism. It is a set of specific descriptions and only approximate analytical methods. Generally, it must be solved numerically.

In the non-relativistic approximation, the emissivity is centered at frequencies $\omega = s\omega_{ce}$. The distribution for different angles creates 2^s -multipole with the distribution proportional $\cos^2\theta \sin^{2(s-1)}\theta$. The orders of $s = 1, 2, 3, \dots$ corresponds to the bipolar, quadrupolar, octupolar, ... After the transition to the ultra-relativistic limit, the emission is strictly into the angle $\theta = \alpha$, where α is the pitch-angle. The angle half-width $\Delta\theta \approx \gamma_{rel}^{-1}$ is centered on the frequency

$$\omega = \frac{s\omega_{ce}}{\gamma_{rel} \sin^2\theta}. \quad (1.13)$$

Dulk et al. (1979) approximated the absorption coefficients for small angles $|\theta - \frac{\pi}{2}| \ll \omega_{ce}/2\omega \ll 1$

$$\gamma^\sigma(s, \theta) = \frac{\omega_{pe}^2}{\omega_{ce}} \left(\frac{\pi\omega_{ce}}{2\omega}\right)^{\frac{1}{2}} \frac{1}{\beta_0^2 \sin^2\theta} \left(\frac{e\beta_0^2 \omega \sin^2\theta}{2\omega_{ce}}\right)^{\omega/\omega_{ce}} (1 - \sigma|\cos\theta|)^2, \quad (1.14)$$

and for $\theta = \pi/2$

$$\gamma^x(s, \theta) = \frac{\omega_{pe}^2}{\omega_{ce}} \left(\frac{\pi\omega_{ce}}{2\omega}\right)^{\frac{1}{2}} \frac{1}{\beta_0^2} \left(\frac{e}{2}\beta_0^2 \frac{\omega}{\omega_{ce}}\right)^{\omega/\omega_{ce}}, \quad (1.15)$$

$$\gamma^o(s, \theta) = \beta_0^2 \gamma^x(s, \theta), \quad (1.16)$$

$$\beta_0^2 = \frac{v_{tb}^2}{c^2}, \quad (1.17)$$

where o is the ordinary wave and x is the extraordinary wave.

The theory assume (Melrose, 1980) the Doppler frequency shift given by orbiting movements of particles

$$\omega = \frac{s\omega_{ce}\sqrt{1-\beta^2}}{1 - n\beta \cos\alpha \cos\theta}, \quad (1.18)$$

where $n = n_\sigma(\omega, \theta)$ is the refractive index for polarization σ , θ is the wave angle, $\beta = v/c$ is the electron speed, s is the integer harmonic number and α is the pitch angle.

Because in the plasma the waves below the plasma frequency cannot escape, the Razin effect gives the frequency

$$\omega \lesssim \begin{cases} 2\omega_{pe} & \text{for } \gamma_{rel} \approx 1, \\ \frac{3}{2} \frac{\omega_{pe}^2}{\omega_{ce} \sin \theta} & \text{for } \gamma_{rel} \gg 1, \end{cases} \quad (1.19)$$

at which the radiation from the distribution of electrons is absorbed.

1.2 Solar radio bursts

The solar radio emission has been systematically studied since the 1940s. One of the pioneers was Southworth (1945), who experimented in 3–10 cm wavelengths in 1942 and Reber (1944) who looked for 1.9 m radiation from the solar corona. Reber (1944) found that the radio emission exceeds the thermal emission of the solar photosphere. The greater brightness temperature at meter wavelengths has been identified as thermal emission from the much hotter solar corona. Another discovery by a chain of radar stations, which monitored the time variation of intensity, was by Hey (1946) who collated the observations and associated the emission with the large flare on the Sun. This discovery of enhancements and bursts opens a completely new view on the solar activity. It stimulated theory and laboratory research in plasma generation and propagation of the electromagnetic radiation.

The radio bursts are closely connected with the solar flares. The bursts are not created by plasma thermal mechanisms but the non-thermal emission. This emission depends on a conversion of the kinetic energy of particles into the electromagnetic waves, and the radio bursts are directly linked to the particle streams. In this way, the very fast particles are ejected, accelerated, trapped, and stored in the solar atmosphere during and after the flare. The zoo of the solar radio bursts was divided into five groups by Wild et al. (1963).

The different burst types can be plotted into the frequency-time diagram (Figure 1.2). Typical frequencies range from a few tens of MHz up to a few GHz. Time is measured after the start of the flare. The first radio signatures of the flare are the Type III radio bursts. In the past, the observed frequencies of maxima in the bursts were growing with an increase of the detection frequencies of the radio instruments.

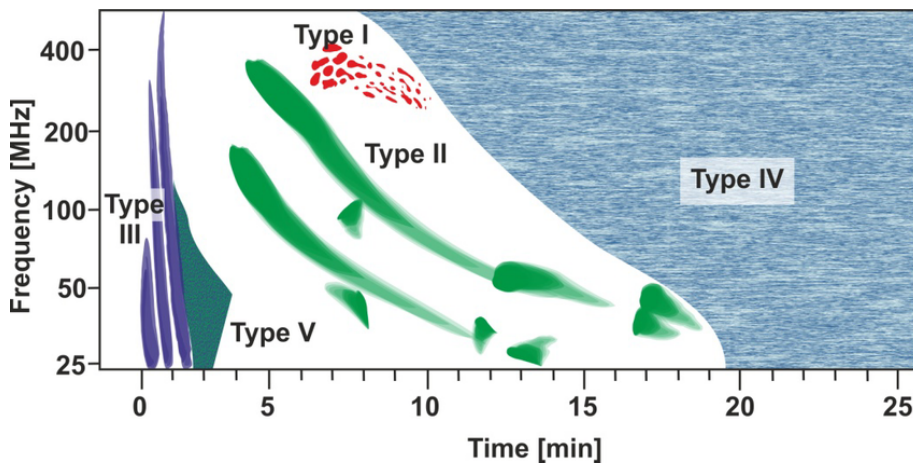


Figure 1.2: Type bursts Types I–V in dependence on frequency and time after the flare start for the meter wavelengths. Figure was taken from Dabrowski et al. (2016).

1.2.1 Type I bursts

The Type I radio noise storms are long series of bursts sometimes accompanied by continuum radiation. During the increased solar activity, hundreds of bursts per hour can occur at meter wavelengths. The duration of an individual burst can vary from 0.1 to 10 s with the bandwidth of a few MHz (Wild, 1951, Vitkevich & Gorelova, 1960, Elgarøy, 1961). Elgarøy (1961) found that half of the bursts have frequency drift between the Type II and Type III bursts, or they can approach the Type III.

The Type I noise storm is associated with the sunspots in the active regions but not every sunspot is radio noise active. The noise storm radiation is strongly circularly polarized (Payne-Scott & Little, 1951). The polarization corresponds to the ordinary mode of a magneto-ionic activity, while the storm center is polarized in the extraordinary mode. An example of Type I noise storm is in Figure 1.3. Elgaroy (1977) also did the review of different emission processes.

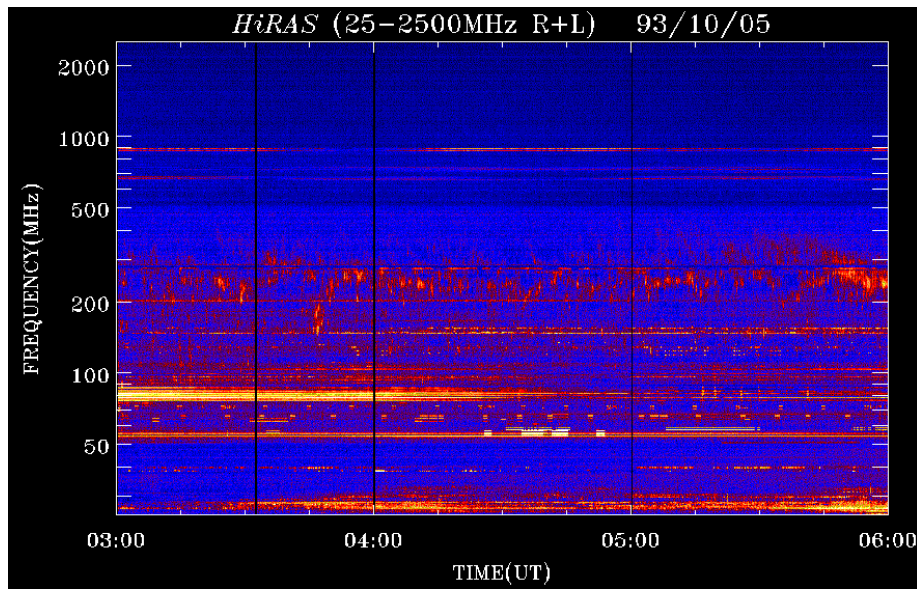


Figure 1.3: An example of Type I radio bursts from radiotelescope HiRAS (2012).

1.2.2 Type II bursts

The Type II is slowly drifting structure which last approximately 10 min. They are associated with large flares. The systematic frequency drift is interpreted as a shock with velocity 1 000 – 1 500 km/s (Wild et al., 1963). In the shock, the accelerated particles radiate at the plasma or the gyrocyclotron frequency. Except for the fundamental branch, the harmonic branch is usually formed at the double frequency. The examples of the observations from Hiraio Radio Spectrograph are in Figure 1.4 and 1.5. The recent observations and research were done by Vasanth et al. (2014), Kong et al. (2015), Zucca et al. (2018).

The emission and the acceleration mechanisms are still under investigation. The emission at the fundamental branch is assumed (Karlický & Bárta, 2011) to be caused by the coalescence of the Langmuir waves (L) with the ion-sound waves (S). This leads to the electromagnetic radiation (T), $L \pm S \rightarrow T$. Two Langmuir waves compose into the harmonic electromagnetic wave, $L + L' \rightarrow T$.

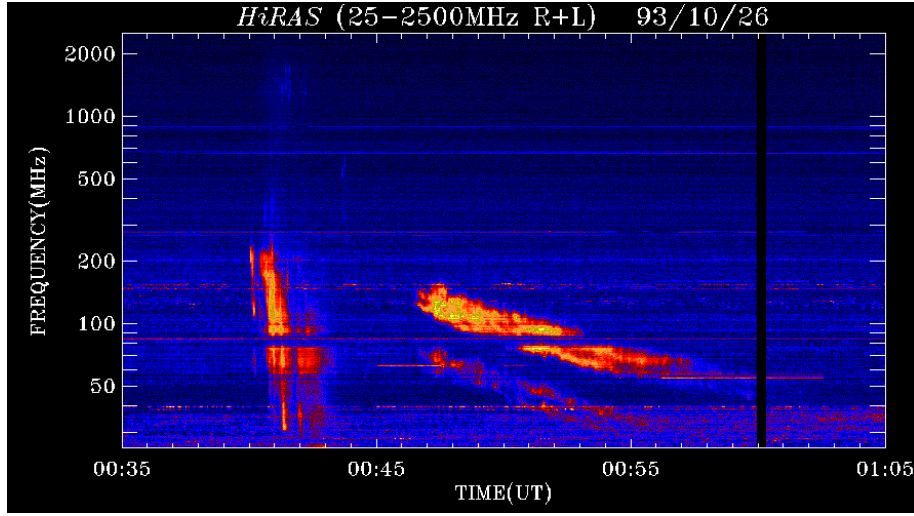


Figure 1.4: An example of Type II and III radio bursts from radiotelescope HiRAS (2012).

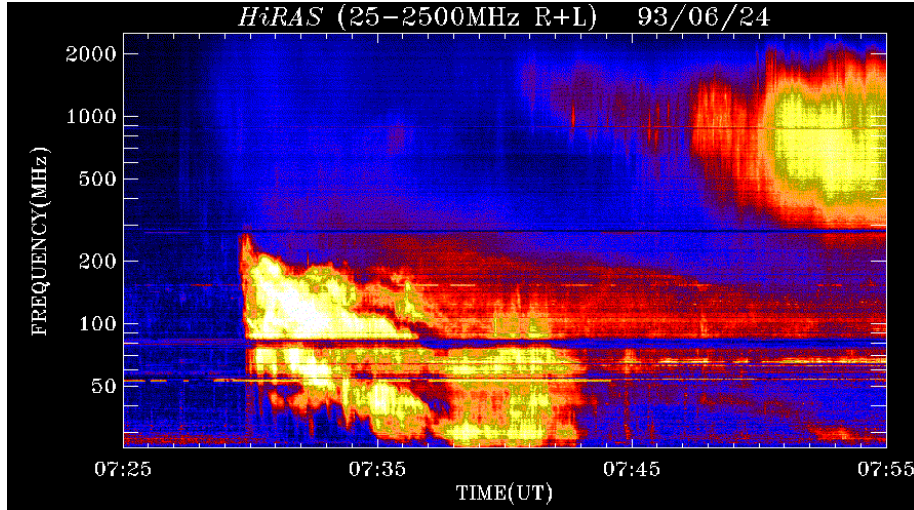


Figure 1.5: An example of Type II and IV radio bursts from radiotelescope HiRAS (2012).

1.2.3 Type III bursts

Type III are fast drifting radio structures (Wild et al., 1963) with a typical duration up to few seconds. The structures have a strong tendency to form a cluster of tens. They are associated with a flare, and they occur near the start of the event. Their spectrum is rapidly decreasing from high to low frequencies. Because of the high-frequency drift (~ 20 MHz/s) together with the broad bandwidth ($\sim 10 - 100$ MHz), the harmonic and the fundamental branch are merged. Wild et al. (1959) estimated from the interferometric measurement the velocity of the disturbance to be $0.4 c$ at ~ 1 solar radius above the solar photosphere.

The emission mechanism with estimated time scales by Sturrock et al. (1984), Aschwanden et al. (1993) is following:

1. Energy release (during solar flare) with total duration ≈ 10 min with ≈ 1 min impulsive phase.
2. Acceleration process of non-thermal particles, ≈ 5 s.

3. Propagation of the particles along the magnetic field, < 1 s.
4. Generation of the electrostatic longitudinal waves, immediate.
5. Transverse of the electrostatic waves into the electromagnetic, $\ll 1$ s.

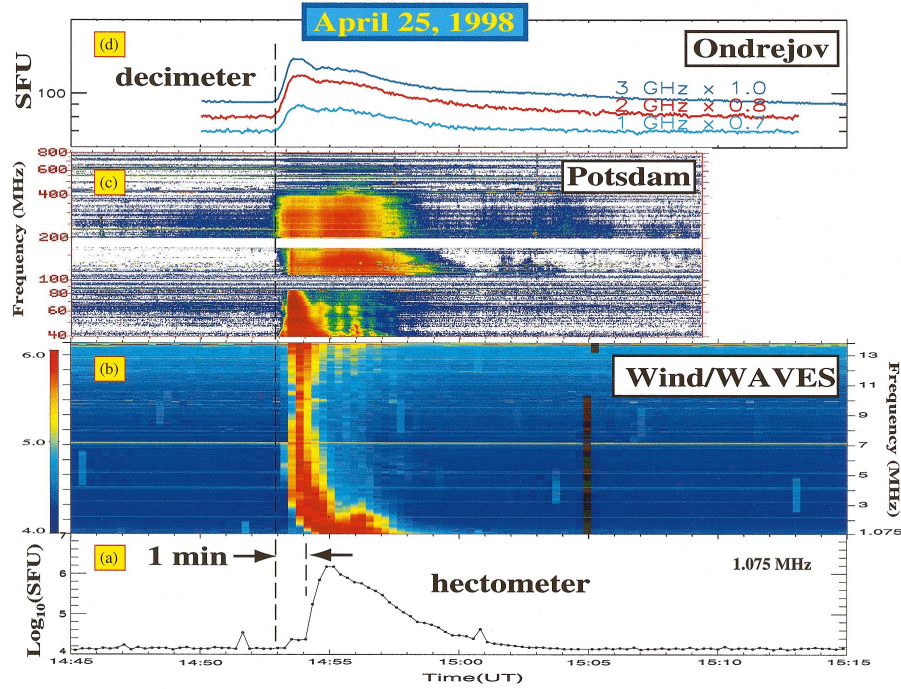


Figure 1.6: An example of Type III in the range from decimetric to hectometric waves by Reiner et al. (2000) on 25 April 1998: (a) Intensity-time profile at 1.075 MHz, (b) Dynamic spectrum Wind/WAVES instrument, (c) Dynamic spectrum in range 40–800 MHz, (d) Intensity-time profile at 1, 2, and 3 GHz.

The bursts are rich in variety: from the sharply defined leading frequency, narrow bandwidth, exponential probably collision decays and the short duration to another extreme when they are followed by the Type V radiation. The properties of the electron streams causing these bursts are still under the investigation (Reid & Kontar, 2018a,b). The examples of Type III radio observations from Ondřejov radiospectrograph (2018) and HiRAS (2012) spectrographs are in Figures 1.4, 1.6 and 1.7.

1.2.4 Type IV bursts

The distinct phenomenon following major outburst was reported by Boischot (1958), who studied the emission lasting tens of minutes after the initial flare. Using the interferometric measurements, he found that the altitudes and movements of the plasma are inconsistent with the plasma emission mechanism and the suggested synchrotron radiation. The designation Type IV was also used for continuum radiation following a solar flare. Later, this radio burst was designated as “moving”, assuming that the radiation region is moving outward with velocity $\sim 1\,000$ km/s, it can reach 5 solar radii above the photosphere, and the size can be $> 10'$ (Wild et al., 1963). The duration is typically up to two hours. The emission was partially circularly polarized corresponding to the

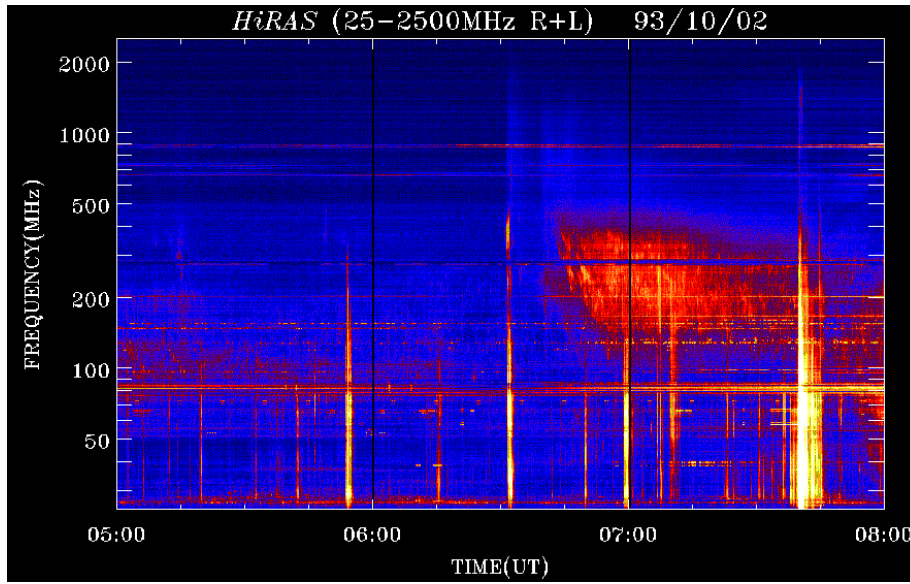


Figure 1.7: An example of Type III together with Type IV radio bursts from radiotelescope HiRAS (2012).

extraordinary wave mode. This theory assumes that the electrons with the energies of few MeV are trapped in a magnetic field and do not lose much of their energy by collisions or by radiation.

The second type of Type IV bursts is “stationary” which may live for more than a day. It includes long-lasting continuum storms. The burst frequency position is not moving and occurs slightly above the plasma frequency. The emission cone is narrow and the emission is strongly circularly polarized in ordinary mode. The initial emission theory was stated by McLean (1959) and clarified by Denisse et al. (1960). The high energy particles from the solar flare are trapped in the magnetic field, they diffuse downward the magnetic field and excite the plasma waves. At all frequencies, the intensity and polarization degree are proportional. Examples of Type IV radio observations are in the Figures 1.5 and 1.7.

1.2.5 Type V bursts

The Type V continuum radio emission follows the Type III bursts. They occur in 10 % of the Type III bursts as the diffusive broadband quasi-continuous emission. They are correlated with the flare decay phase. The drift speeds 1 000 km/s are common. Wild et al. (1959), Raoult et al. (1990) suggested that the burst can be the synchrotron emission from the same electron stream, that is responsible for Type III. The emission is slightly circularly polarized (10 %).

1.3 Fine structure radio bursts

Except for the classical burst Types I – IV, in the radio spectrum are also observed other less frequent phenomena, such as pulsations, spike bursts, fiber bursts, zebra patterns, S-bursts, and others. A comprehensive study of the fine structure solar radio bursts was done by Chernov (2011).

Table 1.1: Classification of pulsating structure models. Table was taken from Aschwanden (1987).

Modulation type	Emissivity
MHD oscillations (eigenmodes)	Gyrosynchotron modulation
	Plasma emissivity modulation
	Bounce motion of wave trains
Cyclic self-organizing systems	Wave-wave interactions
	Wave-particle interactions (e.g. streams or loss-cone instability)
	Periodic injection
Modulation of acceleration	Periodic magnetic reconnection

1.3.1 Pulsations

The pulsations include several observational phenomena. Their observational properties were summarized by Slottje (1982) and later, the models were proposed for pulsating events by Aschwanden (1987). They were divided into three groups (Table 1.1). Pulsations are usually not observed alone, but with a superimposition with the spikes, the fiber bursts, and the zebra patterns. A statistical study of observations was made by Aschwanden (1987), who concluded that background of the pulsations might be the Type IV burst, the Type III burst, the zebra pattern and the spikes, and that the pulsations might be the result of the microwave oscillator modulated emission. Among others, they also suggest that the flaring region consists of many current loops. In each, the tearing instability forms multiscale magnetic islands that modulate the plasma emission, and the motion of the loops causes the frequency drift. According to the mean period of pulsation P , Wang & Xie (2000) classified the pulsation events into three groups: long period pulsations, $P \sim 10$ s, short period pulsations, $P \sim 1$ s, very short period pulsations, $P < 1$ s. One of the recent studies was done by Tan et al. (2007), Figure 1.8. The unit “sfu” is defined as $1 \text{ sfu} = 10^{-22} \text{ W m}^2 \text{ Hz}^{-1}$.

1.3.2 Spike bursts

The spike burst is a very narrow radio emission. Its typical duration is < 0.1 s. The spikes occur in a groups of 10^4 bursts within a time ~ 1 min and show a fine structure with up to six harmonics. The total frequency bandwidth is typically 1–20 MHz. Generally, they are non-thermal, coherent emissions caused by a particle acceleration and an energy release in the flare. Spikes were observed in decametric (Barrow & Saunders, 1972) and also in microwave range (Droege, 1977, Staehli & Magun, 1986). Usually, they are strongly polarized in the same sense as burst Type I or Type III, the emission was related to the ordinary wave. Only the spikes related to the Type II bursts were unpolarized. The review summarising the possible plasma emission mechanisms was done by Fleishman & Mel’nikov (1998). They took into account proposed emission properties by Zhelezniakov & Zaitsev (1975), Zaitsev et al. (1985), Melrose (1991) and concluded, that none of them can fully explain the observational data.

1.3.3 Fiber Bursts

The fiber bursts are one of the fine structures of Type IV. They occur in groups of single narrowband fibers with the frequency drift, which is slower than Type III, but one magnitude higher than Type II (Bernold & Treumann, 1983, Benz & Mann, 1998, Jiřička et al., 2001). They appear in the clusters of 10 – 30, the duration between the individuals is ≤ 1 s at one frequency. The fibers are explained by two types of models. The first one, proposed by Kuijpers (1975) is based on the coupling

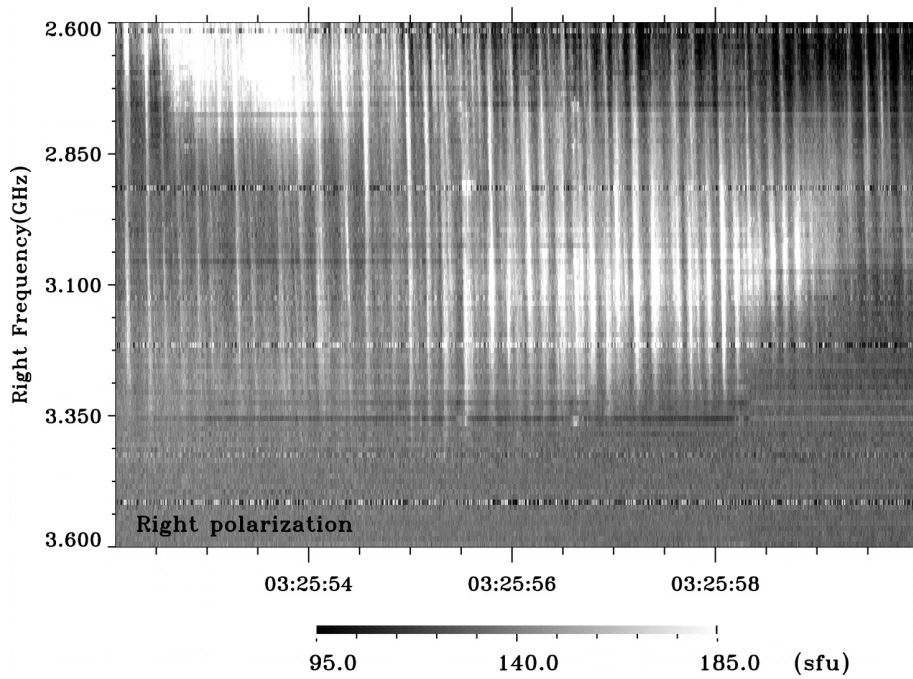


Figure 1.8: An example of microwave quasi-periodic pulsating event on 13 December 2006 on 3:25:52 UT after the flare peak. Selected right polarization. Figure was taken from Tan et al. (2007).

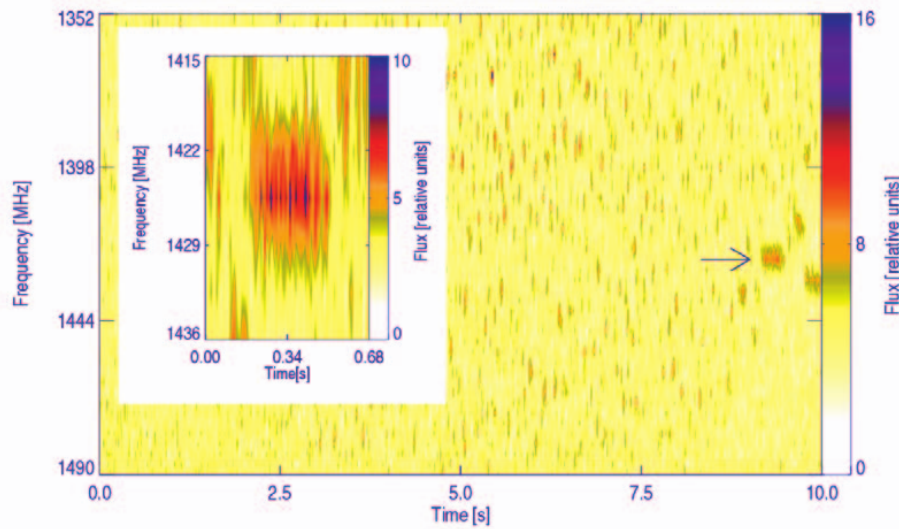


Figure 1.9: The burst from 26 April 2000, beginning at 14:10:05 UT. The arrow points to the chains. Figure was taken from Dabrowski et al. (2005).

of Langmuir wave L with the whistler wave w producing the transverse electromagnetic wave T , $L + w \rightarrow T$. The second one is the propagating Alfvén waves solitons which modulates the emission by Treumann et al. (1990). Both of them can be used for an estimation of the magnetic field strength (Benz & Mann, 1998). Kuznetsov (2006) based the model on the propagation of magnetoacoustic

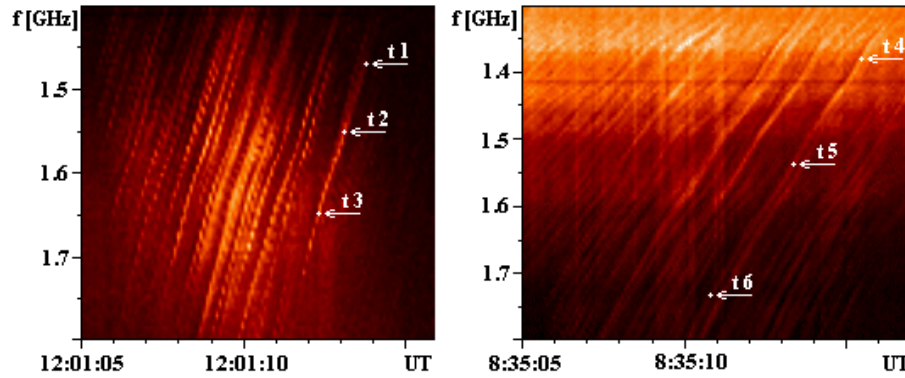


Figure 1.10: Fiber bursts on 23 November 1998 at 12:01:05 UT (left) and 12:01:16 UT (right). Figure was taken from Karlický et al. (2013).

waves along the magnetic field. Karlický et al. (2013) have shown that the observed radio spectra can be explained using the semiempirical and magnetohydrodynamical wave trains (Figure 1.10).

1.3.4 Zebra pattern

One of the most intriguing fine structure solar radio events are the solar radio zebras, and they are correlated and classified as fine structures of the Type IV solar radio bursts. Usually, they are classified as isolated, spectral, almost parallel stripes which are slowly drifting. Each zebra pattern can be described in the set of measured parameters: central frequency, frequency of individual stripes, phase time, polarization degree, stripe number, duration, frequency separation of the stripes and the relative frequency width. Observations from the Ondřejov radiospectrograph and the Yunnan observatory are in Figures 1.11 and 1.12.

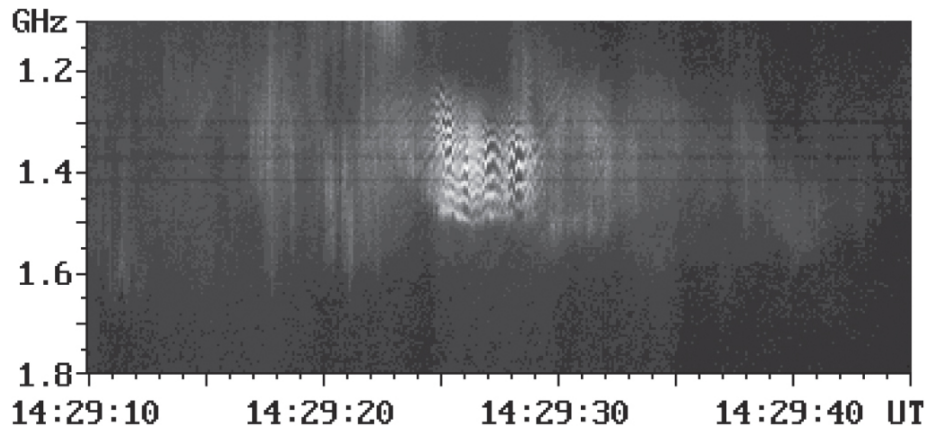


Figure 1.11: Zebra radio fine burst on 2 May 1998 by Ondřejov radiospectrograph (Karlický & Yasnov, 2018).

The comprehensive statistical study and classification was made by Tan et al. (2014) who took into account of 202 zebra pattern events from 40 solar flares which were observed from the Chinese Solar Broadband Radio Spectrometer at Huairou and the Ondřejov radiospectrographs. They classified them into three groups:

1. Equidistant zebra pattern – short duration 1 – 2 s, strongly polarized stripes with less than ten stripes, usually occurring in the rising flare phase.

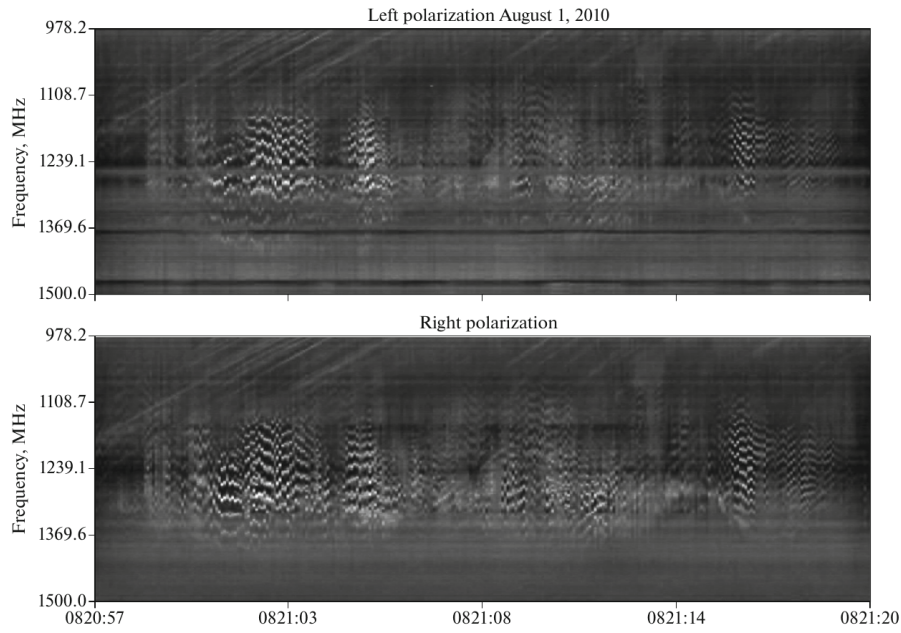


Figure 1.12: Left and right polarization of Zebra pattern from Yunnan observatory (YNAO, Kunming, China). Figure was taken from Chernov et al. (2018).

2. Variable-distant zebra pattern – irregular patterns with duration 2 – 10 s with a different polarization degrees, overlapping with other structures. The frequency between stripes is changing in time.
3. Growing-distant zebra pattern – complex stripes with a long duration (> 10 s), weak polarization and more than ten stripes are occurring in the decay flare phase.

They assume that the different mechanisms may have different physical formation mechanisms. From the mechanisms, they estimated that the magnetic field is in range 10 – 145 G.

Kaneda et al. (2015) measured the polarization in the dependence on the frequency. They found that the right circular polarization was 50-70 %. With cross-correlation, they found that the left polarization was delayed by 50-70 ms due to the different group velocities of the right and the left polarized wave. They concluded that the zebra pattern was created by the double plasma resonance. Chernov et al. (2016) reported the evolution of the polarization during the burst. In the beginning, there was a left circular polarization with the narrowband zebra stripes, in the decay phase, the polarization was right-handed with the left-handed background type IV burst.

Karlický (2014) analyzed the frequency variations of the zebra stripes in time. They found that the spectrum has a power-law form with index from -1.61 to -1.75 and assumed that the zebra stripes are generated at the upper-hybrid frequency. They can be interpreted as the plasma density variations. The frequency oscillations of the zebra stripes were interpreted by Yu et al. (2016) as the magnetohydrodynamical fast sausage waves that modify the positions of the double plasma resonance emission regions. They made the magnetohydrodynamical simulation of a plasma slab, constructed the skeletons of time variations and concluded that they can be used as detection of short-period oscillations. Kaneda et al. (2018) showed that the upward propagation sausage waves can interpret the observation with the velocities 3 000 – 8 000 km/s.

Recently, when searching for the most suited theory of the zebra pattern, Chernov (2018) summarized the observational properties that are still unexplained or under discussion:

- Imposition of the radio fiber over the zebra stripes, why they limit it from the low-frequency or the high-frequency range.
- Appearance in the pulsing mode.
- Wave-like or tooth-like frequency drifts in the columns.
- Growth of the frequency separation with the frequency.
- Superfine structure of the zebra stripes and the continuum.

The zebra pattern can be used for an estimation of the magnetic field and the plasma density. We assume the theory that the stripes are generated when $\omega_{pe} \approx s\omega_{ce}$, where s is the integer. The estimation of harmonic s is not an easy task. The method, which takes into account the height changes of the plasma density and the magnetic field, was proposed by Karlický & Yasnov (2015). We can compute for each stripe the cyclotron frequency as $\omega_{ce} = \omega_{pe}/s$. Because we know the cyclotron frequency for each stripe, we can estimate the magnetic field from Equation 1.3. Moreover, because we assume that the radiation is at or very close to the plasma frequency, we can compute the plasma density from Equation 1.1. If we look at the zebra stripes modulation, we know the electron density and the magnetic field temporal changes, see Karlický & Yasnov (2018).

The zebra patterns are also observed from the other objects. In our solar system, the known source of them is the Jovian decametric radiation (Panchenko et al., 2010, 2018). Their interpretation was done by Shaposhnikov et al. (2018). They showed that the double plasma resonance instability model cannot be used. Instead of that, they used the excitation of the ion cyclotron waves at the lower-hybrid frequency and the ion double plasma resonance regime. The radio zebras are also in the high frequency and the high temporal resolution observations of the Crab nebula by Hankins & Eilek (2007).

Chapter 2

Solar Radio Zebra Models

The theory of the zebra formation and the zebra pattern emission has been studied and discussed for over forty years. The efforts of an explanation of the different radio fine structures were proposed by the processes leading to the plasma emission mechanisms. Kuijpers (1980) gave a review of existing fine structure theories and concluded, that the most important high-frequency instabilities are connected with the magnetic traps in which the loss-cone instabilities generate the upper-hybrid waves. Later, the models were developed and based on the double plasma resonance instability and also other theories. The comparison of different zebra models was made by Zlotnik (2009) and Chernov (2010, 2011).

2.1 The Double Plasma Resonance Instability Model

The culmination of the effort for an explanation of the zebra pattern was done by publishing the series of papers by Zhelezniakov & Zlotnik (1975a,b,c). There are also other papers extending and clarifying the theory (Dulk, 1985, Winglee & Dulk, 1986, Yasnov & Karlický, 2004, Kuznetsov, 2005, Benáček et al., 2017).

In the literature, the most widely used theory for explaining the zebra pattern is the double plasma resonance (DPR), i.e., the resonance between the plasma frequency, the cyclotron frequency, and the electrostatic wave. While the designation double plasma resonance is mostly used for the condition $\omega_{pe} > \omega_{ce}$, the electron cyclotron maser (ECM) theory is used for the case $\omega_{pe} < \omega_{ce}$.

The theory of the electrostatic growth rate is computed from the permittivity tensor. We can write Poisson equation

$$\nabla \cdot \hat{\epsilon} \cdot \mathbf{E} = 0, \quad (2.1)$$

where $\hat{\epsilon}$ is the permittivity (dielectric) tensor with the components ϵ_{ij} .

If we assume that the particles are non-relativistic and they have the Maxwellian distribution function with the thermal velocity v_{tb} , the components of the permittivity tensor derived from the plasma kinetic theory are

$$\epsilon_{ij}(\omega, \mathbf{k}) = \delta_{ij} + \sum_s \frac{\omega_{pe}^2}{\omega} \frac{e^{-\lambda}}{k_{\parallel} v_{tb}} \sum_{n=-\infty}^{\infty} \hat{T}_{ij}, \quad (2.2)$$

where the tensor \hat{T}_{ij} is

$$\hat{T}_{ij} = \begin{pmatrix} n^2 I_n \frac{Z}{\lambda} & in(I'_n - I_n)Z & -nI_n \frac{Z'}{\sqrt{2}\lambda} \\ -in(I'_n - I_n)Z & (n^2 \frac{I_n}{\lambda} + 2\lambda I_n - 2\lambda I'_n)Z & i\sqrt{\lambda}(I'_n - I_n) \frac{Z'}{\sqrt{2}} \\ -nI_n \frac{Z'}{\sqrt{2}\lambda} & -i\sqrt{\lambda}(I'_n - I_n) \frac{Z'}{\sqrt{2}} & -I_n Z' \zeta_n \end{pmatrix}, \quad (2.3)$$

and the parameters are

$$\lambda = \frac{k_{\perp}^2 v_{\text{tb}}^2}{2\omega_{\text{ce}}}, \quad (2.4)$$

$$\zeta_n = \frac{\omega - n\omega_{\text{ce}}}{k_{\parallel} v_{\text{tb}}}, \quad (2.5)$$

$$Z(\zeta) = \sqrt{\pi} \int_{-\infty}^{\infty} \frac{e^{-t^2}}{t - \zeta} dt. \quad (2.6)$$

$$(2.7)$$

I_l is the modified Bessel function of l -th order, ω is the wave frequency, $\mathbf{k} = (k_{\parallel}, k_{\perp})$ is the wave vector parallel and perpendicular to the direction of the magnetic field, respectively. The summation in Equation 2.2 is over the index n . The plasma function $Z(\zeta)$ can be approximated in the case for $\zeta \ll 1$ by

$$Z(\zeta) = i\sqrt{\pi}e^{-\zeta^2} - 2\zeta \left[1 - \frac{2\zeta^2}{3} + \frac{4\zeta^4}{15} - \frac{8\zeta^6}{105} + \mathcal{O}(\zeta^8) \right], \quad (2.8)$$

or for the case of $\text{Re}(\zeta) > 0$ by

$$Z(\zeta) = i\sqrt{\pi}\sigma e^{-\zeta^2} - \frac{1}{\zeta} \left[1 + \frac{1}{2\zeta^2} + \frac{3}{4\zeta^4} + \frac{15}{8\zeta^6} + \mathcal{O}(\zeta^{-8}) \right], \quad (2.9)$$

where σ

$$\sigma = \begin{cases} 0 & y > \frac{1}{|x|}, \\ 1 & |y| < \frac{1}{|x|}, \\ 2 & y < \frac{-1}{|x|}. \end{cases} \quad (2.10)$$

We assume the electric field in the form

$$\mathbf{E} = \mathbf{E}_0 + \mathbf{E}_1, \quad (2.11)$$

where \mathbf{E}_0 is the constant part and \mathbf{E}_1 is a small perturbation. Then the perturbation $\mathbf{E}_1 = -\nabla\phi_1$, where $\phi_1 = \phi_{10} \exp i(\mathbf{k}\mathbf{r} - \omega t)$, is

$$\mathbf{k} \cdot \hat{\epsilon} \phi = k_x^2 \epsilon_{xx} + 2k_x k_z + k_z^2 \epsilon_{zz} = 0, \quad (2.12)$$

where the Fourier transformation was used

$$\frac{\partial}{\partial \mathbf{r}} \rightarrow -i\mathbf{k}, \quad \frac{\partial}{\partial t} \rightarrow i\omega. \quad (2.13)$$

Now, for the longitudinal electrostatic wave parallel to the magnetic field ($k_{\parallel} = 0$) we get

$$\epsilon_{\parallel} = \epsilon_{\parallel}^{(0)} + \epsilon_{\parallel}^{(1)} = 0, \quad (2.14)$$

where the term $\epsilon_{\parallel}^{(0)}$ corresponds to the background Maxwellian plasma and the term $\epsilon_{\parallel}^{(1)}$ is a correction to the hot and rare plasma component. In our case with $n_h \ll n_e$,

$$\text{Re } Z(\zeta) = -\frac{1}{\zeta}, \quad (2.15)$$

and in agreement with Chen (1984), Zhelezniakov (1997), Fitzpatrick (2015) we can write

$$\epsilon_{\parallel}^{(0)} = 1 - 2\omega_{pe}^2 \frac{e^{-\lambda}}{\lambda} \sum_{l=1}^{\infty} \frac{l^2 I_l(\lambda)}{\omega^2 - l^2 \omega_{ce}^2} = 0. \quad (2.16)$$

The solutions of the real part of Equation 2.16 are the dispersion relations for the upper-hybrid waves as well as for the Bernstein waves. Because in the present thesis we are interested in these waves in the upper-hybrid band, where the problem is to distinguish between these waves sometimes, therefore in the following we use for them the common term: the electrostatic waves.

For small $\lambda \ll 1$, Zhelezniakov & Zlotnik (1975a) gave the approximate relations

$$\epsilon_{\parallel}^{(0)} = 1 - \frac{\omega_{pe}^2}{\omega^2 - \omega_{ce}^2} - \frac{3\omega_{pe}^2 \omega_{ce}^2 \lambda}{(\omega^2 - 4\omega_{ce}^2)(\omega^2 - \omega_{ce}^2)} - \frac{\omega_{pe}^2}{(\omega^2 - s^2 \omega_{ce}^2)} \frac{s}{(s-1)} \left(\frac{\lambda}{2}\right)^{s-1}, \quad (2.17)$$

where s is the harmonic number of ratio ω_{pe}/ω_{ce} . The solutions of this equation are

$$\omega^2 = s^2 \omega_{ce}^2 + \frac{\omega_{pe}^2 \omega_{ce}^2}{(s^2 - 1)\omega_{ce}^2 - \omega_{pe}^2} \frac{s(s+1)}{(s-2)!} \left(\frac{\lambda}{2}\right)^{s-1}, \quad (2.18)$$

and for the frequencies close to

$$\omega^2 = \omega_{pe}^2 + \omega_{ce}^2, \quad (2.19)$$

we get

$$\omega^2 = \omega_{UH}^2 \equiv \omega_{pe}^2 + \omega_{ce}^2 + 3k_{\perp}^2 v_{tb}^2. \quad (2.20)$$

The relativistic theory of the double plasma resonance instability assumes the resonance between the electrostatic wave with the frequency ω and the wave vector \mathbf{k} , and the plasma characterized by the electron plasma frequency ω_{pe} and the electron cyclotron frequency ω_{ce} . The particles are moving at the velocities connected with the momenta $\mathbf{u} = (u_{\parallel}, u_{\perp}) = \gamma_{\text{rel}}(v_{\parallel}, v_{\perp}) = \gamma_{\text{rel}}/m_e(p_{\parallel}, p_{\perp})$. The resonance is in the form

$$\omega - \frac{s\omega_{ce}}{\gamma_{\text{rel}}} - \frac{k_{\parallel} u_{\parallel}}{\gamma_{\text{rel}}} = 0, \quad (2.21)$$

where s is the resonance harmonic number. If the s is positive, we speak about “normal Doppler effect”; if s is negative, it is called “anomalous Doppler effect”. If $s = 0$, it is only resonance between the plasma frequency and wave frequency without the magnetic field and it is called “Cherenkov radiation”.

When searching for the dependence of u_{\perp} on u_{\parallel} , the Equation 2.21 can be transformed into the equation of an ellipse (Winglee & Dulk, 1986)

$$\frac{(k_{\parallel}^2 c^2 + s^2 \omega_{ce}^2)^2}{s^2 \omega_{ce}^2 (k_{\parallel}^2 c^2 + s^2 \omega_{ce}^2 - \omega^2)} \left(\frac{v_{\parallel}}{c} - \frac{\omega k_{\parallel} c}{k_{\parallel}^2 c^2 + s^2 \omega_{ce}^2} \right)^2 + \frac{k_{\parallel}^2 c^2 + s^2 \omega_{ce}^2}{k_{\parallel}^2 c^2 + s^2 \omega_{ce}^2 - \omega^2} \frac{v_{\perp}^2}{c^2} = 1, \quad (2.22)$$

which has the center at

$$v_{\parallel} = c \frac{\omega k_{\parallel} c}{k_{\parallel}^2 c^2 + s^2 \omega_{ce}^2}, \quad v_{\perp} = 0. \quad (2.23)$$

The ellipse eccentricity is

$$e = \left(\frac{k_{\parallel}^2 c^2}{k_{\parallel}^2 c^2 + s^2 \omega_{ce}^2} \right)^{1/2}, \quad (2.24)$$

and the semimajor axis V along v_{\perp} is

$$V = c \left(\frac{k_{\parallel}^2 c^2 + s^2 \omega_{ce}^2 - \omega^2}{k_{\parallel}^2 c^2 + s^2 \omega_{ce}^2} \right)^{1/2}. \quad (2.25)$$

If the condition in Equation 2.21 is satisfied, the electrostatic wave is unstable, and its amplitude and the energy are growing or decaying dependent on the plasma velocity distribution function $f = f(v_{\parallel}, v_{\perp})$. If the region exist in the distribution function, for which the derivations $\partial f / \partial v_{\perp} > 0$ or $\partial f / \partial v_{\parallel} > 0$ are sufficiently larger than zero, the instability is growing. Otherwise, the energy of the instability is constant or decreasing.

The electromagnetic waves are an essential part of the DPR model. During the instability, the electrostatic waves are generated. Their group velocity is very close to zero, and they remain inside the instability region. These waves are formed into a dispersion branches. The dispersion branch is a relation between the frequency ω and the wave vector \mathbf{k} , in general case $\phi(\omega, \mathbf{k}) = 0$. In DPR case of the electrostatic waves, the branches are given by Equation 2.2. It is assumed, that due to the process of the plasma emission (Chapter 1.1.1), the electrostatic waves are transformed into the electromagnetic radiation, which can escape the instability region. The explanation of the radiation directionality and the polarization remains an open question.

2.2 Whistler Generation Model

The next zebra pattern model is based on the low-frequency electromagnetic waves in the solar corona. First, the whistler model was used for the generation of the fiber bursts by Kuijpers (1975). He assumed the non-linear coalescence of the whistler waves w and the Langmuir waves L , which are both generated by the unstable distribution functions, into the electromagnetic waves T ,

$$w + L \rightarrow T. \quad (2.26)$$

The theory for the explanation of the solar radio zebras was intensively developed using the same model by Chernov (1976), who published a series of papers. The theory was summarized in the work Chernov (2011). Even though the modulation of the plasma frequency by the whistler waves with the frequency $\omega_w \approx 0.1 \omega_{pe}$ is an appropriate assumption, the quasi-harmonic stripes are not easily explainable (Zlotnik, 2009) by this theory, unlike the fiber bursts. One has to assume that the whistler waves exist at some levels with a constant density to obtains the stripes. In the model, after some time of evolution, the unstable velocity distribution function quenches the instability and the

Langmuir waves generation. For the electrostatic wave generation, there must be a source of the energetic particles in the magnetic trap.

The region of the magnetic trap is divided into the amplification and the absorption regions. The length of the absorption where the whistlers are generated is

$$l_w = \Lambda \frac{c\omega_{ce}}{\omega_{pe}^2} \frac{n_e}{n_h}, \quad (2.27)$$

where Λ is Coulomb logarithm. The length of the absorption is

$$\Delta l_B = T_c v_{gr}^w \frac{l_B}{2v_e} v_{gr}^w, \quad (2.28)$$

where v_e is the electron velocity in a trap of length l_B , and v_{gr}^w is the whistler group velocity. Both distances are less than the trap size (Chernov, 2006). The coalescence in different amplification regions creates the stripe structure.

There are also indices that the amplification is much larger than the expected size of the trap (Bespalov & Trakhtenherzt, 1986). Though these problems in explanation, the whistler waves still must be considered as one of the important mechanisms for interaction with the Langmuir waves and the generation of the electromagnetic waves at the plasma frequency.

2.3 MHD Waves Model

The model based on the magnetohydrodynamical (MHD) waves with the aim to explain the solar and the Crab nebula radio zebra was proposed by Karlický (2013). He used a simple semi-empirical model of modulation of the radio continuum. He assumed the modulation by the density wave $n(h)$ (Roberts et al., 1984) in the form of the wave train

$$n(h) = n_0 \exp\left(-\frac{h}{H}\right) \left\{ 1 + n_R \cos\left[2\pi \frac{(h - h_0 - c_s t)}{L_w}\right] \right\}, \quad (2.29)$$

where h is the height in the atmosphere, n_0 is the density at height $h = 0$, H is the scale height, n_R is the relative density perturbation, c_s is the velocity of the slow magnetoacoustic wave, t is the time and L_w is the wavelength. Using this relation, he concluded that even for a small perturbation n_R , these two analyzed observations could be explained. The comparison of the computed and the observed zebra stripes profile is in Figure 2.1.

2.4 Eigenfrequencies (Trapped Plasma Waves) Model

LaBelle et al. (2003) created the zebra model that uses the generation mechanism proposed by Winglee & Dulk (1986), but is based on the trapping of the upper-hybrid waves in the density cavities. It assumes the double plasma resonance condition, which generates the electromagnetic Z-waves below the upper-hybrid frequency. Near the upper-hybrid frequency this mode becomes electrostatic and is trapped by the density inhomogeneities.

LaBelle et al. (2003) solved the equation electric field E in the cylindrical coordinates (r, ϕ)

$$\frac{1}{r} \frac{d}{dr} \left(r \frac{dE}{dr} \right) + \frac{1}{r^2} \frac{d^2 E}{d\phi^2} + k_{\perp}^2(r) E = 0, \quad (2.30)$$

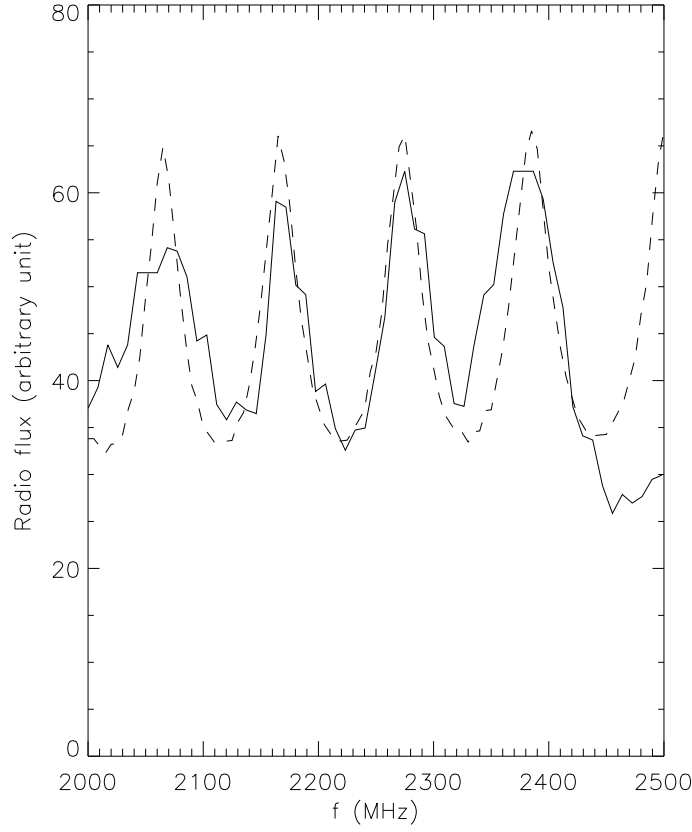


Figure 2.1: The comparison of computed (full line) and observed (dashed line) radio fluxes for density amplitude $n_R = 0.005$. Figure was taken from Karlický (2013).

with the dispersion relation of Z-mode for the background plasma

$$k_{\perp}^2(r) = \frac{2}{\rho_e^2} \frac{\omega_{ce}^2}{\omega_{pe}^2(r)} \left[\frac{\omega_{pe}^2(r) + \omega_{ce}^2}{\omega^2} - 1 \right], \quad (2.31)$$

where $\rho_e = \sqrt{2k_B T_e / m_e \omega_{ce}}$ is the electron gyroradius. The eigenfrequencies were determined by simple “waterbag” model where the density variation is

$$n(r) = \begin{cases} n_0 & \text{for } r > L, \\ n_0(1 + \delta) & \text{for } r < L, \end{cases} \quad (2.32)$$

where L is the cavity dimension. They computed the eigenfrequencies dependent on the radial “quantum” numbers n and the azimuthal quantum numbers m and showed how the frequency positions are changing (Figure 2.2).

2.5 Interference Model

Another model using the plasma density fluctuations is that by Bárta & Karlický (2006), who analyzed the regular structures and their impact on the spectra formation. Their model assumes a finite series of the periodic density square-shaped wells of the frequency depth $\Delta\omega_p$. The

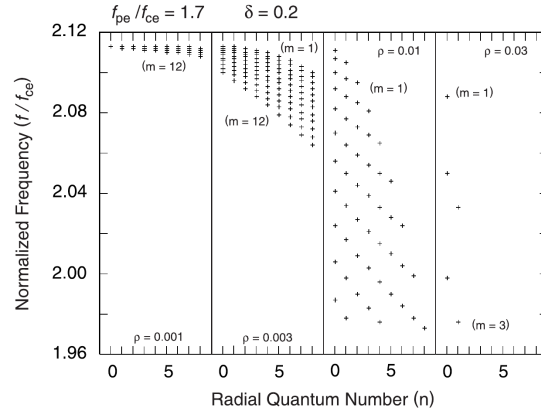


Figure 2.2: The computed eigenfrequencies of the cavity modes for ratio $\omega_{pe}/\omega_{ce} = 1.7$ and four cavity dimensions $\rho = \rho_e/L = 0.001, 0.003, 0.01, 0.03$ in the dependence on the radial number n and the azimuthal number m . The frequency spacing (corresponding to the frequency distance of the zebra stripes) 1 % between the eigenfrequencies are for $\rho = 0.01$. Figure was taken from LaBelle et al. (2003).

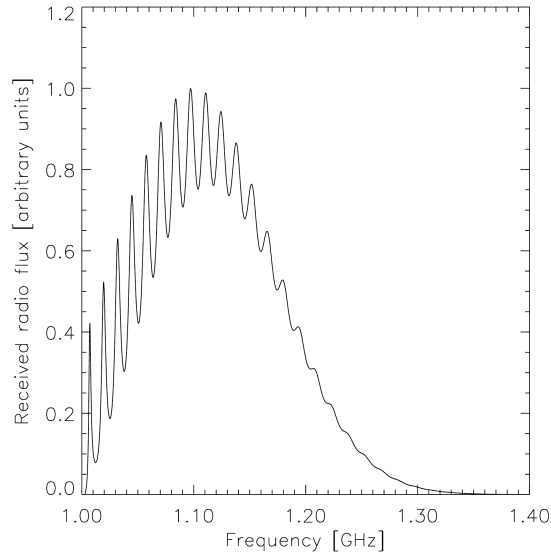


Figure 2.3: Spectrum formed by a single density well. Figure was taken from Bárta & Karlický (2006).

propagating electromagnetic wave is described by the Klein-Gordon equation

$$\frac{\partial^2 \mathbf{E}(\mathbf{r}, t)}{\partial t^2} - c^2 \Delta \mathbf{E}(\mathbf{r}, t) + \omega_{pe}^2(\mathbf{r}) \mathbf{E}(\mathbf{r}, t) = 0, \quad (2.33)$$

where the plasma frequency depends on the density structure $n(\mathbf{r})$. They solved this equation using the similarity with the Schrödinger equation. The solutions are the discrete frequencies. The electromagnetic wave with the frequency $\omega > \omega_{pe}$ is going through this region. It is partly transmitted and partly reflected, and forming the expected zebra stripes (Figure 2.3).

Chapter 3

Particle-in-Cell Model

There are two main approaches to make plasma simulations. The first approach is represented by the MHD models, which describe the plasma as a fluid with the parameters described by statistical properties. The second group consists of the kinetic models, which describe the plasma kinetic properties where the Vlasov, Fokker-Planck codes, and particle-in-cell (PIC) codes belong. The hybrid codes combine some plasma kinetic properties with the fluid description to create simulations, where the plasma is described more precisely than in the MHD models, but it is not as challenging processes as the kinetic models (Figure 3.1).

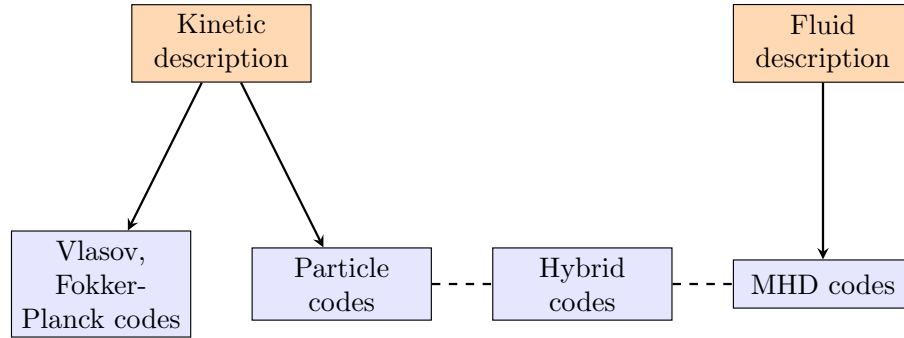


Figure 3.1: The classification of the computer plasma simulation codes.

In our research we used the PIC simulations for the study of the kinetic effect of the DPR. The PIC is a computational approach for solving the partial differential equations in the simplest form that is the most acceptable for the computers

$$\frac{\partial \mathbf{B}}{\partial t} = -\nabla \times \mathbf{E}, \quad \frac{\partial \mathbf{D}}{\partial t} = \nabla \times \mathbf{H} - \mathbf{J}, \quad (3.1)$$

$$\frac{d\mathbf{m}\mathbf{v}}{dt} = q(\mathbf{E} + \mathbf{v} \times \mathbf{B}), \quad (3.2)$$

where $\mathbf{E} = \mathbf{D}/\epsilon_0$ is the electric field, $\mathbf{B} = \mu_0\mathbf{H}$ is the magnetic field, t is time, \mathbf{J} is the current and m is the particle mass. ϵ is the relative permittivity and μ is the relative permittivity for the vacuum. Plasma has been studied with the usage of the PIC codes since 1950s (Dawson, 1983). One of the most advanced PIC codes used in this thesis is called TRISTAN (TRI-dimensional STANford code). TRISTAN is three-dimensional, fully electromagnetic and relativistic code. Originally, it was created by Buneman & Storey (1985) for planet magnetosphere simulations and later was published by Matsumoto & Omura (1993, p.67-84). The parallelization in the particles was made

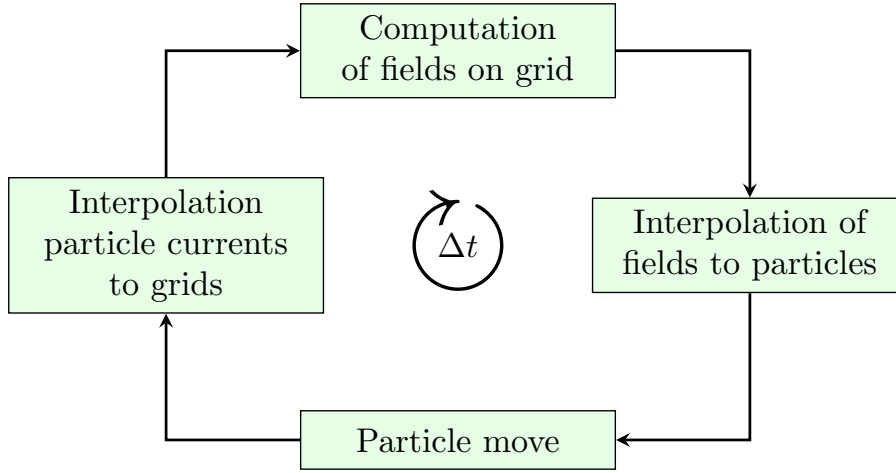


Figure 3.2: The computational steps of the general particle-in-cell method.

by Prof. Marian Karlický. The development of the parallelized version in the domains was one of the aims of my doctoral study. For more details about the parallelization, see Chapter 3.2.

The fields interpolated on the grid and particles are the essence of this model. They are solved as plasma superparticles in a four-part established loop (Figure 3.2). The Equations 3.1 and 3.2 are implemented as finite difference method in which the operators are implemented space- and time-centered for a higher-order accuracy. The electric field \mathbf{E} and magnetic field \mathbf{B} must be leap-frogged in time on the rectangular cubic grid. Therefore, the electric field \mathbf{E} with indexes (i', j', k') in the same position as the magnetic field \mathbf{B} with the indexes (i, j, k) is given by the interpolation of the adjacent cells

$$e_x(i, j, k) = \frac{e_x(i' - 1, j', k') + e_x(i', j', k')}{2}, \quad (3.3)$$

$$e_y(i, j, k) = \frac{e_y(i', j' - 1, k') + e_y(i', j', k')}{2}, \quad (3.4)$$

$$e_z(i, j, k) = \frac{e_z(i', j', k' - 1) + e_z(i', j', k')}{2}. \quad (3.5)$$

It is the same for the magnetic field. Each of the cells has dimensions $\Delta x = \Delta y = \Delta z$. The time discretisation is $\Delta t = 1$. Here, the Courant–Friedrichs–Lewy condition for an algorithm stability (Courant et al., 1928)

$$c\Delta t < \frac{\Delta x}{\sqrt{3}}, \quad (3.6)$$

must be satisfied. Δt is the time step, Δx is the cell size and c is the model light speed. The TRISTAN model is normalized to $\Delta x = 1, \Delta t = 1, c = 0.5$.

The summary of the independent model plasma parameters is in Table 3.1. TRISTAN uses the scales such that $\epsilon_0 = 1$ and $\mu_0 = 1/c^2$. This implies that $\mathbf{E} = \mathbf{D}$. For better computations, the symmetry between the electric field $\mathbf{E} = (e_x, e_y, e_z)$ and the magnetic field $\mathbf{B} = (b_x, b_y, b_z)$ is introduced in the form using the components multiplied by speed of light $c\mathbf{B}$.

Parameter	Symbol
Permittivity	ϵ_0
Speed of light	c
Electron mass	m_e
Mass ratio	m_i/m_e
Time step	$\omega_{pe}\Delta t$
Frequency ratio	ω_{pe}/ω_{ce}
Thermal velocity	v_{tb}

Table 3.1: The independent parameters used in the TRISTAN particle-in-cell model.

3.1 Model Workflow

The model is implemented in the programming language Fortran 90/95. The code was divided into several files. Except the main part of the model in the file `model.f90`, there are the files `savedata.f90` for the data storage on disk, `boundptl.f90` and `boundfield.f90` for the boundary conditions, `init.f90` for the initial conditions, and `size.inc` for the array configuration.

The parallelization is made by using the Message Passing Interface¹ (MPI). This technique is based on the principle that each processor has its data memory domain where it computes. The data exchange between these domains is based on the messages which are exchanged between the running processors. This library creates an interface for the effective and efficient creation of a connection between the processors and the nodes. The main advantage is that the library can use many types of hardware networks between the nodes. It can run on the supercomputers or computer clusters, and use existing the Ethernet network or special independent Infiniband.

The model block diagrams of the domain parallelized version of the TRISTAN code is shown in Figure 3.3. First, the model loads parameters that are connected with the allocation of the field and the particles arrays. Each processor allocates some subgrid of the fields and the corresponding particles. The configuration specifies the number of processors in each dimension.

The models are prepared in a such way, that all processors have the same grid size for the whole computing time. The number of particles per processor is given by the initial configuration. In default, the number density is constant, but it can change due to the flow of the particles from one processor to another, or by the other boundary conditions.

After the loading of the arrays, the MPI interface is initialized. MPI is automatically assigning the position in the whole model's grid to the processors in a dependence on the MPI library and the server MPI configuration. Usually, the processors are assigned the way, that the close subgrids are assigned to the close processors to minimalize the communication overhead between them.

Then, the model physical parameters that are the same for all the processors are loaded. From the independent parameters, the other dependent parameters are computed. Then, the fields are initialized. Usually, the initial electric field is set to zero. The magnetic field is configured according to the astrophysical situation and the conditions.

In the model, the subroutines for saving the fields and the particles are created. Originally, there were also subroutines for saving other parameters like the currents, the densities, the fluxes. However, because of the high standard storage capacity in computing clusters, it is possible to save all the data and then postprocess them. All the initial fields and the particles are stored before the start of computing itself.

¹<https://www.mpi-forum.org/docs/mpi-3.1/mpi31-report.pdf>

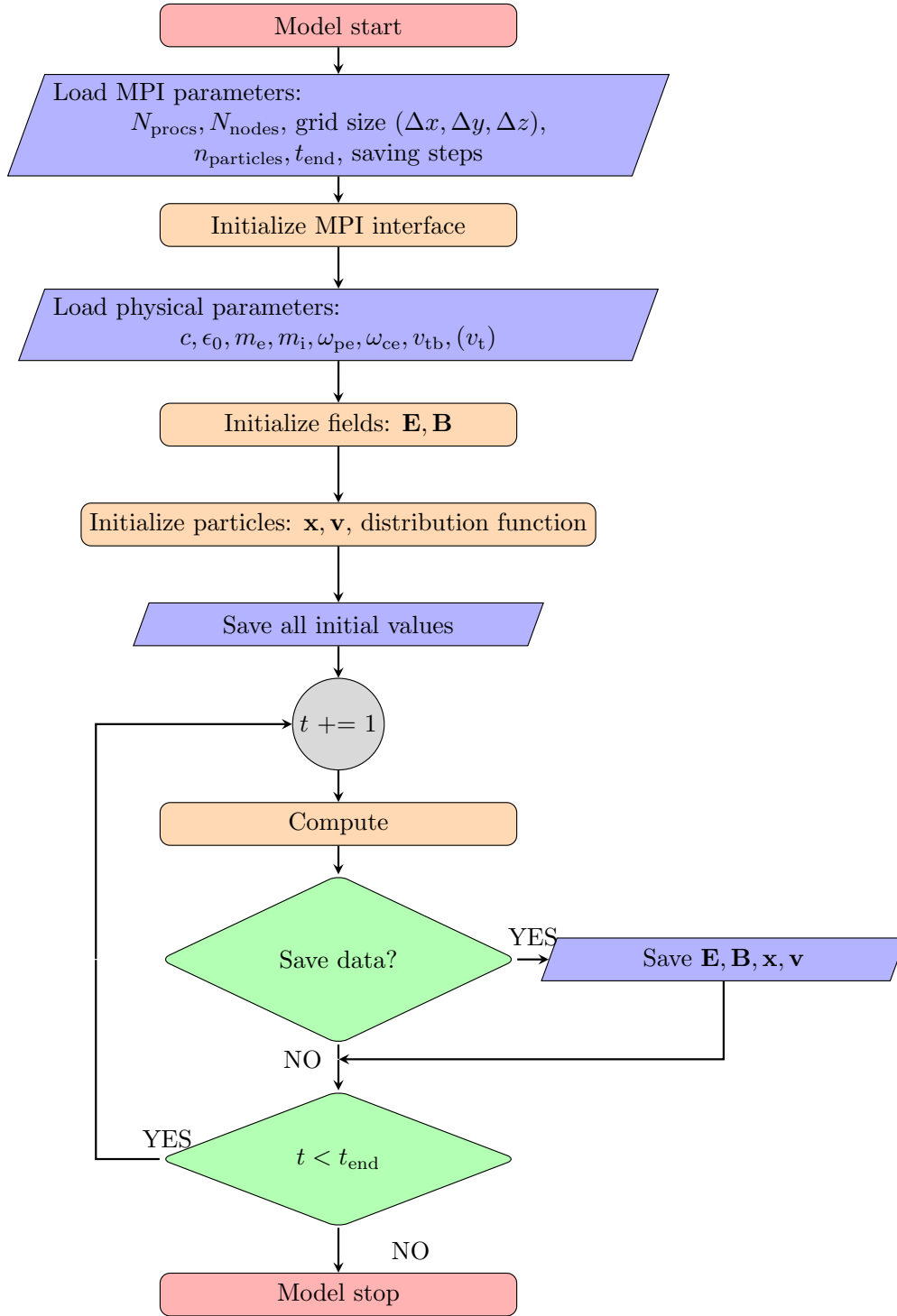


Figure 3.3: The specific computational steps of the TRISTAN particle-in-cell model. For more detailed description see the Chapter 3.1.

The computing is repeating a cycle that is incrementing the time until it equals the defined end time of the model. Each time step consists of the computation itself and, if required, the data are stored on the disk. The data storage frequency can be configured for different time windows.

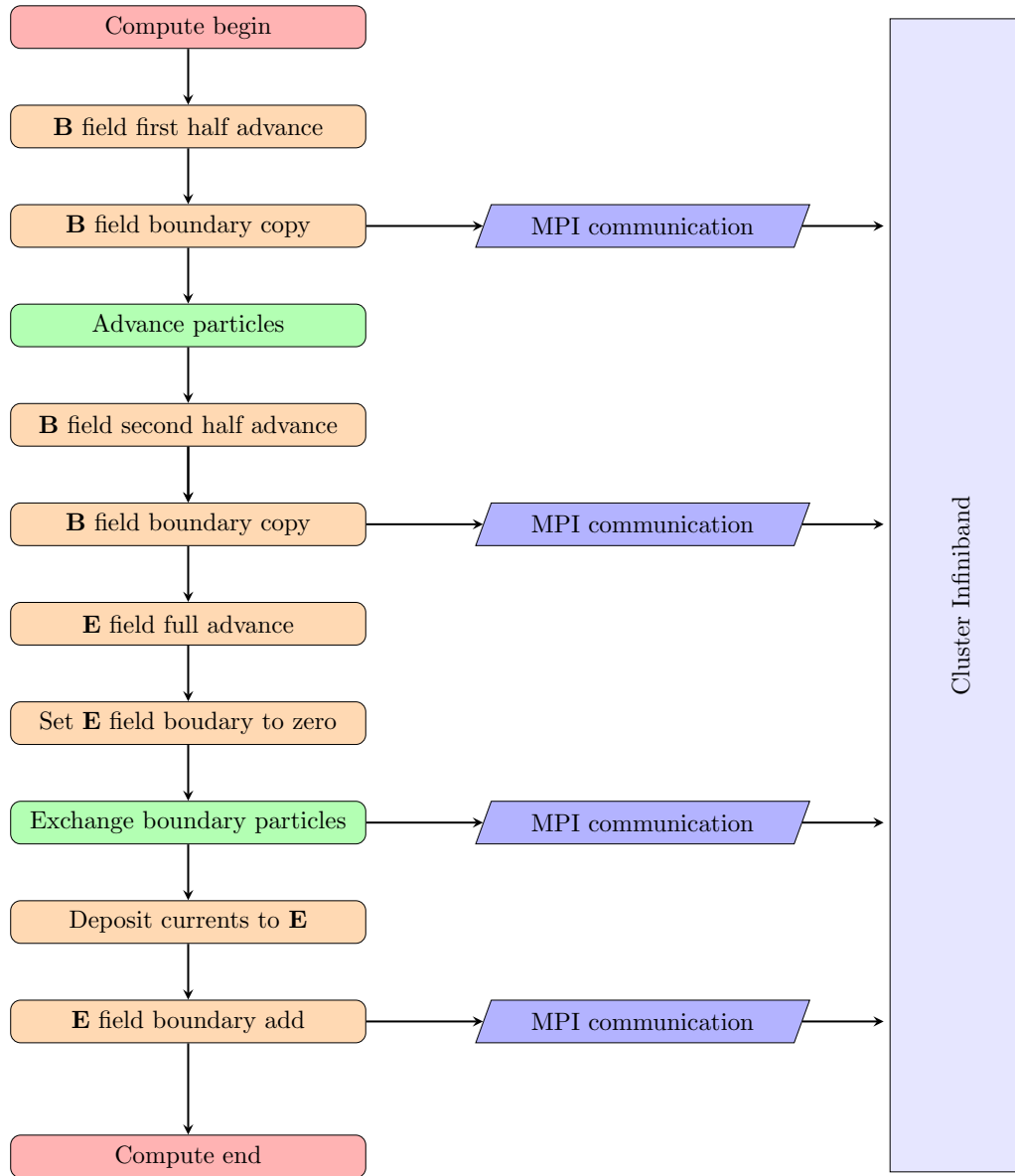


Figure 3.4: The details on one computational step of the TRISTAN model.

For example, in instability initial evolution, only every 100-th time steps can be saved, but then an interesting part occurs where every second time step can be saved. And then the interesting phase ends and we can save only each 1 000-th time step. This behavior is provided by the implemented storage module in the file *savedata.f90*.

More details about the computing algorithm are in Figure 3.4. The first half advance of the magnetic field is computed together with the magnetic field boundary conditions. Then the particles are advanced. The code computes the second part of the magnetic field half advance and the boundary conditions for the particles. Next, the particles are exchanged between the processors, and the current deposition into the electric field is computed. The time step is completed by the computation of the electric field boundary conditions.

Even though it seems that there are many computational steps that take a lot of time, the particle current deposition into the electric field consumes most of the time. This part of the model occupies

70–80 % of the computing time for the typical number density 100 particles. Other time consuming operation can be data storage. But this operation depends on the disk performance and also not every time step is saved.

3.1.1 Field updates

The TRISTAN code solves the Equations 3.1 and 3.2. The time change of the magnetic field in one time step is

$$b_x^{\text{new}}(i, j, k) = b_x^{\text{old}}(i, j, k) + c\Delta t \left[\frac{e_y(i, j, k+1) - e_y(i, j, k)}{\Delta z} - \frac{e_z(i, j+1, k) + e_z(i, j, k)}{\Delta y} \right], \quad (3.7)$$

$$b_y^{\text{new}}(i, j, k) = b_y^{\text{old}}(i, j, k) + c\Delta t \left[\frac{e_z(i+1, j, k) - e_z(i, j, k)}{\Delta x} - \frac{e_x(i, j, k+1) + e_x(i, j, k)}{\Delta z} \right], \quad (3.8)$$

$$b_z^{\text{new}}(i, j, k) = b_z^{\text{old}}(i, j, k) + c\Delta t \left[\frac{e_x(i, j+1, k) - e_x(i, j, k)}{\Delta y} - \frac{e_y(i+1, j, k) + e_y(i, j, k)}{\Delta x} \right]. \quad (3.9)$$

For the better numerical stability of the code, the advance of the magnetic field is computed in two sub-time steps with $\Delta t = \frac{1}{2}$. The full advance of the electric follows the half advances of the magnetic field and it is in the form

$$e_x^{\text{new}}(i, j, k) = e_x^{\text{old}}(i, j, k) + c\Delta t \left[\frac{b_y(i, j, k-1) - b_y(i, j, k)}{\Delta z} - \frac{b_z(i, j-1, k) + b_z(i, j, k)}{\Delta y} \right], \quad (3.10)$$

$$e_y^{\text{new}}(i, j, k) = e_y^{\text{old}}(i, j, k) + c\Delta t \left[\frac{b_z(i-1, j, k) - b_z(i, j, k)}{\Delta x} - \frac{b_x(i, j, k-1) + b_x(i, j, k)}{\Delta z} \right], \quad (3.11)$$

$$e_z^{\text{new}}(i, j, k) = e_z^{\text{old}}(i, j, k) + c\Delta t \left[\frac{b_x(i, j-1, k) - b_x(i, j, k)}{\Delta y} - \frac{b_y(i-1, j, k) + b_y(i, j, k)}{\Delta x} \right]. \quad (3.12)$$

3.1.2 Particle update

The Lorentz difference equation is

$$\mathbf{v}^{\text{new}} = \mathbf{v}^{\text{old}} + \frac{q\Delta t}{m} \left[\mathbf{E} + \frac{1}{2}(\mathbf{v}^{\text{new}} + \mathbf{v}^{\text{old}}) \times \mathbf{B} \right], \quad (3.13)$$

$$\mathbf{r}^{\text{next}} = \mathbf{r}^{\text{present}} + \Delta t \mathbf{v}^{\text{new}}. \quad (3.14)$$

For the computation of the particle advance, the three step form is used (Hockney & Eastwood, 1981, Chapter 4-7-1), (Birdsall & Langdon, 1991, Chapter 4-4):

1. First half of the electric acceleration

$$\mathbf{v}_0 = \mathbf{v}^{\text{old}} + \frac{q\mathbf{E}\Delta t}{2m}, \quad (3.15)$$

2. Magnetic rotation

$$\mathbf{v}_1 = \mathbf{v}_0 + 2 \frac{\mathbf{v}_0 \times \mathbf{v}_0 \times \mathbf{b}_0}{1 + b_0^2} \times \mathbf{b}_0, \quad (3.16)$$

3. Second half of the electric acceleration

$$\mathbf{v}^{\text{new}} = \mathbf{v}_1 + \frac{q\mathbf{E}\Delta t}{2m}. \quad (3.17)$$

The fields interacting with the particle at the position $\mathbf{r} = (x, y, z)$ are linearly weighted in a dependence on their distance $\delta x, \delta y, \delta z$ from the closest grid point i, j, k , where

$$i = \text{round}(x), \quad j = \text{round}(y), \quad k = \text{round}(z), \quad (3.18)$$

are the rounded values, and

$$\delta x = x - i, \quad \delta y = y - j, \quad \delta z = z - k, \quad (3.19)$$

can be used in the expression of $\mathbf{F}^{x,y,z}$. For example, x -component of the electric fields is computed as

$$\mathbf{F}_{e_x}^{x,y,z} = \mathbf{F}_{e_x}^{x,y,k} + [\mathbf{F}_{e_x}^{x,y,k+1} - \mathbf{F}_{e_x}^{x,y,k}] \delta z, \quad (3.20)$$

$$\mathbf{F}_{e_x}^{x,y,k} = \mathbf{F}_{e_x}^{x,j,k} - [\mathbf{F}_{e_x}^{x,j+1,k} - \mathbf{F}_{e_x}^{x,j,k}] \delta y, \quad (3.21)$$

$$\mathbf{F}_{e_x}^{x,y,k+1} = \mathbf{F}_{e_x}^{x,j,k+1} - [\mathbf{F}_{e_x}^{x,j+1,k+1} - \mathbf{F}_{e_x}^{x,j,k+1}] \delta y, \quad (3.22)$$

$$\begin{aligned} 2\mathbf{F}_{e_x}^{x,j,k} &= e_x(i, j, k) + e_x(i-1, j, k) \\ &\quad + [e_x(i+1, j, k) - e_x(i-1, j, k)] \delta x, \end{aligned} \quad (3.23)$$

$$\begin{aligned} 2\mathbf{F}_{e_x}^{x,j+1,k} &= e_x(i, j+1, k) + e_x(i-1, j+1, k) \\ &\quad + [e_x(i+1, j+1, k) - e_x(i-1, j+1, k)] \delta x, \end{aligned} \quad (3.24)$$

$$\begin{aligned} 2\mathbf{F}_{e_x}^{x,j,k+1} &= e_x(i, j, k+1) + e_x(i-1, j, k+1) \\ &\quad + [e_x(i+1, j, k+1) - e_x(i-1, j, k+1)] \delta x, \end{aligned} \quad (3.25)$$

$$\begin{aligned} 2\mathbf{F}_{e_x}^{x,j+1,k+1} &= e_x(i, j+1, k+1) + e_x(i-1, j+1, k+1) \\ &\quad + [e_x(i+1, j+1, k+1) - e_x(i-1, j+1, k+1)] \delta x. \end{aligned} \quad (3.26)$$

3.1.3 Current decomposition

TRISTAN does not calculate the charge density array like other PIC codes. Instead of that, it uses a direct particle current deposition into the electric field. This approach removes the cohesion between the particles and enables parallelization.

A charge conservation scheme was proposed by Villasenor & Buneman (1992). The electric field is modified by the current $\mathbf{J} = (j_x, j_y, j_z)$

$$e_x(i, j, k) = e_x(i, j, k) - j_x \cdot cy \cdot cz, \quad (3.27)$$

$$e_x(i, j+1, k) = e_x(i, j+1, k) - j_x \cdot \delta y \cdot cz, \quad (3.28)$$

$$e_x(i, j, k+1) = e_x(i, j, k+1) - j_x \cdot cy \cdot \delta z, \quad (3.29)$$

$$e_x(i, j+1, k+1) = e_x(i, j+1, k+1) - j_x \cdot \delta y \cdot \delta z, \quad (3.30)$$

$$e_y(i, j, k) = e_y(i, j, k) - j_y \cdot cx \cdot cz, \quad (3.31)$$

$$e_y(i, j+1, k) = e_y(i, j+1, k) - j_y \cdot \delta x \cdot cz, \quad (3.32)$$

$$e_y(i, j, k+1) = e_y(i, j, k+1) - j_y \cdot cx \cdot \delta z, \quad (3.33)$$

$$e_y(i, j+1, k+1) = e_y(i, j+1, k+1) - j_y \cdot \delta x \cdot \delta z, \quad (3.34)$$

$$e_z(i, j, k) = e_z(i, j, k) - j_z \cdot cy \cdot cx, \quad (3.35)$$

$$e_z(i, j+1, k) = e_z(i, j+1, k) - j_z \cdot \delta y \cdot cx, \quad (3.36)$$

$$e_z(i, j, k+1) = e_z(i, j, k+1) - j_z \cdot cy \cdot \delta x, \quad (3.37)$$

$$e_z(i, j+1, k+1) = e_z(i, j+1, k+1) - j_z \cdot \delta y \cdot \delta x, \quad (3.38)$$

where

$$cx = 1 - \delta x, \quad cy = 1 - \delta y, \quad cz = 1 - \delta z. \quad (3.39)$$

3.1.4 Boundary conditions

In the domain parallelized code, there are two types of the boundaries between the computing grids:

1. Boundaries between the subgrids, which belong to the different processors. These boundaries sew together the neighboring subgrids in all three dimensions. They are implemented in the same way as the periodic boundaries because both of them smoothly connect subgrids. For the continuity of the physical quantities, these boundaries must stay unchanged.
2. Outer boundaries of the whole computing domain. At his moment the code uses periodic boundary condition. They must be implemented according to the studied situation.

The boundary data must be sent between the processors. Each processor must determine where to send the data. Sending the fields is easier because the data amount is always the same. The size of the sending buffers of the particle is changing.

The sending of the particles is more complicated. The particle can cross the boundary of the sub-grid in 6 walls, 12 corners between two walls and 8 corners between three walls. According to the direction of the particle, they migrate into one of the 26 other neighboring processors. The number of particles at each processor is changing. For that reason, the initialized array containing all the particles must be larger than the initial number of the particles. Each processor holds the

variable with an actual number of the particles (ions or electrons). If the particle is flowing out of the sub-grid it should be removed from the memory, the item in array is replaced by the particle from the end of array and the number of particles decreases by one. If the particle inflows, it is appended to the end of the particle array and the number of the particles is incremented by one.

3.1.5 Data storage

For the data storage, we use the high-performance parallelized library Hierarchical Data Format in version 5 (HDF5²). It was created for the fast I/O processing and the storage. It has support for many programming languages, and the data can be read from many visualizing programs or data processing routines in Python. The library enables storage of one data array into one file by many processors simultaneously. HDF5 internally uses the MPI interface.

3.2 Domain Parallelisation and Other Code Improvements

The TRISTAN model was the initial starting point of our work and it was originally parallelized only in the particles. Each of the MPI processes was computing the fields on the grids separately. The only source of a change was the electric field generated by the particle currents. Each processor was handling a specific subset of the particles. Their electric fields were summed across all the processors and distributed between them. The boundary conditions were the next advantage of this solution. They were solved locally without MPI communication. The maximum number of the processors that could be efficiently used was smaller or equal to the number of the particles per cell. If a processor had in mean less than one particle per cell, the computation became inefficient. Each processor had a whole grid, but almost no particles, and it was not computing effectively.

The solution for the scaling up is to implement a domain parallelization. The main domain is divided into the subgrids. In our case, each of them has the same size, and they are distributed among the processors. Each processor is computing a specific subgrid and the particles in it. In comparison with the particle parallelization, this implementation is suitable for large domains with a small particle density, and in the case we need to use more processors than the mean particle density.

This type of parallelization is scaling up to a point, where the time spent by the boundary communication exceeds the computing part. It is approximately proportional to the ratio between the size of the boundaries and the volume of the grid. For 100 particles per cell, the subdomain size should be larger than $10\Delta \times 10\Delta \times 10\Delta$.

The implemented improvements for a domain parallelization in TRISTAN are following:

- The interpretation of the domain size changes from the global domain scale to subdomain scale; the introduction of new parameters connected with the number of the processors in each dimension.
- The position in cartesian topology is assigned to each processor using the `MPI_Cart_create` and `MPI_Cart_coords` commands.
- Implementation of the boundary conditions for the fields with the MPI communication.
- Implementation of the boundary condition for the particles using MPI.
- Parallel data storage using HDF5. The fields from the grids are saved into one file. The particle data are stored into separate files.

²<https://www.hdfgroup.org/solutions/hdf5/>

There have been small improvements of the code including:

- Transition of the code from Fortran 77 to Fortran 90/95.
- Division of one long file into more files following the logical arrangements – initialization, storage, particle boundary, field boundary.
- Replacement of the `CPU_TIME()` method by the `SYSTEM_CLOCK()` method. The `SYSTEM_CLOCK` method gives the real-time instead of `CPU_TIME` time. The difference shows up when the processors are not 100 % utilized. `CPU_TIME` gives computing time, not the wall time of the simulation.
- Adding a new random seed method. The method reads a random number from the Linux system and uses it as the seed. It also guarantees that each processor generates a different order of the numbers.
- Transition from `real(4)` to `real(8)` with all the fields and particles. It includes the `real(8)` random generator.
- Implementing method `Add_Step()`, which sets the saving interval for the fields and particles for the given time step.
- Implementation of a better Gaussian random number generator. Adding the relativistic correction for the velocity. Until now, a “five-hump” generator was used, which only combined normal generators and created a “humped” Gaussian distribution.
- Implementation of the loss-cone types of the distribution function: DGH, loss-cone Maxwell, loss-cone Kappa, loss-cone cut-off Kappa, and loss-cone power-law.
- Creation of the starting scripts for the supercomputers Salomon and Anselm, the clusters Oasa and Metacentrum, and for the PCs. They can be used for the PBS Pro or the Slurm job scheduler.

The model includes the parameter *cartd* which can be set to 0 for the particle parallelization or to 3 for the 3D domain parallelization. It can always be chosen, which model is more efficient.

Because the code was developed for the scaling on a large number of the processors, the crucial part at the end of the implementation was testing its performance. The result of the scaling is in Figure 3.5. The testing model had the following parameters: the size was $120\Delta \times 60\Delta \times 1800\Delta$, the particle density $n_e = n_i = 96$ and the thermal velocity of the particles $v_{tb} = 0.018c$. 6–720 processor cores were used on the Salomon cluster. The wall time per one model time step is computed as a mean of 10 computing steps. The initial loading of the model is not included, because it is negligible in comparison with the typical computing times of the real models.

For the scaling, the cluster parameters are important. The main computing clusters are Oasa in Ondřejov and Salomon in Ostrava. They both have similar computing nodes. Both are using 2 sockets with 12 core CPUs (Oasa has Intel Xeon E5-2650v4 @ 2.20GHz, Salomon has Intel Xeon E5-2680v3 @ 2.5 GHz) and Infiniband. Both have 128 GB RAM per node. In Oasa, up to 11 nodes, and in Salomon up to 1008 nodes can be used.

Figure 3.5 shows that both models are scaling differently. While the model parallelized in particles is more efficient for the small number of the particles, its efficiency is changing at around 40 processors. For a higher number of processors, some of them have only one particle per cell, and their computing becomes inefficient. For the number of processors higher than 96, in particle

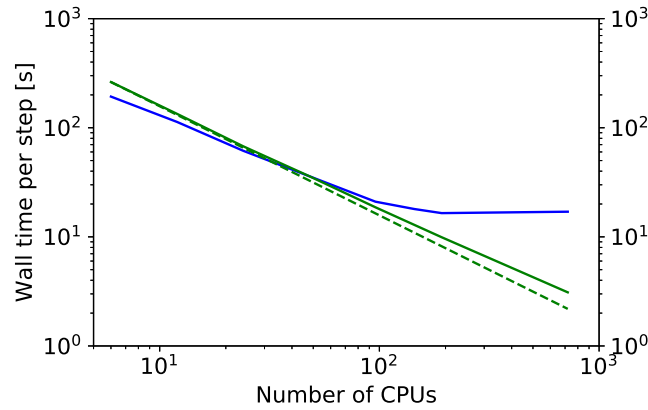


Figure 3.5: Scaling of the code with parallelization in the particles (blue line) and after parallelization in the domains (green line). The dotted green line is the ideal scaling of the model with increasing the number of processors. For more details about the model parameters, see the text.

parallelized model, there are processors that do not even have particles. They are computing only the fields, and their run is useless.

On the other hand, the domain parallelized model is less efficient for less processors than the older version. However, the model is scaling well up to the tested 720 processors, where the slowdown on 30 nodes in comparison with the ideal scaling is about 50 %.

The conclusions of the model usage are following: for computing of small models, ideally on one node, or model with the number of the particles per cell much larger than the number of processors, use the older particle parallelization. For large models, where the number of the particles per cell is not much larger than the used number of processors, use the newer version.

Next parameter influencing the computing time is the storage performance. The amount of time spent on data storage is highly dependent on the saving frequency, the data amount, the overloading of storage by other users. The storage time of one array is increasing with the number of processors. How often and what amount the data are stored and how they influence the total computing time, must be carefully selected. The storage of all particles and all fields from the previous model on Salomon using 720 processors can take a few seconds. Several tens of GB can be saved in one time step.

3.3 Proposed future development

Even though the aims of the model development, the domain parallelization, are fulfilled, there are still adjustments that could or probably, in the near future, should be done, and which we recommend from our knowledge of the code. They concern the code maintainability, the new Fortran features, increasing the representation of the accelerators in the clusters, and others:

- Transition from Fortran 90/95 to newer version Fortran 2008/2018. This Fortran version brings better support for the object oriented programming, the support of the command `forall`, using the AVX vector instructions, and others.
- Packing of the model parameters and the arrays into the objects. For example, the physical parameters could be stored in one object, MPI parameters in another, particles in the next one.

- Support of an acceleration offloading for a better scaling under 1 000 processors – using OpenMP, support for CUDA or Salomon’s Xeon Phi.
- Optimizing the part of the code, where the currents are transformed into the electric fields.
- Usage of the Single Instruction Multiple Data (SIMD) instructions. E.g., Advanced Vector Instructions AVX and AVX-512. Appropriate usage of AVX could increase the computing power by four.

Chapter 4

Summary of my Results

The presented papers are published in the journals: Astronomy and Astrophysics, Solar Physics, and Astrophysical Journal. They are included in Appendixes A–E. The following sections summarize the main aims, the used methods and the results.

4.1 Paper I: Temperature Dependent Growth Rates of the Upper-hybrid Waves and Solar Radio Zebra Patterns

Benáček, J., Karlický, M., Yasnov, L. 2017, Astronomy & Astrophysics, 598, A106.

The double plasma resonance instability is the most promising model of the solar radio zebras. The unstable loss-cone type of the distribution function generates the electrostatic waves that are trapped in the instability region. Then, the electrostatic energy is transformed into the electromagnetic waves, which can escape the instability region. In this paper, we numerically computed the growth rates of the upper-hybrid waves in the double plasma resonance instability. For computing of the growth rates, we used the numerical approach of theory by Winglee & Dulk (1986) with a relativistic correction from Yasnov & Karlický (2004). We used the thermal electron component with DGH distribution function of the hot electrons. The thermal velocity was in the range $0.1\text{--}0.3\ c$, the background thermal velocity $0\text{--}0.018\ c$, the magnetic field $10\text{--}100\ \text{G}$. The results were computed for the ratio $\omega_{pe}/\omega_{ce} = 3\text{--}20$.

We numerically analyzed the values and shapes of the growth rate profiles as a function of the ratio ω_{pe}/ω_{ce} . For each value ω_{pe}/ω_{ce} , we computed the growth rates in $k_{\perp}\text{--}k_{\parallel}$ domain, and then we selected the highest growth rate value and determined its position. We computed the growth rates dependent on the background and the hot electron thermal velocity.

We found that the growth rate dependence on ω_{pe}/ω_{ce} shows distinct peaks for the thermal velocities of hot electrons up to $0.3\ c$. For higher hot electron thermal velocities, the peaks are smoothed. In our case, the frequency shift can be up to 16 % for $v_t = 0.3\ c$. Moreover, there is a frequency shift of the growth rate peaks for a non-zero temperature of the background component. The frequency shift is increasing with the thermal velocity of the hot electrons, but also with the temperature of the background plasma. The frequency shift is linearly proportional to the harmonic number s . We showed how the shift is changing the values of the magnetic field strength obtained by the observations.

We also presented that the values of the wave vectors deviate from the analytical estimations for maximal growth rate value. However, the condition $k_{\perp} \gg k_{\parallel}$ is fulfilled in both cases. Figure 4.1 shows the growth rate in dependence on the ratio ω_{pe}/ω_{ce} for three hot electron thermal velocities

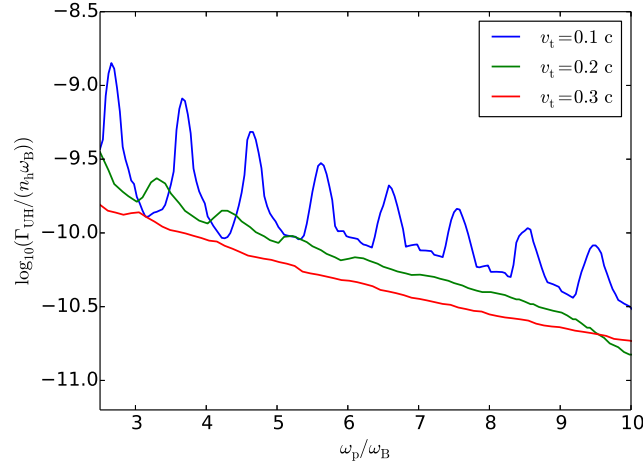


Figure 4.1: The growth rate of the upper-hybrid waves in dependence on ratio ω_{pe}/ω_{ce} for three hot electron temperatures. The growth rate peaks becomes smoothed with increasing the temperature of hot component. With increasing temperature of hot electrons, the peaks are shifted in the frequency towards the low values of the ratio ω_{pe}/ω_{ce} .

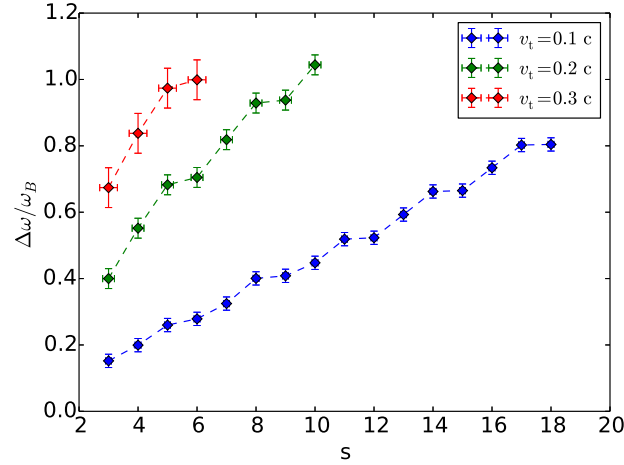


Figure 4.2: The frequency shifts of the peaks in the dependence on harmonic number s for three temperatures of hot component.

$v_t = 0.1\text{--}0.3\ c$. The Figure 4.2 presents the peak frequency shift for the same thermal velocities of the hot electrons.

4.2 Paper II: Brightness Temperature of Radio Zebras and Wave Energy Densities in Their Sources

Yasnov, L.V., Benáček, J., Karlický, M. 2017, Solar Physics, 292, 163.

In this paper, we analyzed three zebra pattern observations. We estimated the brightness temperatures for two scale heights (1 and 0.21 Mm) and the conversion rates from the electrostatic to the electromagnetic energy. We used the prescription for the emission of the electromagnetic waves into the angle θ (Zhelezniakov, 1997)

$$\theta = \operatorname{arcsec} \left(\frac{\omega}{\omega_L} \right) = \operatorname{arcsec} \left(\frac{s}{\sqrt{s^2 - 1}} \right), \quad (4.1)$$

where ω is the emission frequency, ω_L is the plasma frequency at the source. It is supposed that the emission frequency is at the upper-hybrid frequency, and at the height h and the radius r from the loop axis the particle density is (Chernov et al., 1994, Kuznetsov & Kontar, 2015)

$$n_e(r, h) = n_{\text{em}}(h_0) \exp \left(-\frac{r^2}{d^2} \right) \exp \left(-\frac{h - h_0}{H} \right). \quad (4.2)$$

d is the loop width, H is the scale height, n_{em} is the density at the height h_0 . The brightness temperature (Zaitsev & Stepanov, 1983) was computed in the form

$$T_b = \frac{S}{7 \times 10^{-11}} \frac{1}{f_{\text{GHz}}^2 L_8^2}, \quad (4.3)$$

where S is the electromagnetic flux, f_{GHz} is the observed frequency in units of GHz, L_8 is the size of the emission region in units of 10^8 cm.

Using the two density scale heights, two loop widths (1 and 2 arcsec) and the zebra stripes observations, we found that the plasma emission region can be very small. The brightness temperature was estimated $1.1 \times 10^{15} - 1.3 \times 10^{17}$ K for the scale height 1 Mm and $4.7 \times 10^{13} - 5.6 \times 10^{15}$ K for the scale height 0.21 Mm. Though the non-coherent emission mechanism does not enable the temperatures higher than 10^{12} K, these high temperatures are due to the coherent emission processes.

Then, we computed energy density of the electrostatic waves using the PIC simulations. It was assumed that all the generated electrostatic energy is in the form of the upper-hybrid waves. We used the DGH electron velocity distribution function. The model size was $\lambda\Delta \times \lambda\Delta \times 32\Delta$, where λ is the typical electrostatic wave wavelength. The plasma frequency was $\omega_{\text{pe}}\Delta t = 0.05$, the time step $\Delta t = 1$, and the harmonic number $s = 3-18$. The particle density per cell was $n_e = 1920$. The density ratios of the hot and the background component were $n_h/n_e = 1/8, 1/16$, and $1/32$.

We showed the initial exponential growth of the electric energy in PIC. We found that the saturation energy of the electrostatic waves is proportional to the ratio n_h/n_e . We fitted the saturation energy profile for $s = 3-18$ by the exponential function and estimated the energies for $s > 20$. The saturation energy density of the electrostatic waves was found 1.6×10^{-3} of the initial kinetic energy of the hot electrons. We estimated the density of the hot component $n_h = 1.28 \times 10^{13} \text{ m}^{-3}$ using the instability growth rate of the upper-hybrid waves (Thejappa, 1991)

$$-\gamma_{\text{UH}} = 4.4 \times 10^{-2} \omega_{\text{pe}} \frac{n_h}{n_e}, \quad (4.4)$$

and the collisional damping

$$\gamma_c = 2.75 \frac{n_e}{T_e^{3/2}} \ln \left(10^4 \frac{T_e^{3/2}}{n_e^{1/3}} \right), \quad (4.5)$$

where T_e is the background plasma temperature. From the hot electrons density and the saturation energy of the electrostatic energy in PIC model, we got the energy density of the upper-hybrid waves in the DPR region $4.4 \times 10^{-5} \text{ J m}^{-3}$. When we compared the local energy density of the electrostatic waves and the measured flux of electromagnetic radiation, we got the transformation efficiency from the electrostatic waves into the electromagnetic waves $2.54 \times 10^{-6} - 8.86 \times 10^{-4}$.

4.3 Paper III: Double Plasma Resonance Instability as a Source of Solar Zebra Emission

Benáček, J., Karlický, M. 2018, Astronomy & Astrophysics 611, A60.

In this paper, we numerically analyzed the processes in the double plasma resonance instability. We used three-dimensional particle-in-cell code TRISTAN. The PIC model brings a new view to the instability. Using it, we could compute other important aspects of the instability like the growth rate of the electrostatic energy of all waves, the evolution of the particle distribution function or the electrostatic saturation energies.

In the simulation, we used two types of models — the multi-mode model with size $128\Delta \times 60\Delta \times 128\Delta$ and the specific mode model with the size $\lambda\Delta \times \lambda\Delta \times 32\Delta$, where λ is the wavelength of the most unstable wave found by searching for the model size with the highest growth rate. While the multi-mode model is used for detailed analyses, the specific-mode model is used to save computational time in the computations of a broader range of the parameters. We used the DGH distribution of the hot electrons in range of the thermal velocity $v_t = 0.15-0.3 c$ and the background thermal velocity $v_{tb} = 0.03-0.05 c$. The plasma frequency was $\omega_{pe}\Delta t = 0.05$. The cyclotron frequency varied $\omega_{ce} = 0.056-0.38 \omega_{pe}$, corresponding to $s = 3-18$. We used the particle density per cell $n_e = 960$ and the ratio of the hot and the background particles $n_e/n_h = 8$.

First, we showed a good agreement between the specific-mode model and the multi-mode model. Then, we computed the growth rates and the saturation energies for a broader range of ratio $\omega_{pe}/\omega_{ce} = 3-7$. They were both computed for selected values of background temperatures v_{tb} and hot electrons temperatures v_t .

We found a good agreement between the analytical (numerically computed) and the simulation results. The positions of the growth rate and the saturation peaks are at almost the same position ω_{pe}/ω_{ce} . Also, there is a good agreement in the peak position between the analytical theory a PIC simulations. The saturation energies have a higher contrast between the minima and the maxima than the growth rates. The saturation energy is proportional to the number density of the hot electrons. It can be up to 1 % of the initial kinetic energy of the hot electrons. With increasing the ratio n_e/n_h , the growth rate peaks are shifted towards the lower ratio ω_{pe}/ω_{ce} .

We analyzed the time evolution of the velocity distribution function of the hot electrons. The distribution density is decreasing in a region of the DPR resonance ellipses. In these regions, the hot electrons lose their kinetic energy. The kinetic energy is converted into the electrostatic waves. After the transfer of energy, the hot electrons shift to the lower values of v_\perp in the velocity space. An example of the evolution of the distribution is in Figure 4.3.

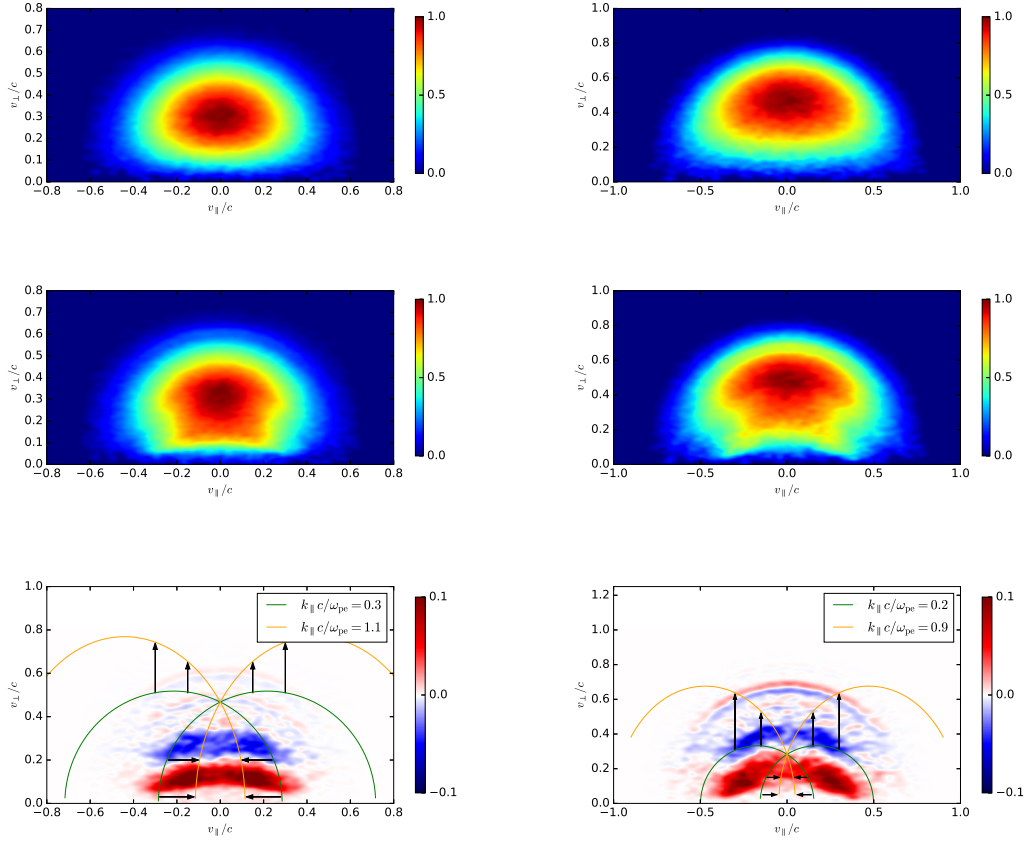


Figure 4.3: The changes of the distribution function of the hot electrons in the multi-mode models. *Left column:* The model with parameters $v_t = 0.2 c$, $v_{tb} = 0.03 c$, and $s = 6$. *Right column:* The model with parameters $v_t = 0.3 c$, $v_{tb} = 0.03 c$, and $s = 5$. *First row:* The state at initial time $\omega_{pe} t = 0$, *Second row:* The distribution function at $\omega_{pe} t = 1000$. *Third row:* The change between the initial distribution and distribution at $\omega_{pe} t = 1000$. The regions with the enhanced density are red, and with the reduced density are blue. The curves are the resonance ellipses and the arrows indicate the position change by increasing the value of k_{\parallel} .

4.4 Paper IV: Growth Rates of the Upper-Hybrid Waves for Power-Law and Kappa Distributions with a Loss-Cone Anisotropy

Yasnov, L. V., Benáček, J., Karlický, M. 2019, Solar Physics, 294, 29.

Although the growth rates were studied by many authors (Winglee & Dulk, 1986, Yasnov & Karlický, 2004, Benáček et al., 2017) using the DGH distribution function, this distribution is not fully physical for the magnetic mirror in the solar magnetic loops. In this paper, we analyzed the growth rates of the upper-hybrid waves for two types of the anisotropic velocity distribution functions: the power-law and the kappa distributions. The power-law is characterized by the parameter δ and the kappa distribution by the parameter κ . The δ was in range 5 and 10, the κ parameter was used in two limit cases $\kappa = 1.5$ and $\kappa = \infty$. The kappa distribution function is approaching the Maxwellian distribution for $\kappa \rightarrow \infty$. The thermal velocities were used in

range $10 v_t - 0.5 c$, where $v_t = 6.75 \times 10^7 \text{ m s}^{-1}$. The pitch angle was used in the steps $\theta_c = 10^\circ, 30^\circ, 50^\circ, 65^\circ$ and 80° . The background plasma had temperature $T = 3 \times 10^6 \text{ K}$.

For the analytical computations, we followed the procedure by Kuznetsov & Tsap (2007). The growth rates are not searched as the maximum on the upper-hybrid branch (Benáček et al., 2017), but as maximum for $\omega > \omega_{pe}$ in the $\omega - k_\perp$ domain. Finally, we compared the growth rates and the observations on 1 August 2010.

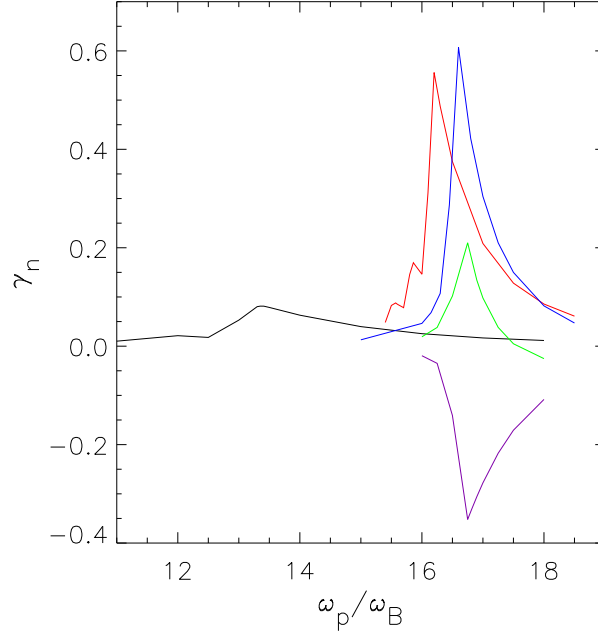


Figure 4.4: The growth rates of the upper-hybrid waves as a function of ω_{pe}/ω_{ce} . The velocity distribution is the loss-cone power-law with $\delta = 5$, the harmonic number $s = 16$ and the low-velocity cut-off $v_m = 0.3 c$. The loss-cone angles are: 10° (black line), 30° (red line), 50° (blue line), 65° (green line) and 80° (violet line).

We found that the growth rates for the power-law distribution strongly depend on the hot electron loss-cone angle θ_c . For small angles, the growth rate is broad; for the high angles, the growth rate is negative (Figure 4.4). The maximal growth rate was found for the angle $\theta_c = 50^\circ$. For power-law index $\delta = 10$, the growth-rate peaks are more distinct than for $\delta = 5$. For $\delta = 5$ the growth rates peaks are higher than for $\delta = 10$ but they are distinguishable only in an interval around $10 v_t$. An example of the growth rate dependence on the loss-cone angle is in the Figure 4.4.

The analysis of the growth rates for the kappa distribution showed that for both cases of the κ index, the maxima are shifted with decreasing characteristic momentum p_κ towards the lower values of ω_{pe}/ω_{ce} . The peaks become broader and therefore, indistinguishable. We assumed for the kappa distribution, which is isotropic up to some large momentum but forms loss-cone distribution above, that the growth rates form distinct peaks and the zebra pattern can be generated.

4.5 Paper V: Growth Rates of the Electrostatic Waves in Radio Zebra Models

Benáček, J., Karlický, M. 2019, Astrophysical Journal, 881, 21.

In this paper, we analyzed dispersion branches of the electrostatic waves in the upper-hybrid band. In the magnetized plasma, a series of the electrostatic branches is generated. The branches appear approximately at the multiples of the cyclotron frequency. Although the upper-hybrid branch usually approximates the branches near the plasma frequency, the position of the branches in $\omega-k_{\perp}$ domain is not the same. The difference in the frequency is essential for calculating the right values of growth rates.

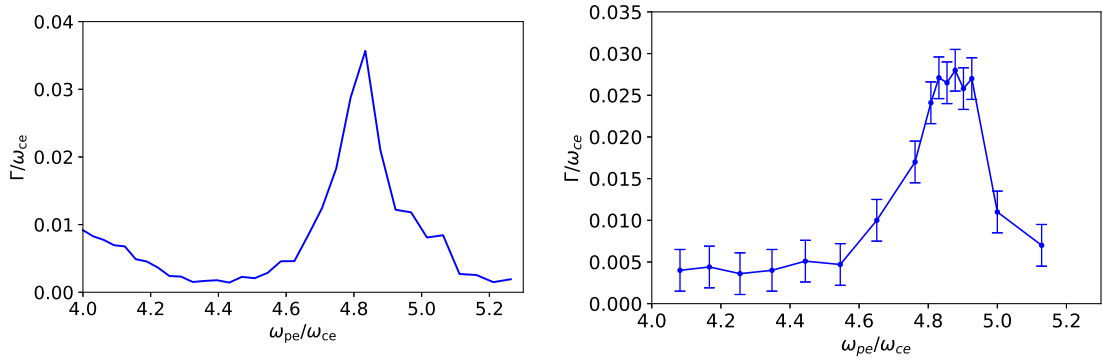


Figure 4.5: The comparison of the growth rates using different techniques. *Left:* The numerically integrated analytical growth rates when taking into account the “specific width” of the electrostatic branches. *Right:* The growth rates of the electrostatic energy estimated from the PIC model.

We computed the growth rates γ of all electrostatic branches and found, that almost all the branches go through the positive growth rate region. We calculated the growth rates as a maximum found at all the electrostatic branches. The result is that the growth rates in the dependence on the ratio ω_{pe}/ω_{ce} are almost flat, and no peaks are formed. This is in a disagreement not only with the general theory of the formation of the radio zebras, but also with the PIC results.

We introduced a new quantity called the integrated growth rate Γ , which takes into account the different “specific widths” of the branches in the frequency. It is assumed that this “specific width” is a product of the particle thermal motion which causes small fluctuations in the plasma frequency. Because of that, the positions of the electrostatic branches are also slightly varying. The “specific width” is different for the electrostatic branches at different harmonics, but it is also changing along each branch. We assumed that the amount of the carried energy is proportional to this “specific width”.

We found that the branches near the plasma frequency are the widest. With increasing the branch frequency distance from the plasma frequency (to lower or higher frequencies), the branch width is increased by several orders. In contrast with the growth rate γ , the integrated growth rate Γ forms significant peaks. The peak is formed when a sufficiently wide dispersion branch crosses the positive growth rate region through enough length. We showed the effects of the background plasma and the hot electron temperatures.

Because the PIC model includes all the electrostatic branches, we computed the growth rates using it. The resulting PIC growth rates are very similar to our integrated growth rates. We found a very good agreement between the theory and the simulation. The growth rate forms a peak at the

same position and has similar values as the result of the PIC simulations. The comparison between the PIC growth rate and the integrated growth rate is in Figure 4.5.

Conclusions

The Sun is our closest star and an essential element for the life on Earth. Although from the public point of view, the Sun is continually shining on Earth every day, it is actively influencing its surrounding. The humans are protected from the X-ray, the γ -ray radiation and the energetic particles by the atmosphere and the magnetosphere. But the radiation and the particles are influencing satellites in the space, the long power lines or people flying in an airplane near the magnetic poles.

Although there are several astronomical devices and probes monitoring the Sun, we are still not able to predict the most powerful energy releases — the solar flares. To predict the impact of the solar activity on Earth, we have to be able to understand not only the flare energy release processes, but also the processes in the solar wind, the interplanetary space, and in the near-Earth environment. The observations of solar radio bursts are the foundation for the understanding of the kinetic plasma processes in solar activity, solar flares, and in the corresponding plasma instabilities and the propagation of the observed radio emission. The gained knowledge can be used not only for understanding of solar flares but also in similar processes in the magnetospheres of planets and the laboratory plasma applications.

In this doctoral thesis, we studied the solar radio zebras. The radio zebra are fine structures occurring during the Type IV radio bursts. Because of the frequency width of the stripes, it is assumed that they are generated by the plasma emission processes. For their study, we used the most probable model based on the double plasma resonance instability. This model assumes the unstable loss-cone type velocity distribution of the hot electrons that are formed in the magnetic loop with the magnetic mirror. The cold and dense electrons in the background plasma give the properties of the electrostatic waves, while the unstable loss-cone determines the growth rates of these waves. It is assumed that the growth rates form peaks at specific frequencies. Then, the corresponding electromagnetic radio emission is proportional to the growth rates, and therefore, the radio zebra stripes are generated at the same frequencies as the corresponding growth rate peaks.

We analytically computed and analyzed the growth rates of the electrostatic waves dependent on the temperature of the hot and the background electrons. We used the DGH distribution function. We found that the growth rate peaks are shifted towards the lower values of ω_{pe}/ω_{ce} . Increasing the temperature of the hot electrons, the growth rate peaks become smoother and for the temperatures $v_t \sim 0.3 c$ they disappear. The temperature of the background component has only a small impact. We also analyzed the growth rates for other distribution functions — the loss-cone kappa and the loss-cone power-law.

We computed the saturation energies, temporal changes in the velocity distribution function, and the wavelengths using the three-dimensional electromagnetic relativistic PIC model. We found that the electrostatic energy is around 0.1 % of the initial kinetic energy of the superthermal electrons. From the knowledge of the energy density of the electrostatic waves and the zebra pattern observation, we estimated the conversion efficiency of the energy from the electrostatic waves into the electromagnetic ones. The electromagnetic waves close to the plasma frequency are emitted into the very narrow cone towards the observer (radiotelescopes on the Earth). During this process,

the distribution function of the hot electrons is changing due to the energy loss. The electron kinetic energy is decreasing in the perpendicular direction to the magnetic field. The resonance ellipses form the regions of a velocity decrease in agreement with the analytical theory. Many electrostatic branches are formed in the $\omega-k_{\perp}$ domain. We found that most of them cross the positive growth rates area. For comparison of the analytical results with the PIC simulations, we introduced the frequency “specific width” and the integrated growth rate. If we assume, that the amount of the carried energy of each dispersion branch is proportional to it “specific width”, most of the energy is carried by the branches near the plasma frequency.

Although we now understand the electrostatic growth rates in more details, a lot of work still needs to be done. For example, from the theoretical point of view, the energy transfer from the electrostatic waves into the electromagnetic radiation is still very poorly understood. That is a general problem of the radio bursts generated by the plasma emission mechanisms. From the observational point of view, except some first attempts, the spatial observations of the zebras are still missing. Such observation would give us information about the zebra’s formation, what the size of the zebra source and the best model are.

Appendix A

Temperature dependent growth rates of the upper-hybrid waves and solar radio zebra patterns

J. Benáček¹, M. Karlický², and L. V. Yasnov³

¹ Department of Theoretical Physics and Astrophysics, Masaryk University, Kotlářská 2, 611 37 Brno, Czech Republic
 e-mail: jbenacek@physics.muni.cz

² Astronomical Institute of the Czech Academy of Sciences, Fričova 258, 251 65 Ondřejov, Czech Republic

³ St.-Petersburg State University, 198504 St.-Petersburg, Russia

Received 14 September 2016 / Accepted 24 November 2016

ABSTRACT

Context. The zebra patterns observed in solar radio emission are very important for flare plasma diagnostics. The most promising model of these patterns is based on double plasma resonance instability, which generates upper-hybrid waves, which can be then transformed into the zebra emission.

Aims. We aim to study in detail the double plasma resonance instability of hot electrons, together with a much denser thermal background plasma. In particular, we analyse how the growth rate of the instability depends on the temperature of both the hot plasma and background plasma components.

Methods. We numerically integrated the analysed model equations, using Python and Wolfram Mathematica.

Results. We found that the growth-rate maxima of the upper-hybrid waves for non-zero temperatures of both the hot and background plasma are shifted towards lower frequencies comparing to the zero temperature case. This shift increases with an increase of the harmonic number s of the electron cyclotron frequency and temperatures of both hot and background plasma components. We show how this shift changes values of the magnetic field strength estimated from observed zebras. We confirmed that for a relatively low hot electron temperature, the dependence of growth rate vs. both the ratio of the electron plasma and electron cyclotron frequencies expresses distinct peaks, and by increasing this temperature these peaks become smoothed. We found that in some cases, the values of wave number vector components for the upper-hybrid wave for the maximal growth rate strongly deviate from their analytical estimations. We confirmed the validity of the assumptions used when deriving model equations.

Key words. Sun: radio radiation – instabilities – methods: analytical

1. Introduction

Zebra patterns (zebras) are fine IV radio-burst type structures, observed during solar flares in the dm- and m-wavelength ranges (Slottje 1972; Chernov et al. 2012). They are considered to be an important source of information about the plasma density and intensity of the magnetic field in their sources.

There are many zebra models (Rosenberg 1972; Kuijpers 1975; Zheleznyakov & Zlotnik 1975; Chernov 1976, 1990; LaBelle et al. 2003; Kuznetsov & Tsap 2007; Bárta & Karlický 2006; Ledenev et al. 2006; Laptukhov & Chernov 2009; Tan 2010; Karlický 2013). The most promising one is based on the double plasma resonance instability of the plasma, together with loss-cone type electron distribution function (Zheleznyakov & Zlotnik 1975; Zlotnik 2013). In this model, the upper-hybrid waves are first generated, then transformed to electromagnetic (radio) waves with the same (fundamental branch) or double frequency (harmonic branch) as the upper-hybrid waves. This model has the simple resonance condition

$$\omega_{UH} \approx s\omega_B, \quad (1)$$

where $\omega_{UH} = \sqrt{\omega_p^2 + \omega_B^2}$ is the upper-hybrid frequency of the background plasma, ω_p and ω_B are electron-plasma and electron-cyclotron frequencies and s is a integer harmonic number, is used for estimations of the magnetic field strength and electron plasma density in zebra radio sources (Ledenev et al. 2001; Zlotnik 2013; Karlický & Yasnov 2015). However, this

resonance condition is only valid in the zero-temperature limit. If we want to analyse effects of temperatures on the zebra generation processes, we need to take the resonance condition in its general form, see relation 3.

In this paper we study these temperature effects in detail. It is shown that these effects require a correction in the method used to estimate magnetic field strength in zebra radio sources, especially for zebra stripes at high harmonics.

The paper is structured as follows: in Sect. 2 we present model equations describing the double plasma resonance instability and methods of their solution. Results are summarized in Sect. 3. Finally, the paper is completed by discussions and conclusions in Sects. 4 and 5.

2. Model

Similarly to Winglee & Dulk (1986), Yasnov & Karlický (2004), for the hot electron component we consider the DGH distribution function with the parameter $j = 1$ (Dory et al. 1965)

$$f = \frac{u_{\perp}^2}{2(2\pi)^{3/2}v_t^5} \exp\left(-\frac{u_{\perp}^2 + u_{\parallel}^2}{2v_t^2}\right), \quad (2)$$

where $u_{\perp} = p_{\perp}/m_e$ and $u_{\parallel} = p_{\parallel}/m_e$ are electron velocities and p_{\perp} and p_{\parallel} are components of the electron momentum perpendicular and parallel to the magnetic field, and m_e is the electron

mass. For simplification and in agreement with [Winglee & Dulk \(1986\)](#), we call v_t here the thermal velocity of hot electrons and we use the term the temperature of hot electrons, although the distribution function in relation 2 is not Maxwellian.

Unlike [Winglee & Dulk \(1986\)](#), we included the background plasma with non-zero temperature. Its density n_b is assumed to be much greater than the density of the hot electrons n_h .

In agreement with the approach by [Melrose & Dulk \(1982\)](#), [Winglee & Dulk \(1986\)](#), [Yasnov & Karlický \(2004\)](#), we use the condition for double plasma resonance instability in the form

$$\omega_{UH} - \frac{k_{\parallel} u_{\parallel}}{\gamma} - \frac{s \omega_B}{\gamma} = 0, \quad (3)$$

where $\omega_{UH} = \sqrt{\omega_p^2 + \omega_B^2 + 3k^2 v_{tb}^2}$ is the upper-hybrid frequency of the background plasma, where the temperature effect is included, v_{tb} is the thermal velocity of the background plasma, $\gamma = \sqrt{1 + u^2/c^2}$ is the Lorentz factor, k is the absolute value of the wave number vector. Its components k_{\parallel} and k_{\perp} are in parallel and perpendicular directions to the magnetic field.

Then, starting from the basic equations presented in [Winglee & Dulk \(1986\)](#), [Yasnov & Karlický \(2004\)](#), we derived the relation for the growth rate Γ_{UH} of the upper-hybrid waves as

$$\frac{\Gamma_{UH}}{\omega_B n_h} = \frac{\pi^2 e^2}{\omega_B^2 m_e \sqrt{r_{pB}^2 + 1}} \sum_s \int_0^{u_{\perp, \max}} (h^+ + h^-) du_{\perp}, \quad (4)$$

$$h^{\pm} = \frac{s^2 G^{\pm} e^{-\frac{1}{2\sigma^2} (u_{\parallel}^2 + u_{\perp}^2)} J_s^2 \left(\frac{\sqrt{\lambda} u_{\perp}}{v_t} \right)}{2 \sqrt{2\pi} \lambda f^{\pm} v_t^5 (u_{\parallel}^2 + u_{\perp}^2 + 1)}, \quad (5)$$

$$f^{\pm} = \frac{s u_{\parallel}^{\pm} - \frac{u_{\perp}^2 + 1}{\sigma v_t}}{(u_{\parallel}^2 + u_{\perp}^2 + 1)^{3/2}}, \quad (6)$$

$$u_{\parallel}^{\pm} = \frac{1}{\beta} \left(\sigma s v_t \mp \sqrt{\beta + 1} \sqrt{-\beta (u_{\perp}^2 + 1) + \sigma^2 s^2 v_t^2} \right), \quad (7)$$

$$\beta = -1 + v_t^2 \sigma^2 (1 + r_{pB}^2) + 3 v_{tb}^2 (1 + \lambda \sigma^2), \quad (8)$$

where n_h is the hot electron density, e is the electron charge, r_{pB} is the ratio ω_p/ω_B , $J_s(x)$ is the Bessel function of first kind of s th order and λ, σ are dimensionless parameters

$$k_{\perp} = \sqrt{\lambda} \frac{\omega_B}{v_t}, \quad k_{\parallel} = \frac{\omega_B}{\sigma v_t}, \quad (9)$$

and G^{\pm} are functions

$$G^{\pm} = g_1 + g_2^{\pm}, \quad (10)$$

$$g_1 = s \left(-u_{\perp}^3 + 2 u_{\perp} v_t^2 \right), \quad (11)$$

$$g_2^{\pm} = \frac{u_{\perp}^3 u_{\parallel}^{\pm}}{s v_t \sqrt{u_{\parallel}^2 + u_{\perp}^2 + 1}}. \quad (12)$$

The term g_2^{\pm} comes from original relation of derivation distribution function of hot electrons ($k_{\parallel} u_{\perp} \partial f / \partial u_{\parallel} / \gamma$) ([Winglee & Dulk 1986](#), Eq. (A8)). As shown below, this term is negligible, and thus in our computations we use $G^{\pm} = g_1$.

The sum $h^+ + h^-$ expresses a simultaneous effect of the both operators h^+, h^- on one upper-hybrid wave described by the specific \mathbf{k} -vector. In our computations we used both operators, but we found that term h^- was always at least two orders lower than h^+ and the typical difference was ten orders.

Equations (4)–(8) are valid for $k_{\perp} \gg k_{\parallel}$, see [Winglee & Dulk \(1986\)](#). We note that comparing these relations with those in the paper by [Yasnov & Karlický \(2004\)](#) the growth rate (relation 5, $G^{\pm} = g_1$) is proportional to s^3 , not to s^2 .

The integration is done for velocities up to their maxima

$$u_{\perp, \max} = \frac{\sqrt{-1 + (1 + r_{pB}^2 - s^2) v_t^2 \sigma^2 + 3 v_{tb}^2 (1 + \lambda \sigma^2)}}{\sqrt{1 - (1 + r_{pB}^2) v_t^2 \sigma^2 - 3 v_{tb}^2 (1 + \lambda \sigma^2)}}, \quad (13)$$

from which we get the following conditions for maximal and minimal value of λ and σ (expressions under root in previous equations equal zero):

$$\sigma_{\max}(v_t, v_{tb}, s, \lambda) = \frac{\sqrt{1 - 3 v_t^2}}{\sqrt{(1 + r_{pB}^2 - s^2) v_t^2 + 3 v_{tb}^2 \lambda}}, \quad (14)$$

$$\sigma_{\min}(v_t, v_{tb}, s, \lambda) = \frac{\sqrt{1 - 3 v_t^2}}{\sqrt{(1 + r_{pB}^2) v_t^2 + 3 v_{tb}^2 \lambda}}, \quad (15)$$

$$\lambda_{\min}(v_t, v_{tb}, s) = \frac{(-1 - r_{pB}^2 + s^2) v_t^2}{3 v_{tb}^2}. \quad (16)$$

For the comparison below, we add values of σ and λ for the maximal growth rate as follows from analytical estimations made by [Winglee & Dulk \(1986\)](#)

$$\sigma_{\Gamma_{\max}} = \frac{1}{\sqrt{2(r_{pB}^2 + 1) v_t^2}}, \quad (17)$$

$$\lambda_{\Gamma_{\max}} = \frac{s^2}{2}, \quad (18)$$

when we suppose $u_{\perp, \max} = \sqrt{2} v_t$.

2.1. Methods

We used Python SympPy¹ library for analytical application and Python SciPy² library for numerical computations of growth rate Eqs. (4)–(8), (13)–(16).

Generally, the analytical expressions for the growth rate (relations 4–8) depend on $v_t, v_{tb}, \lambda, \sigma, s$ and r_{pB} . Their numerical solutions are made in several steps as described below.

First of all is the choice of thermal velocities v_t, v_{tb} . Then we selected the r_{pB} interval in which computations are made and steps in this interval. We usually use the interval $r_{pB} = 3-20$ with the step as $\Delta r_{pB} = 0.03$.

For each value of r_{pB} we searched for s which fulfill $s = s_0 - m, \dots, s_0 + n$, where $s_0 = \text{Round}(r_{pB})$ is the round value of r_{pB} . Numbers $m, n \in \mathbb{N}$ creates the interval of s for which the growth rate can be computed. However, we limited this interval only for s , maximal values of the growth rate of this interval are at least one hundredth of the maximal growth rate for s_0 .

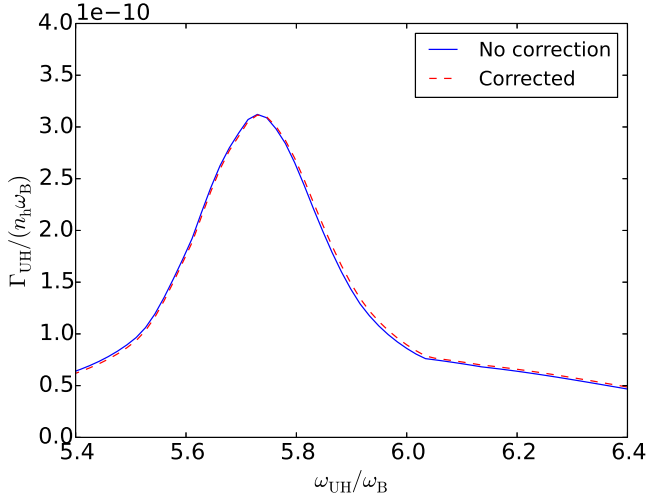
Next, values of v_t, v_{tb}, r_{pB} and s were chosen, and values of remaining variables λ and σ , which correspond to the \mathbf{k} -vector components of the upper-hybrid waves, need to be specified. We chose these values in the intervals $\sigma \in (\sigma_{\min}, \sigma_{\max})$ and $\lambda \in (\lambda_{\min}, \lambda_{\max})$ on equidistant lattice. If the maximal values of σ_{\max} and λ_{\max} are too large or not defined, the upper boundaries are

¹ <http://www.sympy.org>

² <http://www.scipy.org>

Table 1. Computation parameters.

Model No.	v_t	v_{tb}
1	0.1 c	0.018 c
2	0.1 c	0.009 c
3	0.1 c	0 c
4	0.2 c	0.018 c
5	0.3 c	0.018 c

**Fig. 1.** Example of the comparison of the growth rates computed with and without the term g_2^\pm (Eq. (5)), for Model 1 and $s = 6$. We note that the growth rate at this and following figures are normalized by the term $n_h \omega_B$.

chosen as ten times of their minimal values. It was found to be sufficient in all cases.

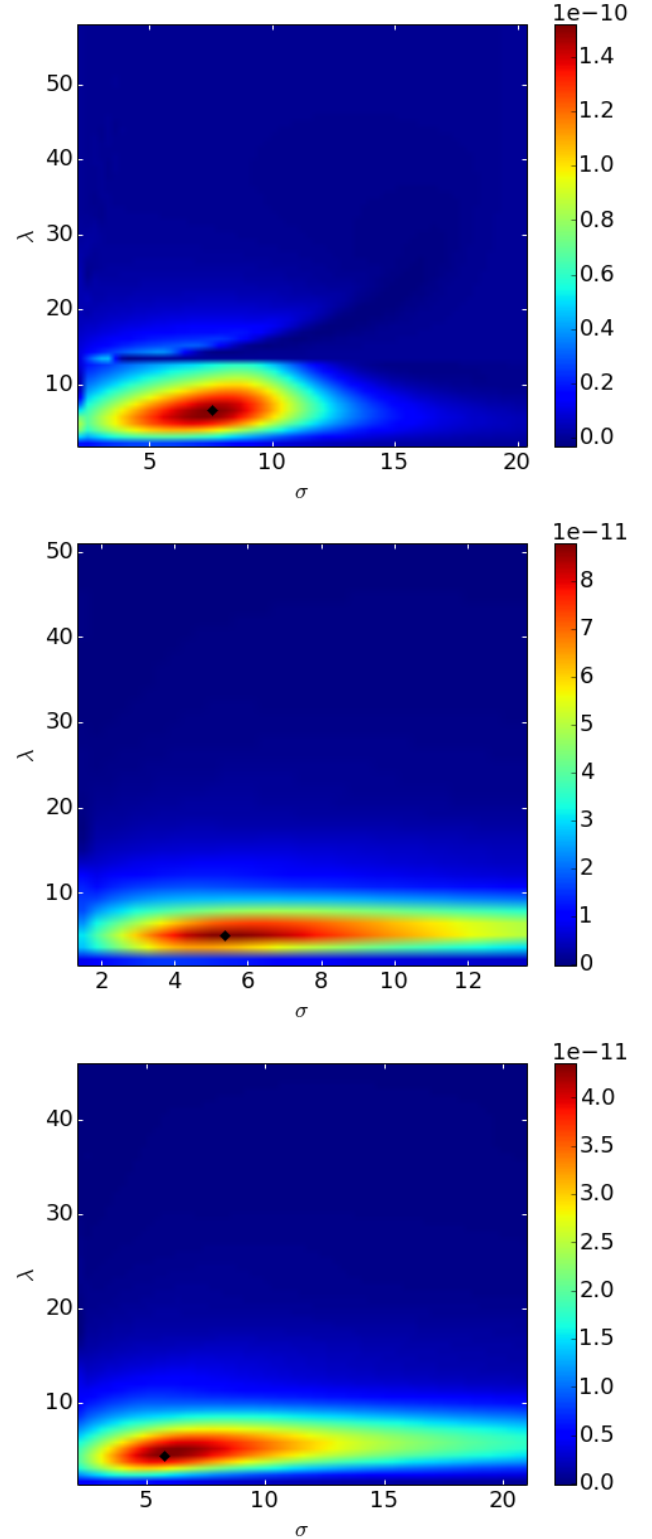
Only then it is possible to compute the growth rate given by relations between four and eight for parameters v_t , v_{tb} and r_{pb} for each s and in all points of the map $\lambda - \sigma$. In following step we summed the maps in each specific $(\lambda - \sigma)$ -point over s . Finally, in the resulting map we searched for the point $(\lambda_{\Gamma_{\max}}, \sigma_{\Gamma_{\max}})$, where is the highest value of the growth rate, which is then that determined for chosen r_{pb} . The wave number components of the upper-hybrid wave with the maximal growth rate is then determined by Eq. (9).

3. Results

We solved the above described equations for the parameters shown in Table 1, for $r_{pb} = 3-20$ and $B = 100$ G. In Models 1–3, we changed background temperature while temperature of the hot electrons remains constant. Models 4 and 5 consider higher temperatures of the hot electrons comparing with Model 1, while the temperature of the background plasma is fixed.

First, we tested an importance of the correction term g_2^\pm in Eq. (10) for computation of the growth rate. An example of such comparison is shown in Fig. 1. We found that in all models differences in values of the growth rate in models with and without this term is less than 5%, and at their maxima even smaller. Thus, we consider the effect of this term negligible and in all following computations we suppose $g_2^\pm = 0$.

In computations of the growth rate in all models (see Table 1) we followed steps described in Methods. Thus, we obtained many maps in the $\lambda - \sigma$ space, corresponding to the \mathbf{k} -vector

**Fig. 2.** Growth rates in the $\lambda - \sigma$ space: Model 1 (top), Model 4 (middle), Model 5 (bottom); all computed for $s = 6$ and r_{pb} , for which the growth rate is maximal. In Model 1 $r_{pb} = 5.8$, compare with Fig. 3. Black diamonds show positions of maximal values of the growth rate.

space. We note that the relations between the $\lambda - \sigma$ and \mathbf{k} -vector space is given by relation 9.

Examples of such maps for $s = 6$ at their maxima are shown in Fig. 2. In each of these maps the maximal growth rate is indicated. Then we summed the maps over s and in the resulting

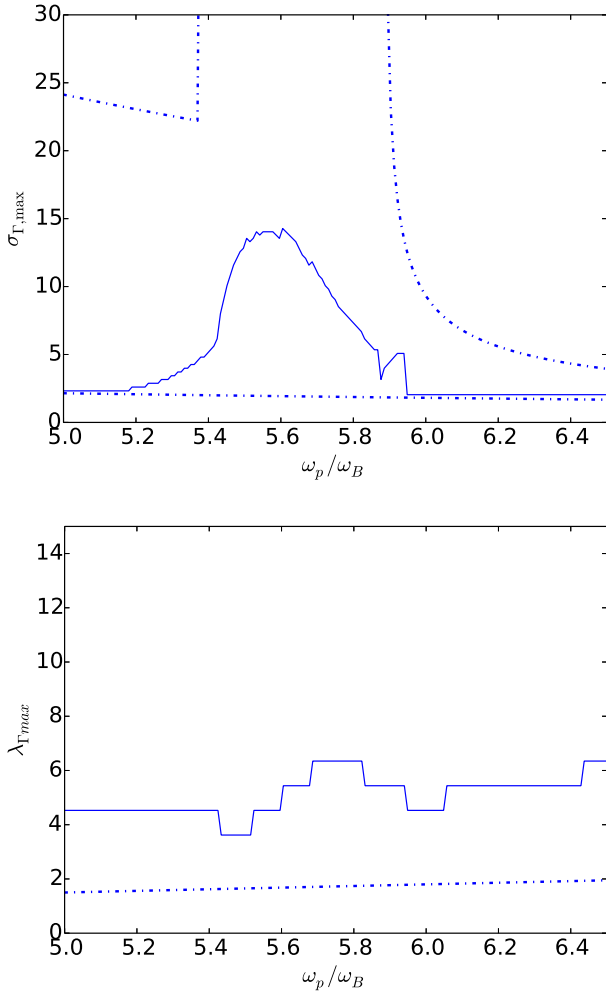


Fig. 3. Values of σ (top) and λ (bottom) for Model 1 and $s = 6$, where the growth rate has the maximal value depending on r_{pB} . Solid lines show values of the maximal growth rate, dash-dotted lines are boundaries of the $\sigma - \lambda$ space. Where dash-dotted lines are not shown, the boundaries are outside the presented region.

map we searched for the maximal growth rate. This growth rate then corresponds to one point of the curve in Fig. 4.

To compare the computed and analytically estimated (relations 17–18) \mathbf{k} -vectors, which correspond to the maximal growth rate for the cases presented in Fig. 2, these are shown in Table 2. Thus, the assumption ($k_{\perp} \gg k_{\parallel}$) used in derivation of the growth-rate relations was fulfilled in all studied Models. All computed \mathbf{k} -vectors are smaller than that analytically predicted. Their computed perpendicular components are systematically two times less than analytical ones. This is due to assumptions and simplifications made in analytical estimations of these values. Computed values of k_{\parallel} decrease with increasing temperature in contradiction with analytical predictions.

Examples of values $\sigma_{\Gamma,\max}$, $\lambda_{\Gamma,\max}$ for $v_t = 0.1$ c (Model 1), where the growth rate has the maximal value depending on r_{pB} , are presented in Fig. 3. Values of $\sigma_{\Gamma,\max}$ for $r_{pB} \sim 5$ and $r_{pB} > 6$ are close to the lower boundary (given by Eq. (15)). However, in the region around the growth-rate maximum they deviate from the lower boundary. Values of $\lambda_{\Gamma,\max}$ are changing only slightly. The steps in curves are due to discretisation of the $\lambda - \sigma$ space. Note that the value $\lambda_{\Gamma,\max} \approx 5$ (Fig. 3, bottom) is less than predicted value $s^2/2 = 18$.

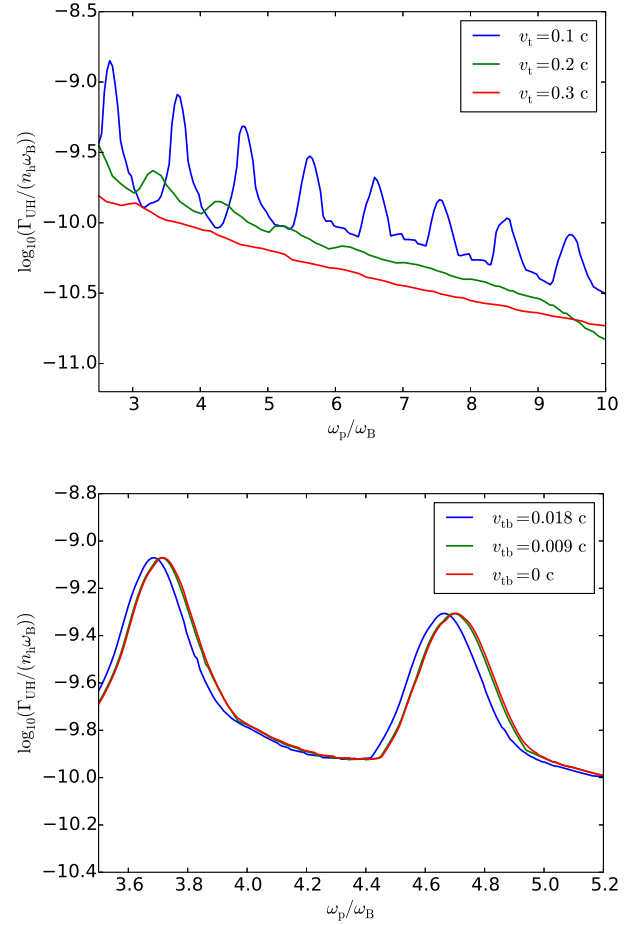


Fig. 4. Growth rates in Models shown in Table 1 in dependence on $r_{pB} = \omega_p/\omega_B$. Upper part: growth rates for Models 1, 4 and 5 with the fixed background temperature $v_{tb} = 0.018$ c. Bottom part: growth rates for Models 1–3 with the fixed temperature of hot electrons $v_t = 0.1$ c; detailed view.

Based on many such $\lambda - \sigma$ maps the growth-rate in dependence on the $r_{pB} = \omega_p/\omega_B$ were computed for all Models according to Table 1. These growth rates are shown in Fig. 4. The upper part of this figure shows an effect of the temperature increase of the hot electrons for fixed temperature of the background plasma electrons, and its bottom part an effect of the temperature increase of the background plasma electrons for fixed temperature of hot electrons.

As seen in the upper part of this figure, Model 1 with the lower velocity of hot electrons have higher growth rates than those in Models 4 and 5 for all $r_{pB} = \omega_p/\omega_B$. Furthermore, the temperature increase of hot electrons smooths peak maxima in the growth rate. While Model 1 shows distinct maxima, in Model 5 the maxima for $s > 5$ are hardly recognisable.

On the other hand, the change of the thermal velocity of background electrons in Models 1–3 for fixed temperature of hot electrons (see the bottom part of the Fig. 4) do not change values of the growth rate, but the temperature increase shifts the maxima slightly to lower r_{pB} . The values of maxima generally decrease with an increase of r_{pB} .

As already mentioned, maxima of the growth rates are more distinct for lower temperatures of the hot electrons. Therefore in Fig. 5 we present ratios of these maxima and neighbouring minima of the growth rate in dependence on s . We note that there is a simple relation between s and r_{pB} ; $s = \sqrt{r_{pB}^2 + 1}$. As seen in

Table 2. Positions of maximal growth rates (diamonds) from Fig. 2 in k -space for $s = 6$. All values agrees $k_{\parallel} \ll k_{\perp}$.

Model No.	k_{\parallel} [cm ⁻¹]	$k_{\parallel, \text{theor}}$ [cm ⁻¹]	k_{\perp} [cm ⁻¹]	$k_{\perp, \text{theor}}$ [cm ⁻¹]
1	0.078	0.049	1.49	2.48
4	0.054	0.086	0.66	1.24
5	0.034	0.117	0.41	0.83

Notes. Computed values are lower than analytically predicted.

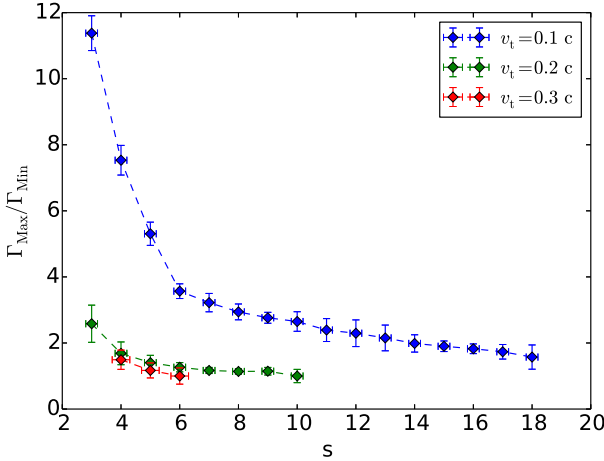
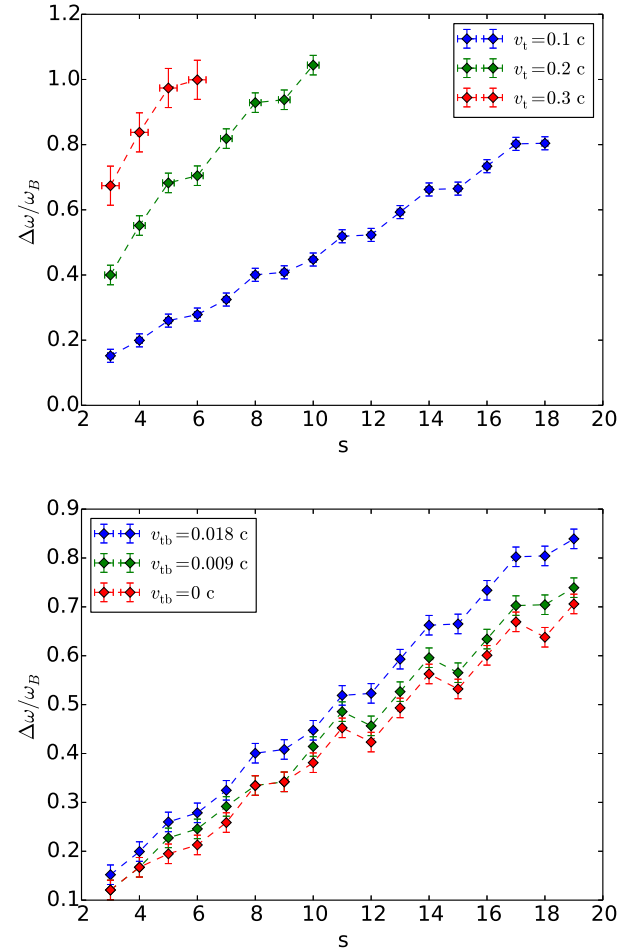
**Fig. 5.** Ratio between maxima and minima of growth rate depending on s for Models 1, 4 and 5.

Fig. 5, the ratios decrease with increasing s . It does not depend on the temperature of background electrons.

There is another interesting effect of temperatures of the both hot and background plasma electrons. Namely, by increasing these temperatures, the growth-rate maxima are shifted to lower frequencies as shown in Fig. 6.

In Fig. 7 we present this effect in a way that is more appropriate for zebra pattern analysis. Here we show growth-rate dependence on the ratio $\omega_{UH}/\omega_B = s$ for Model 1, meaning that, with the magnetic field intensity $B = 100$ G ($f_B = \omega_B/2\pi = 280$ MHz) and for the model with similar parameters as in Model 1, except that the magnetic field intensity is $B = 10$ G ($f_B = \omega_B/2\pi = 28$ MHz). At the horizontal axis of this figure we used the ratio ω_{UH}/ω_B , because ω_{UH} can be directly determined from frequencies of the observed zebra stripes. As shown here, the growth-rate maxima do not correspond to a simple resonance conditions (relation 1), which is used in estimations of the magnetic field and plasma density in the zebra radio sources from observed zebras. The maxima are shifted to lower frequencies, and this shift increases with the increase of s . Moreover, as seen in Fig. 7, the relative bandwidth of the growth-rate maxima also increases with the increase of s .

We also analyzed an effect of summation over s in relation 4 in comparison with the case for s with the maximal growth rate, see Fig. 8 made for Models 1 and 5. As seen here, for lower temperatures v_t the summation increases values of the growth-rate minima and for higher temperatures the growth rate is enhanced in the whole range. We found that if for a given s the growth rate decreases steeply from its maximum (the case with lower v_t), the summation is important at places where the individual orders overlap. But if the decrease of the growth rate from its maximum is gradual (the case with higher v_t), the summation influences the growth rate in a broad range of r_{pB} .

**Fig. 6.** Relative frequency shift $\Delta\omega$ of growth-rate maxima between predicted values by $\omega_{UH} = s\omega_B$ and its computed position (see Fig. 4). *Top:* Models 1, 4 and 5 with changing hot electrons temperature; *bottom:* Models 1–3 with changing background temperature.

4. Discussion

In the present paper we studied effects of non-zero temperatures of the both hot and background plasma on the growth rate. We showed that including effects of non-zero temperatures leads to shifts in the growth-rate maxima to lower frequencies, comparing frequencies derived from the simple resonance condition $\omega_{UH} = s\omega_B$. We found that these shifts are greater for higher values of the cyclotron harmonic number s . Because the simple resonance condition is used in estimations of the magnetic field and plasma density in the zebra radio sources, these shifts influence such estimations.

Therefore, let us estimate an error in the magnetic field determination from some zebra stripes using the simple resonance condition. For this purpose, let us assume the zebra stripe on the frequency $f = f_{UH} = \omega_{UH}/2\pi = 504$ MHz (assuming the emission on the fundamental frequency) with $s = 18$. If we use the simple resonance condition then for such high s the ratio of $r_{pB} = \omega_p/\omega_B \approx s$, and thus $f_B = \omega_B/2\pi = 28$ MHz, which gives the magnetic field $B = 10$ G, see also Fig. 7. But, for modified Model 1 with $B = 10$ G we found that the emission maximum for $s = 18$ is shifted to $\omega_{UH}/\omega_B = 17.3$. From observations, we have $f_{UH} = \omega_{UH}/2\pi = 504$ MHz, thus $f_B = 504/17.3 \approx 29.1$ MHz, which gives the magnetic field $B = 10.4$ G. This example shows a 4% error in magnetic field estimation. As shown in Fig. 6, the shift of the growth rates grows linearly with s . However, the

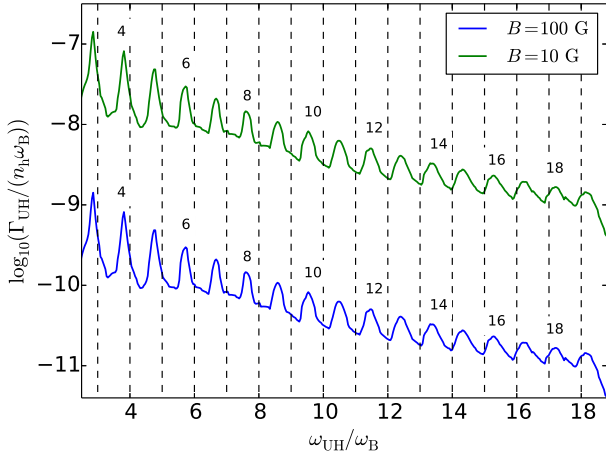


Fig. 7. Growth rate for Model 1 ($B = 100$ G, $f_B = \omega_B/2\pi = 280$ MHz) (blue line) and the model with similar parameters to Model 1, except the magnetic field intensity $B = 10$ G ($f_B = \omega_B/2\pi = 28$ MHz) in dependence on ω_{UH}/ω_B . Numbers close the growth-rate maxima designate s from computations. We note that the growth rate at this figure is normalized by the term $n_h \omega_B$.

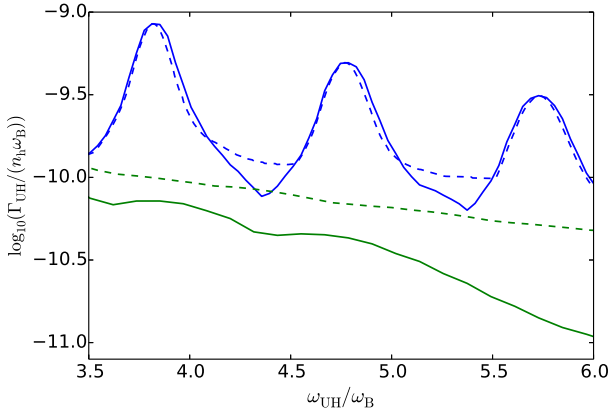


Fig. 8. Comparison of the growth rates with summation over s and for s with the maximal growth rate, for Model 1 (blue line) and Model 5 (green line). Dashed lines show summation over s and solid lines correspond to s with the maximal growth rate.

relative error of determining the magnetic field does not depend on s . For higher temperatures of hot electrons errors in magnetic field estimations are larger. For example, for Model 4 (recognisable maxima only for $s < 11$) this error is $\approx 16\%$.

The growth rate is proportional to the density of the hot plasma n_h and inversely proportional to the magnetic field. If we multiply the growth rate for Model 3 (with zero temperature of the background plasma), expressed in our paper as $\Gamma_{UH}/(\omega_B n_h)$ by the density $n_h = 10^8 \text{ cm}^{-3}$ we obtain the growth rate, which agrees with that by (Winglee & Dulk 1986).

In agreement with the results by Yasnov & Karlický (2004) we found that for a relatively low temperature of the hot electrons (Model 1) the dependence of the growth rate vs. the ratio of the electron plasma and electron cyclotron frequencies expresses distinct peaks and increasing this temperature (Models 4 and 5) these peaks are smoothed, especially for high s . This growth-rate behaviour differs from those in previous studies (Zheleznyakov & Zlotnik 1975; Winglee & Dulk 1986). The difference is caused by relativistic corrections used in the present

paper in both resonance terms in Eq. (3) and in selection of maximal growth rates in k -maps. We note that a similar effect in growth-rate behaviour was found by Kuznetsov & Tsap (2007). Namely, considering the power-law and loss-cone distribution function of hot electrons, they showed that stripes of a zebra pattern become more pronounced with an increase of the loss-cone opening angle and the power-law spectral index.

We also studied effects of the neglected term in the growth rate with $\frac{\partial f}{\partial u_{||}}$ (Winglee & Dulk 1986, Eq. (A8)). We found that these effects are negligible.

5. Conclusions

We found that the growth-rate maxima of the upper-hybrid waves for non-zero temperatures of the both hot and background plasma are shifted towards lower frequencies comparing to the zero temperature case. It was found that this shift increases with an increase of the harmonic number s of the electron cyclotron frequency and temperatures of the both hot and background plasma components.

We showed that this shift of the growth-rate maxima influences estimations of the magnetic field strength in sources of observed zebras. In agreement with previous studies we found that for a relatively low temperature of the hot electrons the dependence of the growth rate vs. the ratio of the electron plasma and electron cyclotron frequencies expresses distinct peaks and increasing this temperature these peaks are smoothed.

We found that in some cases the values of components of the wave number vector of the upper-hybrid wave for the maximal growth rate strongly deviate from their analytical estimations. Validity of the assumptions used in derivation of the model equations was confirmed.

Acknowledgements. The authors thank G. P. Chernov for useful comments. We acknowledge support from Grants P209/12/0103. Access to computing and storage facilities owned by parties and projects contributing to the National Grid Infrastructure MetaCentrum provided under the programme “Projects of Projects of Large Research, Development, and Innovations Infrastructures” (CESNET LM2015042), is greatly appreciated. L.Y. acknowledges support by the RFBR grant (No. 16-02-00254).

References

- Bárta, M., & Karlický, M. 2006, *A&A*, **450**, 359
- Chernov, G. P. 1976, *Sov. Astron.*, **20**, 449
- Chernov, G. P. 1990, *Sol. Phys.*, **130**, 75
- Chernov, G. P., Sych, R. A., Meshalkina, N. S., Yan, Y., & Tan, C. 2012, *A&A*, **538**, A53
- Dory, R. A., Guest, G. E., & Harris, E. G. 1965, *Phys. Rev. Lett.*, **14**, 131
- Karlický, M. 2013, *A&A*, **552**, A90
- Karlický, M., & Yasnov, L. V. 2015, *A&A*, **581**, A115
- Kuijpers, J. M. E. 1975, Ph.D. Thesis, Utrecht, Rijksuniversiteit, 72
- Kuznetsov, A. A., & Tsap, Y. T. 2007, *Sol. Phys.*, **241**, 127
- LaBelle, J., Treumann, R. A., Yoon, P. H., & Karlický, M. 2003, *ApJ*, **593**, 1195
- Laptukhov, A. I., & Chernov, G. P. 2009, *Plasma Phys. Reports*, **35**, 160
- Ledenev, V. G., Karlický, M., Yan, Y., & Fu, Q. 2001, *Sol. Phys.*, **202**, 71
- Ledenev, V. G., Yan, Y., & Fu, Q. 2006, *Sol. Phys.*, **233**, 129
- Melrose, D. B., & Dulk, G. A. 1982, *ApJ*, **259**, 844
- Rosenberg, H. 1972, *Sol. Phys.*, **25**, 188
- Slotje, C. 1972, *Sol. Phys.*, **25**, 210
- Tan, B. 2010, *Astrophys. Space Sci.*, **325**, 251
- Winglee, R. M., & Dulk, G. A. 1986, *ApJ*, **307**, 808
- Yasnov, L. V., & Karlický, M. 2004, *Sol. Phys.*, **219**, 289
- Zheleznyakov, V. V., & Zlotnik, E. Y. 1975, *Sol. Phys.*, **44**, 461
- Zlotnik, E. Y. 2013, *Sol. Phys.*, **284**, 579

Appendix B

Brightness Temperature of Radio Zebras and Wave Energy Densities in Their Sources

L.V. Yasnov¹ · J. Benáček² · M. Karlický³

Received: 5 February 2017 / Accepted: 11 September 2017 / Published online: 26 October 2017
© Springer Science+Business Media B.V. 2017

Abstract We estimated the brightness temperature of radio zebras (zebra pattern – ZP), considering that ZPs are generated in loops having an exponential density profile in their cross section. We took into account that when in a plasma there is a source emitting in all directions, then in the escape process from the plasma the emission has a directional character nearly perpendicular to the constant-density profile. Owing to the high directivity of the plasma emission (for emission at frequencies close to the plasma frequency), the region from which the emission escapes can be very small. We estimated the brightness temperature of three observed ZPs for two values of the density scale height (1 and 0.21 Mm) and two values of the loop width (1 and 2 arcsec). In all cases, high brightness temperatures were obtained. For the higher value of the density scale height, the brightness temperature was estimated to be $1.1 \times 10^{15} - 1.3 \times 10^{17}$ K, and for the lower value, it was $4.7 \times 10^{13} - 5.6 \times 10^{15}$ K. These temperatures show that the observational probability of a burst with a ZP, which is generated in the transition region with a steep gradient of the plasma density, is significantly higher than for a burst generated in a region with smoother changes of the plasma density. We also computed the saturation energy density of the upper-hybrid waves (according to the double plasma resonance model, they are generated in the zebra source) using a 3D particle-in-cell model with a loss-cone type of distribution of hot electrons. We found that this saturated energy is proportional to the ratio of hot electron and background plasma densities. Thus, comparing the growth rate and collisional damping of the upper-hybrid waves, we estimated minimum densities of hot electrons as well as the

J. Benáček
jbenacek@physics.muni.cz

L.V. Yasnov
l.yasnov@spbu.ru

M. Karlický
karlicky@asu.cas.cz

¹ St.-Petersburg State University, St.-Petersburg, 198504, Russia

² Department of Theoretical Physics and Astrophysics, Masaryk University, Kotlářská 2, 611 37 Brno, Czech Republic

³ Astronomical Institute, Academy of Sciences of the Czech Republic, 251 65 Ondřejov, Czech Republic

minimum value of the saturation energy density of the upper-hybrid waves. Finally, we compared the computed energy density of the upper-hybrid waves with the energy density of the electromagnetic waves in the zebra source and thus estimated the efficiency of the wave transformation.

Keywords Sun: corona · Sun: flares · Sun: radio radiation

1. Introduction

Fine structures of solar radio bursts are very important for understanding flare energy-release processes and diagnostics of the flare plasma. Of the various fine structures, the zebra structure (ZP – zebra pattern) is the most intriguing. It occurs in Type IV radio bursts. In radio spectra it appears as several parallel stripes distributed uniformly in frequency; see examples below. The number of these zebra stripes in a ZP is typically large ($> 5–8$, sometimes even exceeding 20).

There are still questions about the generation mechanism of these ZPs. Of the many proposed models (Zheleznyakov and Zlotnik, 1975; LaBelle *et al.*, 2003; Bárta and Karlický, 2006; Kuznetsov and Tsap, 2007; Tan, 2010; Karlický, 2013), the most commonly accepted model is that based on the double-plasma resonance (DPR) (Zlotnik, 2013; Karlický and Yasnov, 2015). Based on this model, most of the observed characteristics of ZPs were explained: the frequency range, polarization, amount of stripes and their frequencies, their high-frequency limit, and their temporal changes.

However, only a few estimations of the ZP brightness temperature have been reported so far, which is important for further specification of the generation mechanism of ZPs. For example, Chernov *et al.* (1994) estimated the brightness temperature of metric ZPs to be 10^{10} K, with the source size constrained by the Nançay radioheliograph.

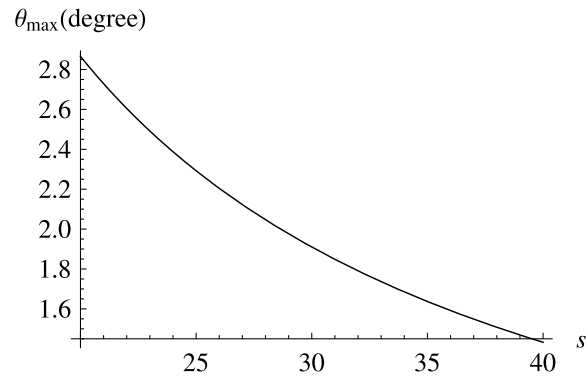
Another estimation of the ZP brightness temperature ($T_b = 10^{13}$ K) has been reported by Chernov, Yan, and Fu (2003), where the ZP consisted of spiky superfine structures; see also Chernov (2006). On the other hand, Chernov (2006) stated that the metric ZP radio sources occupy a notable part of the background continuum source or even the entire active region. The half-width of one source of the metric ZP was about 1.9 arcmin, which gives a brightness temperature of 10^{10} K.

Using the *Siberian Solar Radio Telescope* (SSRT), Altyntsev *et al.* (2005) observed a ZP burst at ≈ 5.7 GHz (the highest frequency ever reported for ZP emission), which yielded a lower limit of $T_b \approx 2 \times 10^7$ K.

Chen *et al.* (2011) estimated the lower limit for the decimetric ZP brightness temperature to be 1.6×10^9 K. Finally, Tan *et al.* (2014) estimated the brightness temperature of a decimetric ZP to be $T_b \approx 2 \times 10^{11}$ K.

In the present article we estimate the brightness temperature of a ZP, considering that a ZP is generated in a loop whose cross section has an exponential density profile. In this case, the ZP source size and brightness temperature depend on the loop cross-section size. Furthermore, using a 3D particle-in-cell model with a loss-cone type of distribution of hot electrons, we compute the energy density of the upper-hybrid waves. Then this energy density is compared with that of the electromagnetic waves, and thus the efficiency of the wave transformation (which is not well known) is estimated.

Figure 1 Maximum escape angle of the plasma emission in conditions of the double-plasma resonance depending on the gyroharmonic number s .



2. Sizes of the Zebra Source

If in a plasma there is a source emitting in all directions, then the emission during its escape process has a directional character. The range of angles $\leq \Theta_{\max}$ in which the emission escapes can be expressed as (Zheleznyakov, 1997)

$$\Theta_{\max} = \operatorname{arcsec}\left(\frac{\omega}{\omega_L}\right), \quad (1)$$

where ω_L is the plasma frequency in the source and ω is the emission frequency. In the conditions of a double-plasma resonance, the ratio of these frequencies is (Karlický and Yasnov, 2015)

$$\frac{\omega}{\omega_L} = \frac{s}{\sqrt{s^2 - 1}}, \quad (2)$$

where s is the gyroharmonic number.

In Figure 1 the maximum escape angle of the plasma emission for the double-plasma resonance in the dependance on the gyroharmonic number s is shown.

Owing to the high directivity of the plasma emission (for emission frequency close to the plasma frequency), the region from which the emission escapes can be very small. This is connected with the fact that the emission region in the flare loop at a fixed frequency is not flat because of the density inhomogeneity across the loop (the maximum density is expected at the loop axis). It has a convex form, and thus the emission with a high directivity (with a maximum value in the direction perpendicular to the constant-density layer) can reach an observer only from a limited region.

Watko and Klimchuk (2000) showed that the width of loops close to their footpoints, where the decimetric bursts are generated, is about 0.5 arcsec (0.36 Mm), and the typical width of higher loops is about 1 arcsec. Note that the decimetric ZPs are generated in loops at low heights (about 3 Mm) (Karlický and Yasnov, 2015; Yasnov, Karlický, and Stupishin, 2016). The width of some loops can be even smaller. For example, Peter *et al.* (2013) found tiny 1.5 MK loop-like structures that they interpreted as miniature coronal loops. Their coronal segments above the chromosphere have a length of only about 1 Mm and a thickness of less than 200 km. Moreover, Peter and Bingert (2012) showed that in a 3D self-consistent magnetohydrodynamic model of the solar corona, the loop width remains constant with height, and profiles of intensities along the loop radius correspond to Gaussian profiles. The Gaussian profile along the loop radius was also considered by Chernov *et al.* (1994). Kuznetsov and Kontar (2015) assumed a Gaussian function ($\exp(-r^2/a^2)$, where r is the loop radius and $a = 1$ arcsec) describing the electron distribution in the flare loop.

Therefore, in agreement with the above-mentioned articles, we assume that the density inside the magnetic loop at a specific height $[h_0]$ has the exponential form

$$n_e(r) = n_{\text{em}}(h_0) \exp\left(-\frac{r^2}{d^2}\right), \quad (3)$$

where n_{em} is the density at the loop axis, d is the loop width, and r is the radius across the loop. Moreover, the density in the loop decreases with height as $\approx \exp(-(h - h_0)/H)$, where h is the height in the solar atmosphere and H is the scale height. Thus, the density inside the loop can be expressed as

$$n_e(r, h) = n_{\text{em}}(h_0) \exp\left(-\frac{r^2}{d^2}\right) \exp\left(-\frac{h - h_0}{H}\right). \quad (4)$$

Now, we calculate the form of a layer with constant plasma density. For the height where this layer is located, we can write

$$C = n_{\text{em}}(h_0) \exp\left(-\frac{r^2}{d^2}\right) \exp\left(-\frac{h - h_0}{H}\right), \quad (5)$$

$$h(r) = h_0 - H \frac{r^2}{d^2} + H \ln\left(\frac{n_{\text{em}}(h_0)}{C}\right), \quad (6)$$

where C is a constant.

In a loop with constant magnetic field, it follows from the pressure equilibrium and density variations that the temperature varies, and thus also the scale-height. However, for simplification in further calculations, we assume that the scale-height $[H]$ inside the loop is constant.

Then the derivation of dh/dr is

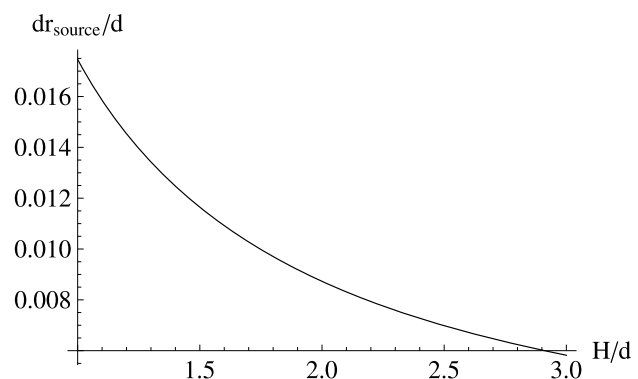
$$\frac{dh}{dr} = -\frac{2Hr}{d^2}. \quad (7)$$

When we use this derivation, the extent of the emission region for which the emission direction is nearly perpendicular to the constant-density profile can be estimated as

$$\Delta r_{\text{source}} = \frac{d^2 \tan(\Theta_{\text{max}})}{2H}, \quad (8)$$

where Θ_{max} is the maximum escape angle of the plasma emission according to Equation 1 (Figure 1). Note that the extent is independent of r . An example of the dependance of $\Delta r_{\text{source}}/d$ on H/d for $\Theta_{\text{max}} = 2^\circ$ is shown in Figure 2.

Figure 2 Source extent $[\Delta r_{\text{source}}/d]$ as a function of H/d for the emission nearly perpendicular (for the maximum escape angle $= 2^\circ$) to the constant-density profile.



The emission source is also extended in height. This dimension can be estimated as $h_s = H(df/f)$, where df is the bandwidth of the zebra stripe and f is the zebra-stripe frequency.

3. Estimations of the Brightness Temperature of Zebra Structures

Now, we estimate the brightness temperature of some observed ZPs. For this purpose, we selected three ZPs observed by the Ondřejov radiospectrograph (Jiricka *et al.*, 1993); see Figures 3, 4, and 5.

Figure 3 *Left panel:* Example of the zebra pattern observed by the Ondřejov radiospectrograph during the 2 May 1998 solar flare. *Right panel:* Radio-flux profile as a function of frequency at 14:29:27.3 UT.

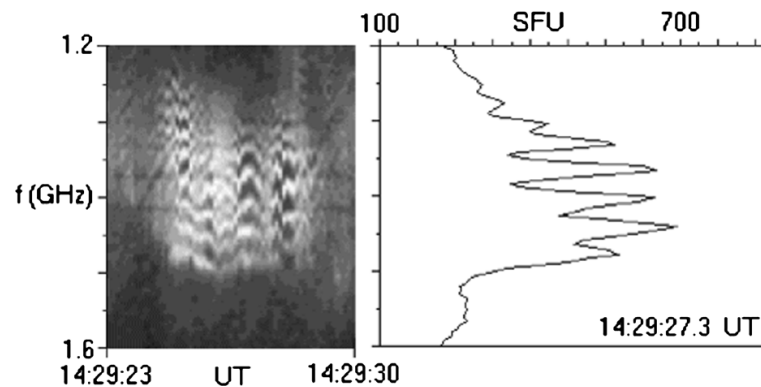


Figure 4 *Left panel:* Example of the zebra pattern observed by the Ondřejov radiospectrograph during the 14 February 1999 solar flare. *Right panel:* Radio-flux profile as a function of frequency at 12:08:57.7 UT.

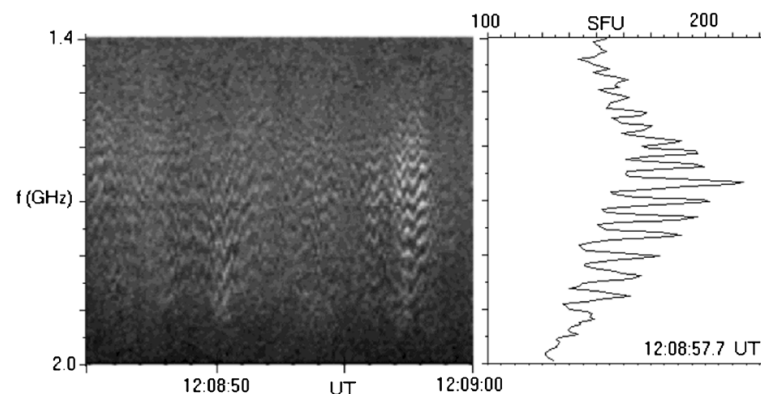


Figure 5 *Left panel:* Example of the zebra pattern observed by the Ondřejov radiospectrograph during the 6 June 2000 solar flare. *Right panel:* Radio-flux profile as a function of frequency at 15:43:12.6 UT.

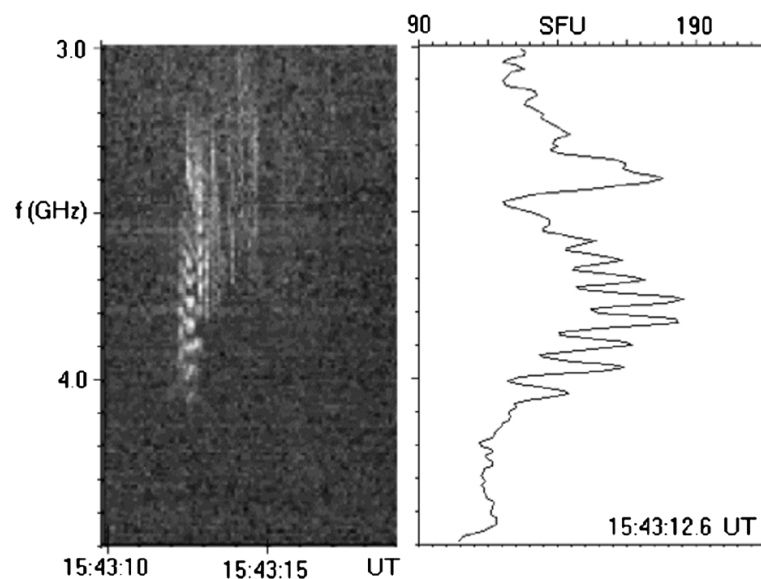


Table 1 ZP source parameters. S is the radio flux in SFU units and s_1 is the gyro-number of the stripe with the lowest frequency.

	ZP 2 May 1998	ZP 14 February 1999	ZP 6 June 2000
Event location	S15W15	N16E09	N23E15
S [SFU]	650	170	210
f_{GHz}	1.45	1.67	3.78
s_1	21	32	34
Θ_{max}	2.70	1.79	1.68
L_8 ($2d = 1$ arcsec)	0.0059	0.0038	0.0035
L_8 ($2d = 2$ arcsec)	0.023	0.015	0.014
T_b ($2d = 1$ arcsec)	13×10^{16} K	6×10^{16} K	1.7×10^{16} K
T_b ($2d = 2$ arcsec)	0.83×10^{16} K	0.39×10^{16} K	0.11×10^{16} K
Source height [km]	28	14.7	12.5

Table 2 ZP source parameters for $H = 0.21$ Mm

	ZP 2 May 1998	ZP 14 February 1999	ZP 6 June 2000
L_8 ($2d = 1$ arcsec)	0.028	0.018	0.017
L_8 ($2d = 2$ arcsec)	0.11	0.070	0.067
T_b ($2d = 1$ arcsec)	5.6×10^{15} K	2.7×10^{15} K	0.73×10^{15} K
T_b ($2d = 2$ arcsec)	0.36×10^{15} K	0.18×10^{15} K	0.047×10^{15} K

The brightness temperature can be expressed as (Zaitsev and Stepanov, 1983)

$$T_b = \frac{S}{7 \times 10^{-11}} \frac{1}{f_{\text{GHz}}^2 L_8^2}, \quad (9)$$

where S is the radio flux in SFU, f_{GHz} is the frequency in GHz, and L_8 ($= 2\Delta r_{\text{source}}$) is the dimension of the emission region in units of 10^8 cm.

To compute the brightness temperature, we therefore need to determine the source size [Δr_{source}]. First, using the method presented by Karlický and Yasnov (2015), we determined the gyroharmonic numbers s_1 for the observed zebras. Knowing s_1 (see Table 1) and considering the scale height as $H = 1$ Mm (according to the relation H [m] = $50 T$ [K] (Priest, 2014) for the temperature $T = 2 \times 10^4$ K), we calculated the source size of the observed zebras for two values of $2d$ (1 and 2 arcsec). All of the computed parameters of the zebra sources together with the brightness temperatures are shown in Table 1.

However, in a region with a rapid change of the plasma temperature, the scale height can be shorter. Therefore, we estimate the brightness temperature using the model by Selhorst, Silva-Válio, and Costa (2008). For typical densities in ZP sources of $5.0 \times 10^9 \text{ cm}^{-3}$ – $3.6 \times 10^{10} \text{ cm}^{-3}$, the model gives heights in the solar atmosphere of between 2.84 Mm and 3.27 Mm. Thus, the scale height is $H = 0.21$ Mm, which is almost five times shorter than that according to the formula of Priest used above. For this scale height, the ZP source parameters are given in Table 2.

Table 3 Energy densities of electromagnetic and upper-hybrid waves in the ZP source for the 2 May 1998 event. $\epsilon = W_{\text{elm}}/W_{\text{UH,min}}$ is the parameter expressing the efficiency of transformation of the upper-hybrid waves into electromagnetic waves.

L_8 [Mm]	W_{elm} [J m^{-3}]	$W_{\text{UH,min}}$ [J m^{-3}]	ϵ
0.0059	3.90×10^{-8}	4.40×10^{-5}	8.86×10^{-4}
0.023	2.57×10^{-9}	4.40×10^{-5}	5.84×10^{-5}
0.028	1.73×10^{-9}	4.40×10^{-5}	3.93×10^{-5}
0.11	1.12×10^{-10}	4.40×10^{-5}	2.54×10^{-6}

4. Energy Densities of Electromagnetic and Upper Hybrid Waves in the ZP Source

We consider the zebra observed during the 2 May 1998 event. Knowing the ZP radio flux (650 SFU) and the zebra line frequency width (40 MHz), and computing the ratio of the emission area at 1 AU (corresponding to the emission directivity angle (2.7° for $s = 21$, see Figure 1)), and ZP source area ($L_8 \times L_8$ for four cases according to Tables 1 and 2), the energy density of electromagnetic waves in the ZP source was calculated; see the second column in Table 3.

In the double-plasma resonance (DPR) model of ZPs, it is assumed that there are hot electrons with a loss-cone type distribution together with much denser background plasma in the ZP source. The distribution is unstable and generates the upper-hybrid waves, which after their transformation produce the observed ZPs.

In addition to estimating the energy density of electromagnetic waves, it is therefore highly desirable to estimate the energy density of the upper-hybrid waves in the ZP source. For this purpose, we used a 3D particle-in-cell (PIC) relativistic code (Buneman and Storey, 1985, Matsumoto and Omura, 1993, Karlický and Bárta, 2008). Although this code is very useful for these computations, it has its own limitations, which means that some parameters of the ZP of 2 May 1998 cannot be reproduced in the following PIC computations. For example, computing high gyro-harmonic numbers ($s > 20$ in our case) is problematic because it is very difficult to select PIC plasma parameters that reproduce resonances with high harmonic numbers, especially because of the discrete space (grids) in PIC models.

The size of the model is $L_x \times L_y \times L_z = \lambda \Delta \times \lambda \Delta \times 32\Delta$, where Δ is the grid size and λ is the wavelength of the upper-hybrid wave in resonance in normalized units. We chose a model containing only one wavelength of the upper-hybrid wave to simplify the processing and decrease computing time. The model time step was $dt = 1$, the plasma electron frequency was $\omega_{pe} dt = 0.05$, the initial magnetic field was in z -direction, and the electron-cyclotron frequency was, *e.g.*, $\omega_{ce} = 0.176 \omega_{pe}$ for the harmonic number $s = 7$. The harmonic number was considered in the interval $s = 4 - 18$. We used two groups of electrons: a) cold background electrons with a thermal velocity $v_{tb} = 0.03 c$ (c is the light speed), corresponding to a temperature 5.35 MK, and b) hot electrons with a DGH (Dory, Guest, and Harris, 1965) distribution function for $j = 1$ in the form

$$f = \frac{u_{\perp}^2}{2(2\pi)^{3/2}v_t^5} \exp\left(-\frac{u_{\perp}^2 + u_{\parallel}^2}{2v_t^2}\right), \quad (10)$$

where $u_{\perp} = p_{\perp}/m_e$ and $u_{\parallel} = p_{\parallel}/m_e$ are electron velocities, p_{\perp} and p_{\parallel} are components of the electron momentum perpendicular and parallel to the magnetic field, m_e is the electron mass, and $v_t = 0.2 c$ is the thermal spread in the velocities of hot electrons.

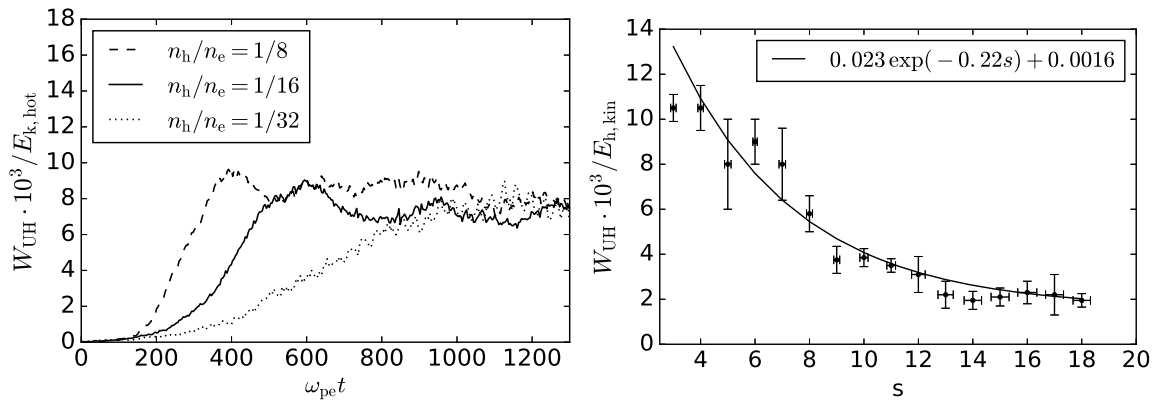


Figure 6 *Left:* Temporal evolution of the ratio of the energy of the upper-hybrid waves W_{UH} to the kinetic energy of hot electrons $E_{h,kin}$ for $s = 7$ and three values of n_h/n_e . *Right:* Ratio of the saturated energy of the upper-hybrid waves to the kinetic energy of hot electrons for $n_h/n_e = 1/8$ as a function of s . The *full line* shows the exponential fit.

The electron density of cold electrons *per cell* was taken to be $n_e = 1920$ and the ratio of hot and background plasma electrons was $n_h/n_e = 1/8$. We also made computations with $n_h/n_e = 1/16$ and $1/32$ to determine the dependence of the saturation energy of the upper-hybrid waves on the density ratio n_h/n_e . There were as many protons as electrons, and their temperature was the same as that of the cold electrons.

The results obtained with this PIC code are shown in the left panel of Figure 6: the temporal evolution of the energy of the upper-hybrid waves [W_{UH}], generated by hot electrons, for $s = 7$ and three values of n_h/n_e . The ratio of the saturated energy of the upper-hybrid waves to the kinetic energy of hot electrons is the same in all three cases ($W_{UH} = 8 \times 10^{-3} E_{h,kin}$). This means that the saturated energy of the upper-hybrid waves is proportional to the n_h/n_e ratio because $E_{h,kin}$ depends on n_h . The saturated energy of the upper-hybrid waves also depends on s , as shown in the right panel of Figure 6. The computed values can be well fit by the exponential fit. Therefore, for the 2 May 1998 zebra that was analyzed, where $s = 21$, we used this exponential fit, which gives the value of the saturated energy of the upper-hybrid waves as $W_{UH} = 1.6 \times 10^{-3} E_{h,kin}$, where $E_{h,kin}$ is the kinetic energy of the hot electrons.

For the following estimations, we derived the minimum value of the parameter n_h/n_e . For this purpose we used the analytical expression for the growth rate of the upper-hybrid waves as derived by Thejappa (1991):

$$-\gamma_{UH} \approx 4.4 \times 10^{-2} \omega_{pe} \frac{n_h}{n_e}. \quad (11)$$

This growth rate agrees with the rate in our PIC simulations. To generate the upper-hybrid waves, this growth rate needs to be greater than the damping of these waves by collisions,

$$\gamma_c = 2.75 \frac{n_e}{T_e^{3/2}} \ln(10^4 T_e^{3/2} / n_e^{1/3}), \quad (12)$$

where T_e is the background plasma temperature. Thus, when we set γ_{UH} equal to γ_c , then for the mean ZP frequency (1.45 GHz and corresponding plasma density $n_e = 2.6 \times 10^{16} \text{ m}^{-3}$) and for a T_e in the ZP source of $2 \times 10^4 \text{ K}$ (at the bottom of the transition region), the minimum ratio of n_h/n_e is 4.93×10^{-4} .

When we take the density of the hot electrons in the ZP source as equal to the minimum density $n_h = 2.6 \times 10^{16} \times 4.93 \times 10^{-4} = 1.28 \times 10^{13} \text{ m}^{-3}$ and use the extrapolated value

of the saturated energy of the upper-hybrid waves for $s = 21$ and the linear dependance of the saturated energy of the upper-hybrid waves on n_h , found in the PIC simulations, the minimum energy density of the upper-hybrid waves [$W_{UH,min}$] is calculated; see the third column in Table 3.

Moreover, when we assume that the energy density of the upper-hybrid waves in the ZP source from 2 May 1998 is the same as $W_{UH,min}$, we can calculate the parameter expressing the transformation efficiency of the upper-hybrid waves into electromagnetic waves; see the last column in Table 3. However, the ratio n_h/n_e in real conditions needs to be greater than its minimum value, and therefore ϵ in real conditions should be lower. On the other hand, values of the parameter ϵ would be greater if we considered the absorption of the electromagnetic waves near the ZP source.

5. Discussion and Conclusions

The closeness of the emission frequency of decimetric zebras to the plasma frequency determines a narrow directivity of the ZP emission. For the exponential density profile across the flaring loop, it gives a small area of this emission and thus high brightness temperatures. We considered two variants of the density dependance on height, *i.e.* two values of the scale height: 1 Mm according to the formula of Priest (2014) and 0.21 Mm for the transition region (Selhorst, Silva-Válio, and Costa, 2008), and two values for the loop width (1 and 2 arcseconds). In all cases, high brightness temperatures were obtained. For the higher value of the density height scale the brightness temperature was estimated as $1.1 \times 10^{15} - 1.3 \times 10^{17}$, and for the lower value as $4.7 \times 10^{13} - 5.6 \times 10^{15}$.

As shown in the Introduction, previous estimations of the ZP brightness temperature were noticeably lower (from 2×10^7 to 10^{13} K). The high brightness temperature found here together with the short duration of zebras and their frequent strong polarization can only be explained as generated by a coherent emission mechanism. Namely, in the non-coherent emission mechanism, the brightness temperature cannot be higher than 10^{12} K, which is given by the Compton limit. The mechanism of the coherent emission of the plasma waves (including the upper-hybrid waves considered here) has been described in detail, *e.g.* by Fleishman and Mel'nikov (1998). Here, we only mention that for the processes described in the present article, an anisotropic distribution of superthermal electrons is necessary. As shown by Yasnov and Karlický (2015), the most probable location of the zebra generation is the transition region in the solar atmosphere of active regions. In the transition region, the temperature as well as the pressure change rapidly, and thus the magnetic fields fan out to form funnels; see, *e.g.*, Wiegelmann, Thalmann, and Solanki (2014). In these magnetic-field funnels, superthermal electrons with momentum perpendicular to the magnetic field are more numerous than those with parallel momentum. The consequence is that in this spatially small region, a high level of anisotropy of the superthermal electrons is easily reached, and thus upper-hybrid waves are generated there (Benáček, Karlický, and Yasnov, 2017).

Note that these brightness temperatures are close to the brightness temperatures of decimetric spikes (Benz, 1986), which indicates that the energies of electrons in the two types of bursts are similar. Because the emission frequency is close to the plasma frequency, the emission absorption can be high, and thus the brightness temperature can be even higher.

Observed sizes of ZP sources can be larger than those assumed here because they are enlarged by the scattering of the emission in density fluctuations in the corona (Bastian, 1994).

We found a lower brightness temperature for a shorter scale height. It has been indicated independently in findings presented by Yasnov and Karlický (2015), Karlický and Yasnov (2015), and Yasnov, Karlický, and Stupishin (2016) that the observational probability of a burst with zebras, which is generated in the transition region with a steep density gradient, is generally greater than the burst generated in a region with smoother changes of the plasma density. This is caused by an enlargement of the visible emission area in the atmosphere with a high density gradient.

Note that ZPs sometimes appear irregularly or quasi-periodically (on timescales of seconds) in the radio spectrum of a Type IV (continuum) burst. This can be explained by small irregular or quasi-periodic motions of the flare loop in the case when the ZP source area is sufficiently small. Then the narrow cone of the emission directivity is oriented toward an observer and the zebra is observed, or *vice versa*.

Numerical simulations with a 3D particle-in-cell model in which hot electrons are described by the DGH distribution function show that first the energy density of the upper-hybrid waves exponentially grows with a linear growth rate and then is saturated. We found that the saturation energy of the upper-hybrid waves is proportional to the ratio n_h/n_e . This dependence enabled us to calculate the saturation energy of the upper-hybrid waves for much lower ratios of n_h/n_e . The saturation energy of the upper-hybrid waves also depends on the gyroharmonic number s . For $s = 7-18$ we found that the computed saturated energies can be well fit by an exponential function. This fit enabled us to find the saturated energy of the upper-hybrid waves for the analyzed 2 May 1998 zebra with $s = 21$ of about $W_{UH} = 1.6 \times 10^{-3} E_{h,kin}$.

Upper-hybrid waves are generated when the growth rate exceeds the damping of these waves by collisions. For the zebra observed during the 2 May 1998 event, this condition is fulfilled if the ratio of hot and cold electrons [n_h/n_e] is greater than 4.93×10^{-4} . Using this value, we computed the minimum energy density of the upper-hybrid waves in the ZP source ($W_{UH,min} = 4.40 \times 10^{-5} \text{ J m}^{-3}$) and the transformation efficiency of the upper-hybrid waves into electromagnetic waves ($\epsilon = 2.54 \times 10^{-6} - 8.86 \times 10^{-4}$).

The transformation efficiency strongly depends on the plasma parameters in the radio source, such as plasma turbulence, levels of low-frequency plasma waves (*e.g.* the ion-sound waves), and density gradients, see Melrose (1985). Unfortunately, most of these parameters in ZP sources are not known, and moreover, the theory of wave conversions is not fully established, especially in the nonlinear regime. For example, Melrose (1985) presented this efficiency in the very broad range from 10^{-10} for the scattering on the thermal ions to 10^{-4} for small-scale density inhomogeneities ($10-10^2 \text{ km}$). Based on comparing the transformation efficiency found in the present article with the efficiency shown by Melrose (1985), we conclude that the zebra source probably has small-scale density inhomogeneities.

Acknowledgements The authors thank the referee for constructive comments that improved the article. M. Karlický acknowledges support from Grants 16-13277S and 17-16447S of the Grant Agency of the Czech Republic. L.V. Yasnov acknowledge support from Grant 16-02-00254 of the Russian Foundation for Basic Research. Computational resources were provided by the CESNET LM2015042 and the CERIT Scientific Cloud LM2015085, provided under the program “Projects of Large Research, Development, and Innovations Infrastructures”.

Disclosure of Potential Conflicts of Interest Authors have no potential conflicts of interest.

References

- Altynsev, A.T., Kuznetsov, A.A., Meshalkina, N.S., Rudenko, G.V., Yan, Y.: 2005, On the origin of microwave zebra pattern. *Astron. Astrophys.* **431**, 1037. DOI.

- Bárta, M., Karlický, M.: 2006, Interference patterns in solar radio spectra: high-resolution structural analysis of the corona. *Astron. Astrophys.* **450**, 359. [DOI](#).
- Bastian, T.S.: 1994, Angular scattering of solar radio emission by coronal turbulence. *Astrophys. J.* **426**, 774. [DOI](#).
- Benáček, J., Karlický, M., Yasnov, L.: 2017, Temperature dependent growth rates of the upper-hybrid waves and solar radio zebra patterns. *Astron. Astrophys.* **555**, A1. [DOI](#).
- Benz, A.O.: 1986, Millisecond radio spikes. *Solar Phys.* **104**, 99. [DOI](#).
- Buneman, O., Storey, L.R.O.: 1985, Simulations of fusion plasmas by A 3-D, E-M particle code. Technical report, Stanford Univ. Report, Stanford.
- Chen, B., Bastian, T.S., Gary, D.E., Jing, J.: 2011, Spatially and spectrally resolved observations of a zebra pattern in a solar decimetric radio burst. *Astrophys. J.* **736**, 64. [DOI](#).
- Chernov, G.P.: 2006, Solar radio bursts with drifting stripes in emission and absorption. *Space Sci. Rev.* **127**, 195. [DOI](#).
- Chernov, G.P., Yan, Y.H., Fu, Q.J.: 2003, A superfine structure in solar microwave bursts. *Astron. Astrophys.* **406**, 1071. [DOI](#).
- Chernov, G.P., Klein, K.L., Zlobec, P., Aurass, H.: 1994, Fine structure in a metric type 4 burst: multi-site spectrographic, polarimetric, and heliographic observations. *Solar Phys.* **155**, 373. [DOI](#).
- Dory, R.A., Guest, G.E., Harris, E.G.: 1965, Unstable electrostatic plasma waves propagating perpendicular to a magnetic field. *Phys. Rev. Lett.* **14**, 131. [DOI](#).
- Fleishman, G.D., Mel'nikov, V.F.: 1998, Reviews of topical problems: millisecond solar radio spikes. *Phys. Usp.* **41**, 1157. [DOI](#).
- Jiricka, K., Karlický, M., Kepka, O., Tlamicha, A.: 1993, Fast drift burst observations with the new Ondrejov radiospectrograph. *Solar Phys.* **147**, 203. [DOI](#).
- Karlický, M.: 2013, Radio continua modulated by waves: zebra patterns in solar and pulsar radio spectra? *Astron. Astrophys.* **552**, A90. [DOI](#).
- Karlický, M., Bárta, M.: 2008, Fragmentation of the current sheet, anomalous resistivity, and acceleration of particles. *Solar Phys.* **247**, 335. [DOI](#).
- Karlický, M., Yasnov, L.V.: 2015, Determination of plasma parameters in solar zebra radio sources. *Astron. Astrophys.* **581**, A115. [DOI](#).
- Kuznetsov, A.A., Kontar, E.P.: 2015, Spatially resolved energetic electron properties for the 21 May 2004 flare from radio observations and 3D simulations. *Solar Phys.* **290**, 79. [DOI](#).
- Kuznetsov, A.A., Tsap, Y.T.: 2007, Loss-cone instability and formation of zebra patterns in type IV solar radio bursts. *Solar Phys.* **241**, 127. [DOI](#).
- LaBelle, J., Treumann, R.A., Yoon, P.H., Karlický, M.: 2003, A model of zebra emission in solar type IV radio bursts. *Astrophys. J.* **593**, 1195. [DOI](#).
- Matsumoto, H., Omura, Y.: 1993, *Computer Space Plasma Physics: Simulation Techniques and Software*, Terra Scientific, Tokyo, 305.
- Melrose, D.B.: 1985. In: McLean, D.J., Labrum, N.R. (eds.) *Plasma Emission Mechanisms*. Cambridge University Press, Cambridge, 177.
- Peter, H., Bingert, S.: 2012, Constant cross section of loops in the solar corona. *Astron. Astrophys.* **548**, A1. [DOI](#).
- Peter, H., Bingert, S., Klimchuk, J.A., de Forest, C., Cirtain, J.W., Golub, L., Winebarger, A.R., Kobayashi, K., Korreck, K.E.: 2013, Structure of solar coronal loops: from miniature to large-scale. *Astron. Astrophys.* **556**, A104. [DOI](#).
- Priest, E.: 2014, *Magnetohydrodynamics of the Sun*, Cambridge University Press, Cambridge.
- Selhorst, C.L., Silva-Válio, A., Costa, J.E.R.: 2008, Solar atmospheric model over a highly polarized 17 GHz active region. *Astron. Astrophys.* **488**, 1079. [DOI](#).
- Tan, B.: 2010, A physical explanation of solar microwave zebra pattern with the current-carrying plasma loop model. *Astrophys. Space Sci.* **325**, 251. [DOI](#).
- Tan, B., Tan, C., Zhang, Y., Huang, J., Mészáros, H., Karlický, M., Yan, Y.: 2014, A very small and super strong zebra pattern burst at the beginning of a solar flare. *Astrophys. J.* **790**, 151. [DOI](#).
- Thejappa, G.: 1991, A self-consistent model for the storm radio emission from the Sun. *Solar Phys.* **132**, 173. [DOI](#).
- Watko, J.A., Klimchuk, J.A.: 2000, Width variations along coronal loops observed by TRACE. *Solar Phys.* **193**, 77. [DOI](#).
- Wiegmann, T., Thalmann, J.K., Solanki S.K.: 2014, The magnetic field in the solar atmosphere. *Astron. Astrophys. Rev.* **22**, 78. [DOI](#).
- Yasnov, L.V., Karlický, M.: 2015, Regions of generation and optical thicknesses of dm-zebra lines. *Solar Phys.* **290**, 2001. [DOI](#).
- Yasnov, L.V., Karlický, M., Stupishin, A.G.: 2016, Physical conditions in the source region of a zebra structure. *Solar Phys.* **291**, 2037. [DOI](#).

- Zaitsev, V.V., Stepanov, A.V.: 1983, The plasma radiation of flare kernels. *Solar Phys.* **88**, 297. [DOI](#).
- Zheleznyakov, V.V.: 1997, *Radiation in Astrophysical Plasmas*, in russian. Original russian title — “Izlucheniye v astrofizicheskoy plasme”, Yanus K., Moscow.
- Zheleznyakov, V.V., Zlotnik, E.Y.: 1975, Cyclotron wave instability in the corona and origin of solar radio emission with fine structure. III. Origin of zebra-pattern. *Solar Phys.* **44**, 461. [DOI](#).
- Zlotnik, E.Y.: 2013, Instability of electrons trapped by the coronal magnetic field and its evidence in the fine structure (zebra pattern) of solar radio spectra. *Solar Phys.* **284**, 579. [DOI](#).

Appendix C

Double plasma resonance instability as a source of solar zebra emission

J. Benáček¹ and M. Karlický²

¹ Department of Theoretical Physics and Astrophysics, Masaryk University, Kotlářská 2, 611 37 Brno, Czech Republic
 e-mail: jbenacek@physics.muni.cz

² Astronomical Institute of the Czech Academy of Sciences, Fričova 258, 251 65 Ondřejov, Czech Republic

Received 23 June 2017 / Accepted 1 November 2017

ABSTRACT

Context. The double plasma resonance (DPR) instability plays a basic role in the generation of solar radio zebras. In the plasma, consisting of the loss-cone type distribution of hot electrons and much denser and colder background plasma, this instability generates the upper-hybrid waves, which are then transformed into the electromagnetic waves and observed as radio zebras.

Aims. In the present paper we numerically study the double plasma resonance instability from the point of view of the zebra interpretation.

Methods. We use a 3-dimensional electromagnetic particle-in-cell (3D PIC) relativistic model. We use this model in two versions: (a) a spatially extended “multi-mode” model and (b) a spatially limited “specific-mode” model. While the multi-mode model is used for detailed computations and verifications of the results obtained by the “specific-mode” model, the specific-mode model is used for computations in a broad range of model parameters, which considerably save computational time. For an analysis of the computational results, we developed software tools in Python.

Results. First using the multi-mode model, we study details of the double plasma resonance instability. We show how the distribution function of hot electrons changes during this instability. Then we show that there is a very good agreement between results obtained by the multi-mode and specific-mode models, which is caused by a dominance of the wave with the maximal growth rate. Therefore, for computations in a broad range of model parameters, we use the specific-mode model. We compute the maximal growth rates of the double plasma resonance instability with a dependence on the ratio between the upper-hybrid ω_{UH} and electron-cyclotron ω_{ce} frequency. We vary temperatures of both the hot and background plasma components and study their effects on the resulting growth rates. The results are compared with the analytical ones. We find a very good agreement between numerical and analytical growth rates. We also compute saturation energies of the upper-hybrid waves in a very broad range of parameters. We find that the saturation energies of the upper-hybrid waves show maxima and minima at almost the same values of ω_{UH}/ω_{ce} as the growth rates, but with a higher contrast between them than the growth rate maxima and minima. The contrast between saturation energy maxima and minima increases when the temperature of hot electrons increases. Furthermore, we find that the saturation energy of the upper-hybrid waves is proportional to the density of hot electrons. The maximum saturated energy can be up to one percent of the kinetic energy of hot electrons. Finally we find that the saturation energy maxima in the interval of $\omega_{UH}/\omega_{ce} = 3\text{--}18$ decrease according to the exponential function. All these findings can be used in the interpretation of solar radio zebras.

Key words. instabilities – methods: numerical – Sun: radio radiation

1. Introduction

The loss-cone type of distribution of hot electrons superimposed on the distribution of much denser and colder background plasma is unstable due to the double plasma resonance instability (Zheleznyakov & Zlotnik 1975; Melrose & Dulk 1982; Zaitsev & Stepanov 1983; Winglee & Dulk 1986; Ledenev et al. 2001; Zlotnik 2013; Karlický & Yasnov 2015). This instability generates the upper-hybrid waves, which have their maxima close to the gyro-harmonic number $s = \omega_{UH}/\omega_{ce}$, where $\omega_{UH}^2 = \omega_{pe}^2 + \omega_{ce}^2$ and ω_{UH} , ω_{pe} , and ω_{ce} are the upper-hybrid, electron-plasma, and electron-cyclotron frequency, respectively. Owing to this property, the double plasma resonance (DPR) instability is used in models of solar radio zebras (Zheleznyakov & Zlotnik 1975; Winglee & Dulk 1986; Ledenev et al. 2001; Treumann et al. 2011; Zlotnik 2013; Karlický & Yasnov 2015; Yasnov & Karlický 2015; Benáček et al. 2017).

The resonance condition for the double plasma resonance instability in the relativistic case can be expressed as

$$\omega_{UH} - \frac{k_{\parallel} u_{\parallel}}{\gamma} - \frac{s \omega_{ce}}{\gamma} = 0, \quad (1)$$

where $\mathbf{k} = (k_{\parallel}, k_{\perp})$ is wave vector, $\mathbf{u} = (u_{\perp}, u_{\parallel})$, $u_{\perp} = p_{\perp}/m_e$, and $u_{\parallel} = p_{\parallel}/m_e$ are the hot electron velocities perpendicular and parallel to the magnetic field; m_e is the electron mass, $\gamma = \sqrt{1 + u^2/c^2}$ is the relativistic Lorentz factor, s is the gyro-harmonic number, and c is the speed of light. In theoretical models studying the double plasma resonance instability, the distribution of hot electrons is usually taken as the Dory–Guest–Harris (DGH; Dory et al. 1965) distribution for $j = 1$ in the form

$$f = \frac{u_{\perp}^2}{2(2\pi)^{3/2} v_t^5} \exp\left(-\frac{u_{\perp}^2 + u_{\parallel}^2}{2v_t^2}\right), \quad (2)$$

where v_t we call the thermal velocity of hot electrons, although the distribution function in the relation (2) is not Maxwellian. The distribution of the background plasma is taken as a Maxwellian one. The combination of both these distributions is considered to be the prototype distribution generating radio zebras (Winglee & Dulk 1986).

In our previous paper (Benáček et al. 2017) we studied the double plasma resonance instability analytically. We showed that the maxima of growth rates of the upper-hybrid waves are shifted to lower ratios of ω_{UH}/ω_{ce} and the contrast between maxima and minima of the growth rate decreases as the temperature of hot electrons increases. On the other hand, when the temperature of the background plasma is increased, the contrast remains the same.

In studies of solar radio zebras (e.g. Ledenev et al. 2001), the frequencies of the zebra stripes and the contrast of these stripes to the background continuum are analyzed. The frequencies are used for the determination of the magnetic field in zebra radio sources. Therefore, it is important to know the relation between the zebra stripe frequencies and the gyro-harmonic number $s \approx \omega_{UH}/\omega_{ce}$. Furthermore, the contrast of the zebra stripes is believed to be connected with the temperature of hot electrons (Yasnov & Karlický 2004). Moreover, some zebras have many stripes and their frequencies correspond to high gyro-harmonic numbers (sometimes >20 ; Karlický & Yasnov 2015). All these facts require computations in a very broad range of the gyro-harmonic number s , which are difficult to make with the spatially extended multi-mode model. Fortunately, we found that the maximal growth rates and saturation energies computed in the multi-mode model agree very well with that computed in the spatially limited specific-mode model. This agreement is caused by the fact that the wave with the maximal growth rate becomes very soon dominant over other growing waves (due to its exponential growth). Using this specific-mode model, which considerably saves computational time, we compute the maximal growth rates and saturation energies of the DPR instability in a broad range of parameters. Because in the analytical analysis of growth rates of the DPR instability several assumptions were made, these numerical computations serve to verify the analytical results.

The paper is structured as follows. In Sect. 2, we describe our numerical model and initial conditions for the studied double plasma resonance instability. In Sect. 3, we present the results for different model parameters. Discussion of these results and conclusions are in Sect. 4.

2. Model

We use a 3D particle-in-cell (PIC) relativistic model (Buneman & Storey 1985; Matsumoto & Omura 1993; Karlický & Bárta 2008) with multi-core message passing interface (MPI) parallelization. Further details can be found in Matsumoto & Omura (1993, p. 67–84) and on the link below¹. In the present article we use this model in two versions: (a) the spatially extended model with many wave modes (multi-mode model), and (b) spatially limited model with specific wave mode (specific-mode model), which is used for relatively fast computing in the broad range of model parameters. The model size in x -, y -, and z -directions is $128 \times 60\Delta \times 128\Delta$ for the multi-mode model, and $\lambda\Delta \times \lambda\Delta \times 32\Delta$ for the specific-mode model, respectively, where $\Delta = 1$ is the grid size and λ is the wavelength of the specific upper-hybrid

wave. For chosen gyro-harmonic numbers and plasma temperatures, we fit the size of the specific-mode model to find the wave mode with the maximal growth rate. In all models we use periodic boundary conditions in all three directions.

The model time step is $dt = 1$, electron plasma frequency $\omega_{pe} = 0.05$, initial magnetic field is in the z -direction, and electron cyclotron frequency ω_{ce} varies from $0.38 \omega_{pe}$ to $0.056 \omega_{pe}$ approximating the gyro-harmonic numbers $s = 3$ –18. For dependencies of the growth rate on temperatures, we use s in the range of $s = 3$ –7. Higher values of s up to 18 are used for calculating the saturation energies of the generated upper-hybrid waves, which is needed for zebras with many zebra stripes. In the model we use two groups of electrons: cold background Maxwellian electrons with the thermal velocity $v_{tb} = 0.03$ – 0.05 c, corresponding to the temperature in the interval 5.4–14.8 MK, and hot electrons with the DGH distribution having the velocity $v_t = 0.15$ – 0.3 c. Higher values of the background plasma temperatures are given by the requirements of the PIC model. However, as known from the previous analytical study (Benáček et al. 2017) and shown in the following, variations of the background plasma temperature have little effect.

The electron density of background electrons was taken as $n_e = 960$ per cell and the ratio of background to hot electrons was taken as $n_e/n_h = 8$ with some exceptions mentioned in the following. The number of protons is the same as the number of electrons and their temperature is always the same as that of background electrons. The proton-to-electron mass ratio m_p/m_e is 1836.

To find the maximal growth rate for specific physical parameters, we changed the model size $\lambda\Delta$ in the perpendicular direction to the magnetic field. Namely, we fit the wavelength of the upper-hybrid wave with the maximal growth rate to a distance of grids used in the PIC model. Thus, we get the maximal simulated growth rate. We found that the optimal model size does not change when computing with different ratios of the electron plasma and electron cyclotron frequencies, but is changed by changing the temperature.

At the beginning of DPR instability, the electric wave energy grows exponentially. We fit this part of the electric energy evolution by the function $W_{UH} = A_0 \exp(2\Gamma t)$, where A_0 is the initial electric energy, t is time, and Γ is the growth rate in model units. Finally we expressed the growth rate of the upper-hybrid waves in the ratio to the upper-hybrid frequency.

3. Results

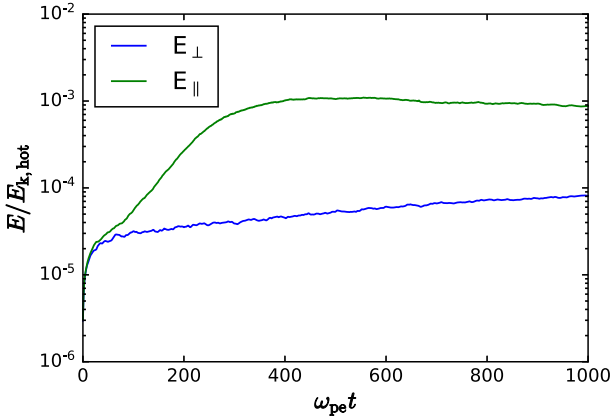
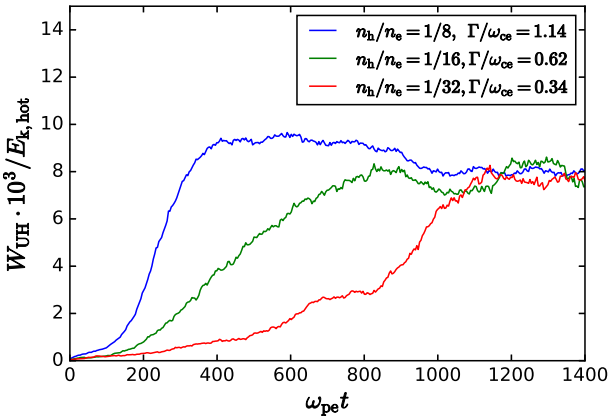
Firstly we compute an evolution of the DPR instability and generation of the upper-hybrid waves in the multi-mode models with the parameters summarized in Table 1. We show an example of the time evolution of the electric energy density in the parallel and perpendicular directions to the magnetic field lines in Model 2M normalized to the kinetic energy density of hot electrons for the maximal growth rate and the gyro-harmonic number $s = 6$ in Fig. 1. As can be seen here, the electric energy density in the perpendicular direction dominates over the parallel energy density by at least two orders of magnitude, which indicates the generation of the upper-hybrid waves.

Examples of the time evolution of the energy density of the upper-hybrid waves normalized to the kinetic energy density of hot electrons for three values of n_h/n_e , the gyro-harmonic number $s = 6$, the maximal growth rate, and Model 2M are presented in Fig. 2. The growth rates, estimated in the early stages of the evolution, are written in this figure. As seen here, these

¹ <https://www.terrapub.co.jp/e-library/cspp/text/10.txt>

Table 1. Parameters of the multi-mode models.

Comp. no.	v_t	v_{tb}	s
1M	0.15 c	0.03 c	6
2M	0.2 c	0.03 c	6
3M	0.2 c	0.03 c	3
4M	0.3 c	0.03 c	5

**Fig. 1.** Time evolution of the electric energy density in the parallel and perpendicular directions to the magnetic field lines in Model 2M (Table 1), normalized to the kinetic energy density of hot electrons for the maximal growth rate and the gyro-harmonic number $s = 6$.**Fig. 2.** Time evolution of the energy density of the upper-hybrid waves normalized to the kinetic energy density of hot electrons for three values of n_h/n_e and for the maximal growth rate and $s = 6$. Other parameters are the same as in Model 2M.

growth rates are proportional to the density of hot electrons, in agreement with the paper by [Yasnov & Karlický \(2004\)](#). Furthermore, the normalized energy density of the upper-hybrid waves in all three models converges to the same saturation energy, which indicates that the saturation energy of the upper-hybrid waves is also proportional to the density of hot electrons. The kinetic energy density of hot electrons $E_{k,hot}$ depends on the plasma density of hot electrons.

3.1. DPR instability in detail

To see the processes during the DPR instability in detail, we make a comparison of the distributions in the initial state and at $\omega_{pe}t = 1000$ for Models 2M and 4M (Table 1; see Fig. 3).

Comparing changes of the distribution in these models (left and right columns in Fig. 3), we can see that the instability with different model parameters causes different changes of the distribution function. The distribution function does not change only in one point of the phase space, but in the subspace defined by resonance ellipses corresponding to the range of k_{\parallel} . In Fig. 3, in the third row, we show these resonance ellipses in the phase space, where the changes are dominant. We also show how the resonance ellipses shift across the distribution function in dependence on k_{\parallel} (see the arrows). In both models, the loss-cones of the distributions are step by step fulfilled by electrons (see the red regions in the third row of Fig. 3) and thus the distributions become closer to the Maxwellian distribution. These changes are due to an increasing energy level of the upper-hybrid waves.

We analyzed time evolution of energies in waves with the k-wave vectors perpendicular to the magnetic field in Model 2M (Fig. 4). As seen in this figure, the interval of k-vectors is relatively narrow and remains practically the same during the instability evolution. It shows that the energy of the upper-hybrid waves is concentrated in the relatively narrow interval of k-vectors. As will be shown in the following, it enables us to use the specific-mode models.

3.2. Comparison of specific-mode and multi-mode model saturation

Because our main objective is to determine the growth rates and saturation energies in a broad range of parameters (which is important for the interpretation of observed zebras), we search for ways to accelerate computations. We decided to use the specific-mode models that are much faster than the multi-mode ones. To justify their use, we compare the growth rate and saturation energies for all multi-mode models shown in Table 1 with the specific-mode models with the same physical parameters. An example of this comparison for Model 2M is shown in Fig. 5. While in the multi-mode model we use the model size $128\Delta \times 60\Delta \times 128\Delta$, in the specific-mode model in this case we use the model size $12\Delta \times 12\Delta \times 32\Delta$. This specific-mode model covers interval of $k_{\perp}c/\omega_{pe}$ above 5.23 (see Fig. 4). This means that this specific-mode model covers the k-vector waves that are important for the DPR instability. This explains why the results from the multi-mode and specific-mode models are very similar (see the following).

As seen in Fig. 5, the growth rate and saturation energy in both the models agree very well. The same result is found for all other models according to Table 1. This agreement is caused by a dominance of the wave with the maximal growth rate (exponential increase) during an evolution of the double plasma resonance instability. We utilize this agreement in the following computations of the growth rates and saturation energies in a broad range of the model parameters. The agreement between numerically and analytically computed growth rates, shown in the following, also justifies the use of the specific-mode models in our case.

3.3. Effects of temperatures of hot and background plasma electrons on the growth rate

In the following computations with the specific-mode models, we use the model parameters as shown in Table 2. Figure 6 presents the effects of the temperature of hot and background electrons on the growth rate. Every point in this figure is computed for at least three model sizes of the specific-mode models. Error bars are estimated from their fit and the probability that the same initial parameters give the same result. Models with

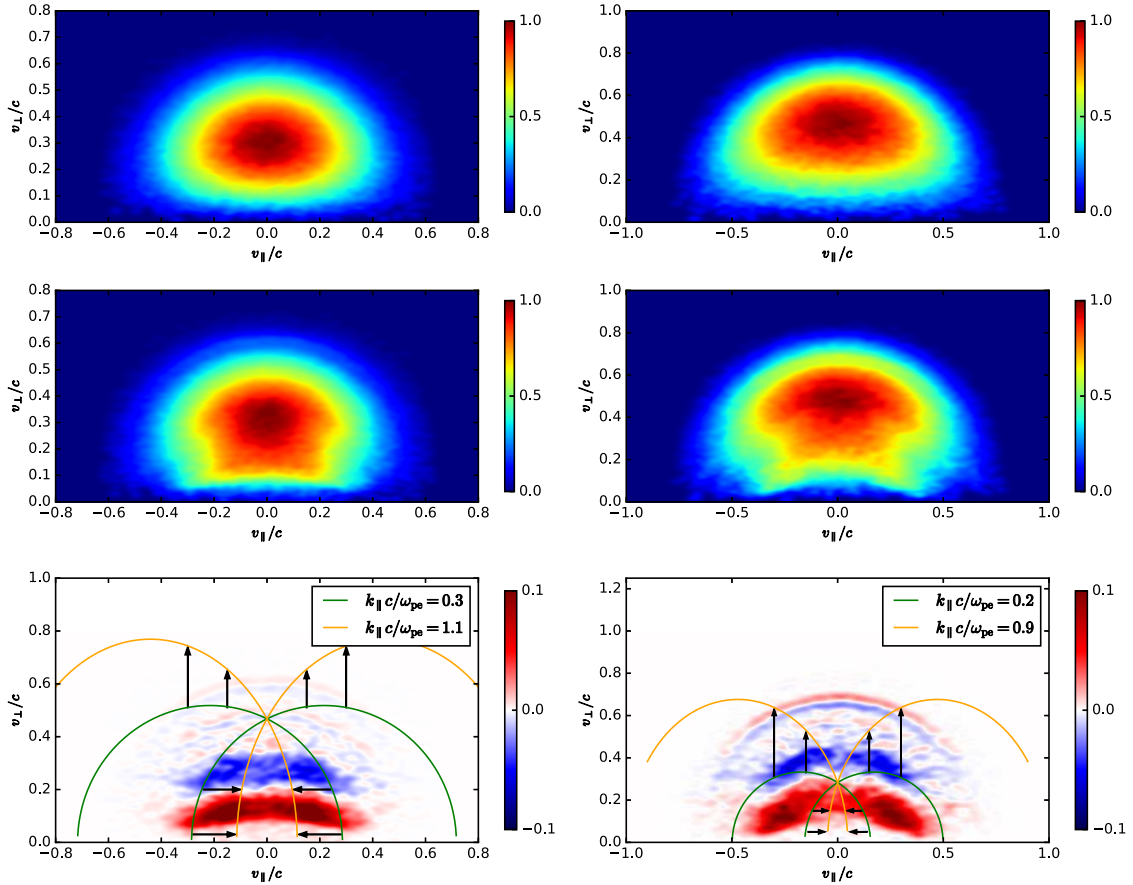


Fig. 3. Changes of the electron distribution functions of hot electrons during the DPR instability. *Left column:* Model 2M with $s = 6$. *Right column:* Model 4M with resonance $s = 5$. *First row:* the distribution at the initial state. *Second row:* the distribution at $\omega_{pe} t = 1000$. Distributions are normalized to their maximal value. *Third row:* the difference of the distributions between the initial state and at $\omega_{pe} t = 1000$. Red regions are with enhanced densities and blue ones are with reduced densities. Elliptical lines show the resonance ellipses for a given k -wave vector along magnetic field. Black arrows show that the ellipses shift with increasing value of k_{\parallel} .

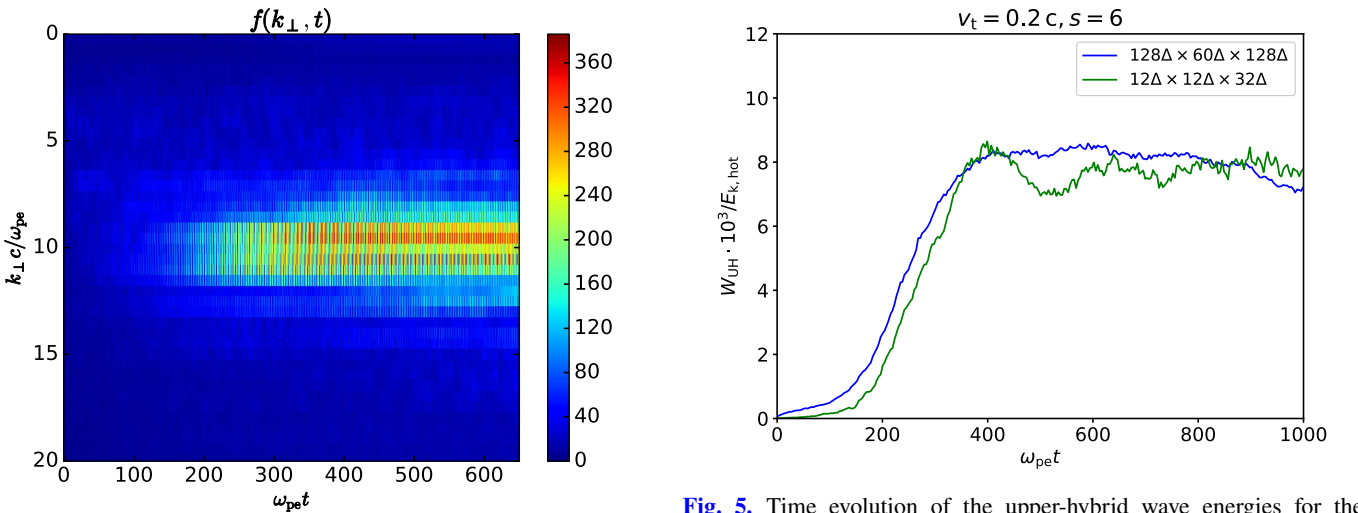


Fig. 4. Time evolution of energies in waves with the k -wave vectors in perpendicular direction to the magnetic field lines in Model 2M.

higher temperatures have lower errors because generated waves are more dominant over the background noise.

Growth rates have the maxima that are shifted to frequencies lower than those given by the gyro-harmonic number s (Fig. 6, upper part and Fig. 7) and this shift increases with increasing temperature. The ratio between maximal and minimal growth

rates for each temperature is up to one order and increases with the decreasing temperature of hot electrons. These effects are in agreement with the analytical results (Benáček et al. 2017). However, contrary to the analytical results, the growth rate for $v_t = 0.3$ is higher than that for lower temperatures. We think that this difference is caused by differences in the analytical and

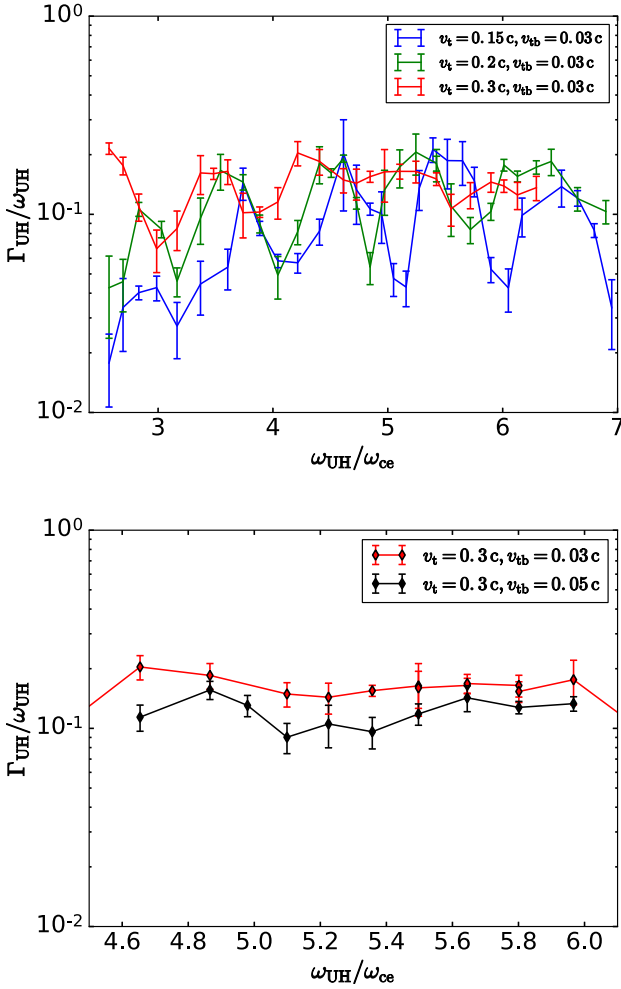


Fig. 6. Growth rates in dependence on ω_{UH}/ω_{ce} for Models 1S–4S. *Top:* plots for three different temperatures of hot electrons v_t . *Bottom:* plots for two different temperatures of background plasma electrons v_{tb} .

Table 2. Parameters of the specific-mode models.

Model no.	v_t	v_{tb}
1S	0.15 c	0.03 c
2S	0.2 c	0.03 c
3S	0.3 c	0.03 c
4S	0.3 c	0.05 c

numerical approach. While in the analytical approach we calculate the growth rate only for one specific k -vector wave, in numerical computations k -vectors in some interval are always in operation. The effect of the temperature of background plasma electrons is small (Fig. 6, bottom part), which agrees with the analytical theory (Benáček et al. 2017). We also determined the shifts of maxima of growth rate (Fig. 7). They increase with increasing s and also depends on temperature of hot electrons.

3.4. Effect of the hot-cold plasma density ratio on the frequency of the growth rate maximum

As shown in Fig. 8, the frequency of the growth rate maximum also depends on the ratio of the background and hot electron densities n_e/n_h . This dependence is exponential as shown by its fit and converges to $\omega_{UH}/\omega_{ce} = 5.1$ for high values of the n_e/n_h

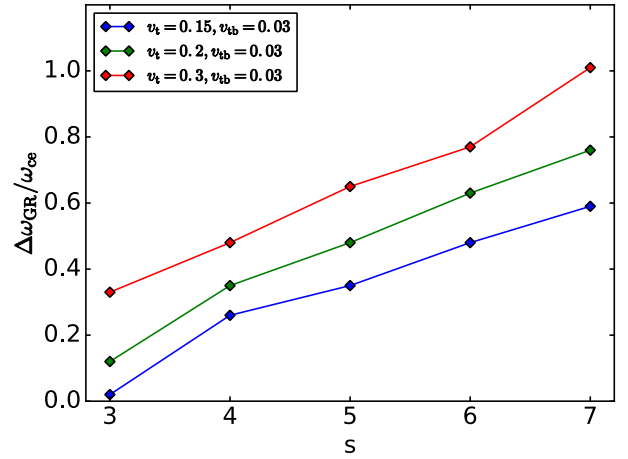


Fig. 7. Shifts of frequency of growth rate maxima from frequency given by gyro-harmonic number s .

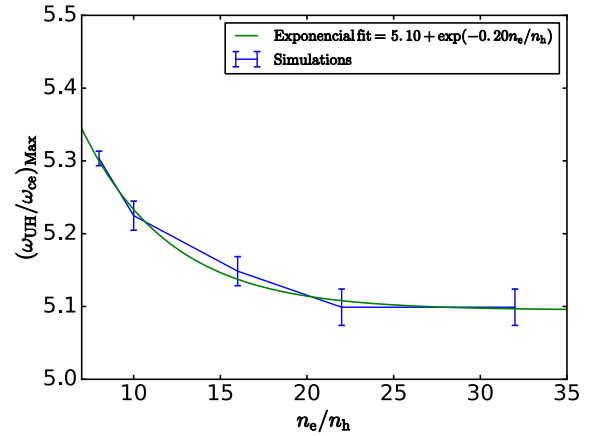


Fig. 8. Frequency of growth rate maximum $(\omega_{UH}/\omega_{ce})_{\text{Max}}$ as function of ratio of background and hot electron densities n_e/n_h for parameters in Model 2S and $s = 6$.

ratio. Namely, low values of the n_e/n_h ratio shift the resonance of the DPR instability and thus the frequency of the growth rate maximum. In the analytical analysis it is supposed that the density of cold electrons is much greater than that of hot electrons ($n_e \gg n_h$).

In most of our simulations the density ratio n_h/n_e is 1:8 in order to keep a low numerical noise. However, such dependencies enable us to extrapolate our results to much lower density ratios, for example to 1:100 as usually considered in the zebra interpretation (see the following).

3.5. Comparison of the numerical and analytical growth rates

We compared the simulated growth rates with the analytical ones presented in the paper by Benáček et al. (2017). The comparison is shown in Fig. 9. It was made as follows. We chose the upper-hybrid frequency and hot electron density as $\omega_{UH} = 7 \times 10^9 \text{ s}^{-1}$ ($f_{UH} = 1.11 \text{ GHz}$) and $n_h = 10^8 \text{ cm}^{-3}$. We changed the growth rate plot expressed in dependence on ω_{ce} (Benáček et al. 2017) to that in dependence on ω_{UH} . Then, we transformed the simulated growth rates, computed for $n_e/n_h = 8$, to those with $n_e/n_h = 100$. The transformation was made in two steps. We shifted the simulated growth rate maxima toward lower values of ω_{UH}/ω_{ce} according to the relation expressed in Fig. 6. Finally, the growth rates were multiplied by the factor 8/100 using

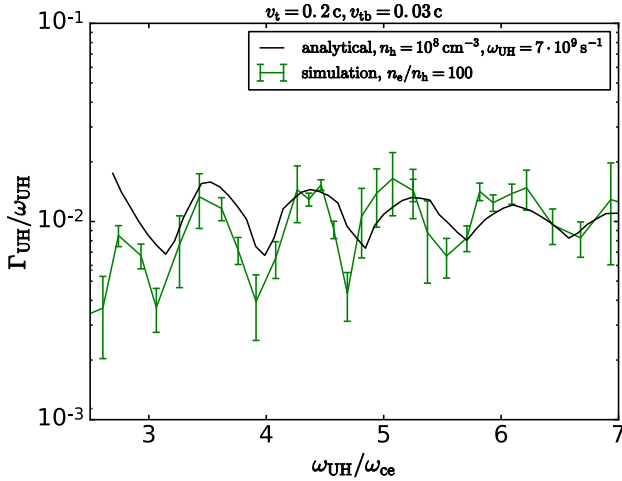


Fig. 9. Comparison of the simulated and analytically derived growth rates for $v_t = 0.2 c$ and $v_{tb} = 0.03 c$.

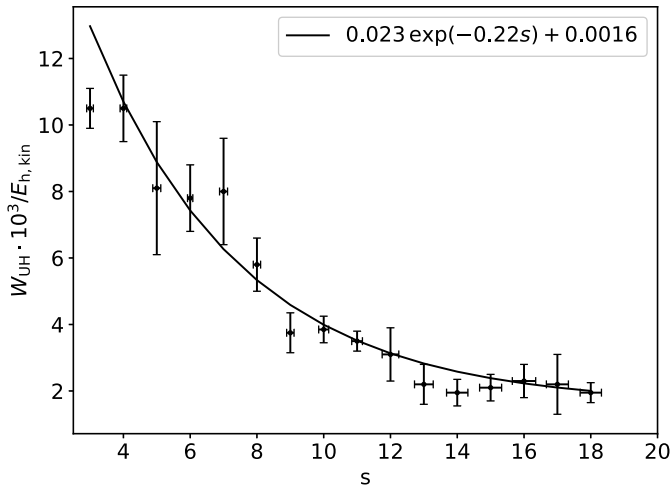


Fig. 10. Maximal saturation energies of the upper-hybrid waves in dependence on the gyro-harmonic number s for Model 2S with the exponential fit.

the linear relation between the growth rate and density of hot electrons (Yasnov & Karlický 2004). As shown in Fig. 9, there is good agreement between the numerically and analytically computed growth rates.

3.6. Saturation energy levels of the upper-hybrid waves in a broad range of gyro-harmonic numbers

In all models, we determined the saturation energy of the upper-hybrid waves. The saturation energy is reached when the growth rate is balanced by nonlinear effects. The time when the saturation begins depends on the model parameters. In our cases, the saturation time was in the time interval $\omega_{pe} t_{\text{satur}} = 300\text{--}1200$. Mostly, the maximal growth rate leads to maximal saturation energy, but this is not a rule. In some cases, the saturated energy is higher in the model with lower growth rate. In other cases, the saturation energies have recognizable maxima, while the growth rate is nearly constant in the broad range of ratios of ω_{UH}/ω_{ce} .

We computed one set of models changing the gyro-harmonic number s from $s = 3$ up to $s = 18$ and keeping the same temperatures as in Model 2S. As shown in Fig. 10, the saturation energy level in local maxima decreases with increasing s and

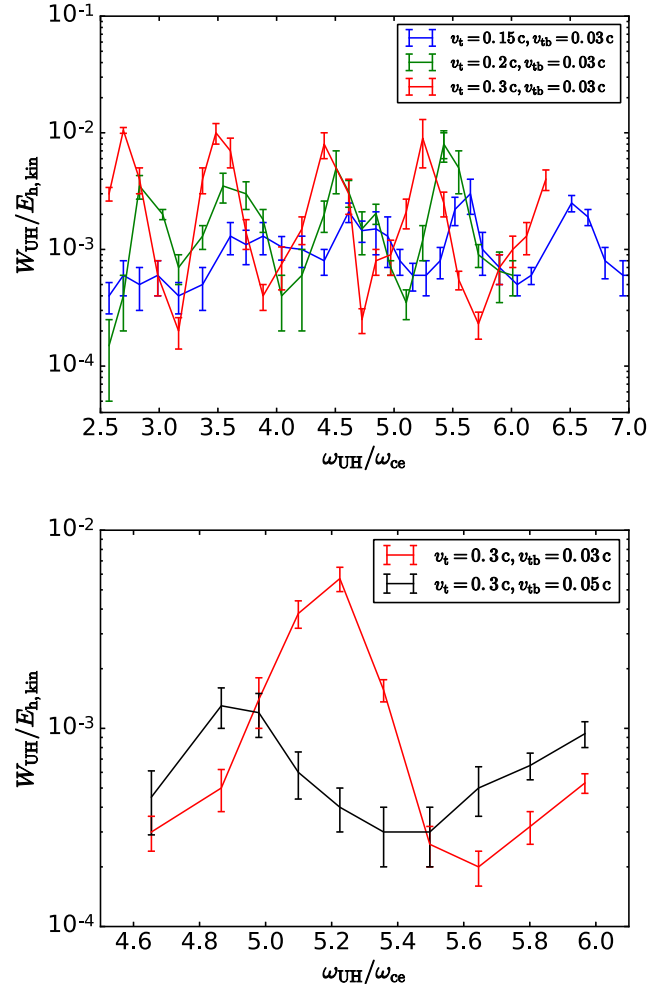


Fig. 11. Saturation energies as a function of ω_{UH}/ω_{ce} . *Top:* plots for three different temperatures of hot electrons v_t . Saturation maxima are shifted to lower ratios ω_{UH}/ω_{ce} . *Bottom:* plots for two different temperatures of background plasma electrons v_{tb} .

converges to the value $W_{UH} \approx 1.6 \times 10^{-3} E_{h,kin}$ (see the exponential fit as presented in Fig. 10). This exponential function can be used for an extrapolation of the saturation energies for even higher parameter s , which is useful for zebras with many stripes.

Maximal values of the saturated energy levels of the upper-hybrid waves for low values of s are about one percent of the kinetic energy of hot electrons. The saturated energy levels increase with an increase in the kinetic energy (temperature) of hot electrons.

Similarly to the growth rates, the saturation energies (Fig. 11) have the maxima and minima shifted to lower ratios of ω_{UH}/ω_{ce} than those given by the integer values of the gyro-harmonic number s . Figure 12 shows these shifts. The frequency of the growth rate and saturation energy maximum is not generally the same. The saturation energy maxima are usually less shifted to lower frequencies than the growth rate maxima. However, contrary to the growth rates, the contrast between the maxima and minima increases with the increasing temperature of hot electrons (Fig. 11, upper part). Similarly, in the models that vary the temperature of background plasma electrons, the contrast between the saturation energy maxima and minima is higher than that for the growth rates (Fig. 11, bottom part).

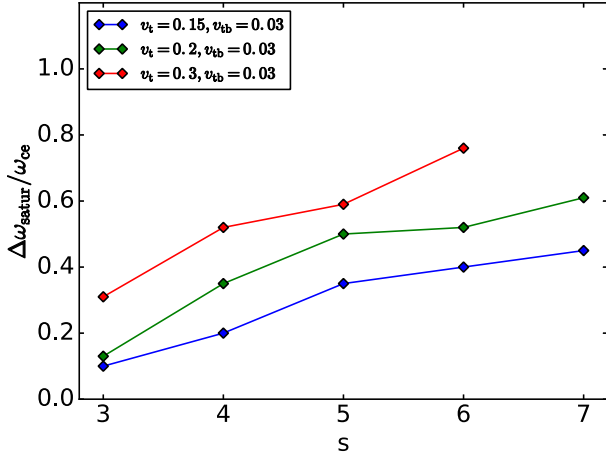


Fig. 12. Shifts of the frequency of the saturated energy maxima from the frequency given by the gyro-harmonic number s .

4. Discussion and conclusions

Using the 3D PIC model in two versions (multi-mode and specific-mode models) we computed not only the growth rates of the double plasma resonance instability, but also saturation energies of the generated upper-hybrid waves. We described details of the DPR instability by showing how the distribution function of hot electrons changes during the DPR instability. We found that the growth rate as well as the saturation energy are proportional to the density of hot electrons.

Owing to many assumptions made in our previous analytical study, we checked the analytical results using the present numerical models. We found a very good agreement between the numerical and analytical results. This justifies a use of the specific-mode models in this case. We confirmed that the growth rate maxima are shifted to lower frequencies in comparison with those given by the gyro-harmonic number s . This frequency shift increases with an increase of the temperature of hot electrons, in agreement with the analytical results. We confirmed that the contrast between maxima and minima of the growth rate decreases with the increasing of the hot electron temperature. On the other hand, the temperature of the background plasma has only a small effect on the growth rates.

We found that the frequency of the growth rate maximum depends on the ratio of the background and hot electron densities n_e/n_h . We used this dependence to extrapolate our numerical results, made mostly for the ratio $n_e/n_h = 8$, to those with the ratio $n_e/n_h = 100$ considered usually in the analytical studies of zebras. Using this dependence in detailed comparison of the analytical and numerical growth rates, made in the interval of

$\omega_{UH}/\omega_{ce} = 3-7$ and the parameters considered in zebras, we found very good agreement.

We think that some small differences between the numerical and analytical results are caused by differences in the two methods. In numerical simulations, as in reality, the DPR instability works in some regions of the k -vector space, not only with one k -vector as assumed in the analytical theory. Furthermore, in some of the present simulations we found deviations from the assumption made in the analytical approach ($k_{\perp} \gg k_{\parallel}$).

We computed the saturation energies of the generated upper-hybrid waves, which is beyond the possibilities of the analytical theory. We compared the results of the multi-mode and specific-mode models considering the same physical parameters. We found very good agreement between the results from both types of model. This agreement is caused by a dominance of the wave with the maximal growth rate during an evolution of the double plasma resonance instability. Therefore we used the specific-mode models, which considerably save computational time, for the computation of the saturation energies in a broad range of the parameter s . A use of the specific-mode models is also justified by a very good agreement between the growth rates computed numerically and analytically. We found that the saturation energy decreases with increasing s and this decrease is exponential. This exponential dependance of the saturation energy can be used for an extrapolation of the saturation energies for the parameter s even greater than 18, which is useful for the interpretation of zebras with many zebra stripes (Karlický & Yasnov 2015; Yasnov & Karlický 2015).

Acknowledgements. We acknowledge support from Grants 16-13277S and 17-16447S of the Grant Agency of the Czech Republic. Computational resources were provided by the CESNET LM2015042 and the CERIT Scientific Cloud LM2015085, provided under the programme “Projects of Large Research, Development, and Innovations Infrastructures”.

References

- Benáček, J., Karlický, M., & Yasnov, L. 2017, *A&A*, **598**, A106
- Buneman, O., & Storey, L. R. O. 1985, *Simulations of fusion plasmas by A 3-D, E-M particle code*, *Tech. Rep.*
- Dory, R. A., Guest, G. E., & Harris, E. G. 1965, *Phys. Rev. Lett.*, **14**, 131
- Karlický, M., & Bárta, M. 2008, *Sol. Phys.*, **247**, 335
- Karlický, M., & Yasnov, L. V. 2015, *A&A*, **581**, A115
- Ledenev, V. G., Karlický, M., Yan, Y., & Fu, Q. 2001, *Sol. Phys.*, **202**, 71
- Matsumoto, H., & Omura, Y. 1993, *Computer Space Plasma Physics: Simulation Techniques and Software* (Tokyo: Terra Scientific Pub. Co), 305
- Melrose, D. B., & Dulk, G. A. 1982, *ApJ*, **259**, 844
- Treumann, R. A., Nakamura, R., & Baumjohann, W. 2011, *Ann. Geophys.*, **29**, 1673
- Winglee, R. M., & Dulk, G. A. 1986, *ApJ*, **307**, 808
- Yasnov, L. V., & Karlický, M. 2004, *Sol. Phys.*, **219**, 289
- Yasnov, L. V., & Karlický, M. 2015, *Sol. Phys.*, **290**, 2001
- Zaitsev, V. V., & Stepanov, A. V. 1983, *Sol. Phys.*, **88**, 297
- Zheleznyakov, V. V., & Zlotnik, E. Y. 1975, *Sol. Phys.*, **44**, 461
- Zlotnik, E. Y. 2013, *Sol. Phys.*, **284**, 579

Appendix D



Growth Rates of the Upper-Hybrid Waves for Power-Law and Kappa Distributions with a Loss-Cone Anisotropy

L.V. Yasnov^{1,2} · J. Benáček³  · M. Karlický⁴

Received: 19 April 2018 / Accepted: 13 February 2019 / Published online: 5 March 2019
© Springer Nature B.V. 2019

Abstract Fine structures of radio bursts play an important role in the diagnostics of the solar flare plasma. Among them the zebras, which are prevalently assumed to be generated by the double-plasma resonance instability, belong to the most important ones. In this paper we compute the growth rate of this instability for two types of the electron distribution: a) for the power-law distribution and b) for the kappa distribution, in both cases with the loss-cone type anisotropy. We find that the growth rate of the upper-hybrid waves for the power-law momentum distribution strongly depends on the pitch-angle boundary. The maximum growth rate is found for the pitch angle $\theta_c \approx 50^\circ$. For small angles the growth rate profile is very flat and for high pitch angles the wave absorption occurs. Furthermore, analyzing the growth rate of the upper-hybrid waves for the kappa momentum distribution we find that a decrease of the characteristic momentum p_k shifts the maximum of the growth rate to lower values of the ratio of the electron-plasma and electron-cyclotron frequencies, and the frequency widths of the growth rate peaks are very broad. But if we consider the kappa distribution which is isotropic up to some large momentum p_m and anisotropic with loss-cone above this momentum then distinct peaks of the growth rate appear and thus distinct zebra stripes can be generated. It means that the restriction of small momenta for the anisotropic part of distributions is of principal importance for the zebra stripe generation. Finally, for the zebra stripes observed on 1 August 2010, the growth rates in dependence

J. Benáček
jbenacek@physics.muni.cz

L.V. Yasnov
l.yasnov@spbu.ru

M. Karlický
karlicky@asu.cas.cz

- ¹ St.-Petersburg State University, St.-Petersburg, 198504, Russia
- ² St.-Petersburg branch of Special Astrophysical Observatory, 196140, St.-Petersburg, Russia
- ³ Department of Theoretical Physics and Astrophysics, Masaryk University, Kotlářská 2, 611 37 Brno, Czech Republic
- ⁴ Astronomical Institute, Academy of Sciences of the Czech Republic, 251 65 Ondřejov, Czech Republic

on the radio frequency are computed. It is shown that in this case the growth rate peaks are more distinct than in usually presented dependencies of growth rates on the ratio of the plasma and cyclotron frequencies.

Keywords Sun: corona · Sun: flares · Sun: radio radiation

1. Introduction

The zebra structure is a fine structure of Type IV radio bursts observed during solar flares in the *decimetric, metric and centimetric wavelength ranges* (Slottje, 1972; Chernov *et al.*, 2012; Tan *et al.*, 2012, 2014). There are many models of this fine structure (Rosenberg and Tarnstrom, 1972; Zheleznyakov and Zlotnik, 1975; Kuijpers, 1975; Chernov, 1976, 1990; LaBelle *et al.*, 2003; Bárta and Karlický, 2006; Ledenev, Yan, and Fu, 2006; Kuznetsov and Tsap, 2007; Laptukhov and Chernov, 2009; Tan, 2010; Karlický, 2013), see also reviews by Chernov (2010), Chernov, Yan, and Fu (2014), Zheleznyakov *et al.* (2016). Among these models the most commonly used model is based on the double-plasma resonance (DPR) instability; see *e.g.* the review by Zheleznyakov *et al.* (2016).

The process of the double-plasma resonance, which generates upper-hybrid waves, is most effective in flare loop regions, where the condition $\omega_p \simeq s\omega_B$ is fulfilled (ω_p and ω_B means the electron-plasma and electron-gyro frequency, s is the gyro-harmonic number). However, this process strongly depends on distributions of accelerated electrons. In many papers (Zheleznyakov and Zlotnik, 1975; Winglee and Dulk, 1986; Yasnov and Karlický, 2004; Benáček, Karlický, and Yasnov, 2017; Yasnov, Benáček, and Karlický, 2017; Benáček and Karlický, 2018) studying zebra stripes the distribution of accelerated electrons were described by the Dory–Guest–Harris (DGH) type function (Dory, Guest, and Harris, 1965). However, this distribution has no clear physical foundation. The distributions that are a result of processes of accelerations and reflections of electrons in magnetic mirrors in closed magnetic loops are physically more acceptable (Stepanov, 1974; Kuijpers, 1974; White, Melrose, and Dulk, 1983). Therefore Winglee and Dulk (1986) considered the loss-cone distribution with an exponential function of the momentum of electrons. Furthermore, in the paper by Kuznetsov and Tsap (2007), the authors considered the loss-cone distribution with a power-law function of the momentum of electrons. This distribution is more realistic because it is used in a power-law fitting of hard X-ray spectra of solar flares. But in this distribution the low-energy cut-off needs to be defined, which is difficult to estimate from observations (Holman *et al.*, 2003; Saint-Hilaire and Benz, 2005; Kontar, Dickson, and Kašparová, 2008). Therefore, in recent years interest in the kappa distribution has been increasing. This distribution has no low-energy cut-off and is close to a Maxwellian distribution at low energies and at high energies is similar to the power-law one. Kappa distributions are supported by theoretical considerations of particle acceleration in collisional plasmas (Bian *et al.*, 2014). Furthermore, the X-ray spectra of coronal X-ray sources are well fitted using kappa distributions (Kašparová and Karlický, 2009; Oka *et al.*, 2013, 2015).

In the present article, first of all, we follow the study of Kuznetsov and Tsap (2007). We extend their analysis in order to show changes of the growth rate for the power-law momentum distribution in dependence on the low-energy cut-off and loss-cone angle. Then we present growth rates for the anisotropic kappa distribution and the kappa distribution which is isotropic up to some large momentum and anisotropic above this momentum. Finally, for the first time, for the zebra stripes observed on 1 August 2010, we compute the growth rates in dependence on the radio frequency.

2. Growth Rates for Power-Law Distributions

Let us briefly describe the growth rate calculation. We follow the method according to Kuznetsov and Tsap (2007). We consider a plasma with two components: a) a background Maxwellian plasma and b) a hot non-equilibrium plasma component, with the plasma densities n_0 and n_h , respectively, where $n_0 \gg n_h$. The electron distribution function of this hot non-equilibrium component is taken as

$$f(p, \theta) = \varphi(p) \begin{cases} 0, & \theta \leq \theta_c - \Delta\theta_c, \\ \frac{\theta - \theta_c + \Delta\theta_c}{\Delta\theta_c}, & \theta_c - \Delta\theta_c < \theta < \theta_c, \\ 1, & \theta > \theta_c. \end{cases} \quad (1)$$

This function describes the distribution with the loss-cone having the pitch-angle boundary θ_c and the boundary width $\Delta\theta_c \ll 1$. The function $\varphi(p)$ describes the distribution in dependence on the electron momentum.

Here the $\varphi(p)$ function is taken in the power-law function form:

$$\varphi(p) = \begin{cases} \frac{\delta-3}{2\pi(\pi-\theta_c)p_m^3} \left(\frac{p}{p_m}\right)^{-\delta}, & p \geq p_m, \\ 0, & p < p_m, \end{cases} \quad (2)$$

where p_m is the low-momentum cut-off, and δ is the power-law index. Note that this distribution is normalized to 1.

Generally, for the growth rate of the upper-hybrid waves we can write

$$\gamma = -\frac{\text{Im } \epsilon_{\parallel}}{\frac{\partial \text{Re } \epsilon_{\parallel}}{\partial \omega} \Big|_{\epsilon_{\parallel}=0}}, \quad (3)$$

$$\frac{\partial \text{Re } \epsilon_{\parallel}}{\partial \omega} \Big|_{\epsilon_{\parallel}=0} \simeq \frac{2}{\omega} \left(2 - \frac{\omega_p^2}{\omega^2} \right), \quad (4)$$

where ϵ_{\parallel} is dielectric permeability and ω is the frequency of the upper-hybrid waves.

For the term $\text{Im } \epsilon_{\parallel}$ we use Equation 17 from the paper by Kuznetsov and Tsap (2007)

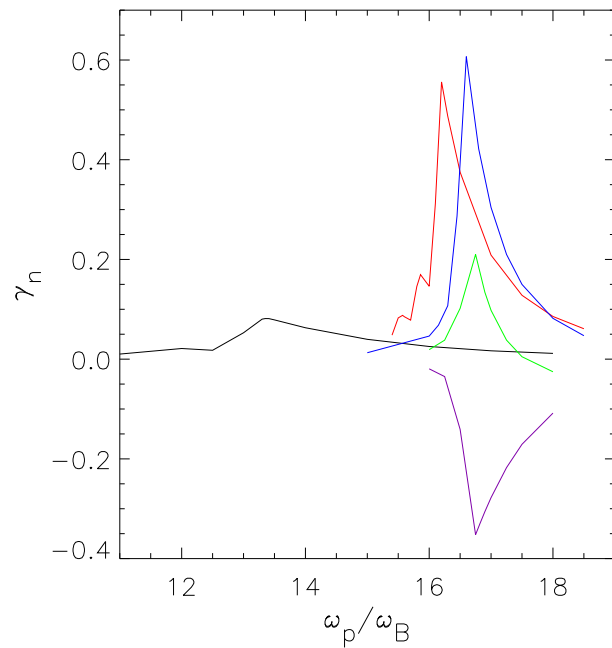
$$\begin{aligned} \text{Im } \epsilon_{\parallel}^{(s)} \simeq & -2\pi^2 m^4 c^2 \frac{\omega_p^2}{k^2} \frac{n_h}{n_0} \Gamma_r^3 J_s^2 \left(\frac{k_{\perp} p_{\perp}}{m\omega_B} \right) \\ & \times \left[\frac{\partial \varphi(p)}{\partial p} + \frac{\varphi(p) \tan \theta_c}{p \Delta\theta_c} \left(\frac{s\omega_B}{\Gamma_r \omega \sin^2 \theta_c} - 1 \right) \right] \frac{\Delta p_z}{p_0}, \end{aligned} \quad (5)$$

where J_s is the s th order Bessel function, ω_B is the electron-cyclotron frequency, $\mathbf{p} = (p_{\perp}, p_{z0}) = (p_0 \sin \theta_c, p_0 \cos \theta_c)$ is the electron momentum, m is the electron mass, c is the speed of light, k is the wave number. The distance in momentum space Δp_z between intersection points with a straight line for small parameter $\Delta\theta_c \ll 1$ is

$$\Delta p_z = 2p_{z0} \frac{\omega}{s\omega_B} \sqrt{2\Delta\theta_c \tan \theta_c}. \quad (6)$$

Then the normalized growth rate can be expressed in agreement with the paper by Kuznetsov and Tsap (2007) as

Figure 1 Maximum growth rate of the upper-hybrid waves for the power-law momentum distribution in dependence on the ratio ω_p/ω_B and the loss-cone angle 10° (black line), 30° (red line), 50° (blue line), 65° (green line) and 80° (violet line). The power-law index of the power-law distribution is $\delta = 5$, the gyro-harmonic number is $s = 16$ and the minimum electron momentum p_m corresponds to the velocity $0.3 c$, *i.e.* to the low-energy cut-off ≈ 30 keV.



$$\gamma_n = \frac{\gamma}{\omega_p} \frac{n_0}{n_h} \sqrt{\Delta\theta_c} = \frac{4}{\sqrt{2}} \pi^2 m^4 c^2 \frac{\omega \omega_p}{k^2} \Gamma_r^4 J_s^2 \left(\frac{k_\perp p_0 \sin \theta_c}{m \omega_B} \right) \times \varphi(p_0) \frac{\tan^{3/2}(\theta_c) \cos(\theta_c)}{p_0 (2 - \frac{\omega_p^2}{\omega^2})} \left(\frac{1}{\Gamma_r^2 \sin^2 \theta_c} - 1 \right), \quad (7)$$

where p_0 is the lower boundary for hot electron momentum

$$p_0 = \frac{mc \sqrt{\omega^2 - s^2 \omega_B^2}}{s \omega_B}, \quad (8)$$

$\mathbf{k} = (k_z, k_\perp)$ is the wave vector with the components along and in the perpendicular direction to the magnetic field,

$$\mathbf{k}^2 = k_z^2 + k_\perp^2 = \frac{\omega^2 - s^2 \omega_B^2}{c^2 \cos^2(\theta_c)} + \frac{\omega^4 - \omega^2 \omega_p^2 - \omega_B^2 \omega_p^2}{3 v_T^2 \omega_p^2}, \quad (9)$$

Γ_r is the relativistic factor

$$\Gamma_r = \frac{\omega}{s \omega_B}, \quad (10)$$

and v_T is the thermal velocity of the background plasma.

Now using Equation 7 we compute the growth rate for the following parameters: The lower limit for the momentum of electrons p_m is taken as corresponding to the minimum energy $E_m \approx 30$ keV, *i.e.*, to the minimum velocity of electrons $v_m/c = 0.3$, the power-law index is $\delta = 5$ and the gyro-harmonic number is $s = 16$. The pitch-angle boundary varies as $\theta_c = 10^\circ, 30^\circ, 50^\circ, 65^\circ$ and 80° and the temperature of the background plasma is $T_0 = 3 \times 10^6$ K.

In the computations we only vary the magnetic field B , while the plasma frequency is kept constant ($f_p = \omega_p/2\pi = 1$ GHz). For each value of ω_p/ω_B the growth rate γ_n is computed in the frequency interval $\sqrt{\omega_p^2 + \omega_B^2} < \omega \leq \omega_{\max}$. The frequency ω_{\max} is taken in

an experimental way in order to find the maximum value of γ_n in this interval. The results of these computations are shown in Figure 1. As seen here the growth rate strongly depends on the value of the pitch-angle boundary. The maximum peak is for $\theta_c \approx 50^\circ$. For small angles no distinct peak is visible, and for high angles the absorption appears.

Now, let us analyze an effect of variation of p_m (i.e., the low-velocity limit of electrons) on the growth rate. The result for $\delta = 5$ and $\theta_c = 50^\circ$ is shown in Figure 2. The value of p_m varies in correspondence with the minimum electron velocity $v_m \in (0.5 c - v_T)$, $v_T = 6.75 \times 10^6 \text{ m s}^{-1}$. Figure 2 shows that the maximum contrast between peaks is for the growth rates with the minimum electron velocities in the $0.3 c - 10 v_T$ range; see also Table 1. For velocities greater than $0.5 c$ the contrast of the peaks decreases and for the velocities $\leq 5 v_T$ the peaks are shifted to much lower ratios of ω_p/ω_B . If we accept that the growth rate profiles correspond to the intensity of the zebra stripes, it means that for low p_m no zebra stripes can be generated.

The same computations are made also for the power-law distribution with the power-law index $\delta = 10$. The computed growth rates for this power-law distribution with different pitch angles are shown in Figure 3. Similar to the case with the power-law distribution with the power-law index $\delta = 5$, we can see a strong dependence on the pitch angle, however, the maximum is one again for the pitch angle $\theta_c \approx 50^\circ$. On the other hand, the growth rates are higher and narrower in frequency than in the previous case.

Summarizing all these results, in Table 1 we present the ratio $(\omega_p/\omega_B)_m$, where the growth rate has maximum and the peak width $\Delta(\omega_p/\omega_B)$ (taken at half of the maximum) in dependence on the minimum electron velocity v_m (minimum of p_m) for the gyro-harmonic number $s = 16$ and for the power-law index $\delta = 5$ and 10. To see separate zebra stripes the peak width needs to be smaller than 0.5. Meanwhile, for the power-law index $\delta = 5$ the zebra structure can be formed only in a limited interval of v_m around the velocity $10 v_T = 6.75 \times 10^7 \text{ m s}^{-1}$; in the case with $\delta = 10$ the widths of the growth rates are twice smaller and thus more favorable for the zebra pattern generation. The positions of the growth rate maxima in both cases are approximately the same.

3. Growth Rates for Kappa Distributions

Now, we consider a plasma with the hot component having the kappa distribution with the loss-cone anisotropy for all electron momenta. The kappa distribution is taken as (Bian *et al.*, 2014)

$$f_\kappa(v) = \frac{n_\kappa \Gamma(\kappa + 1)}{\pi^{\frac{3}{2}} \theta_\kappa^3 \kappa^{\frac{3}{2}} \Gamma(\kappa - \frac{1}{2})} \left(1 + \frac{v^2}{\kappa \theta_\kappa^2}\right)^{-\kappa-1}, \quad (11)$$

where κ is the kappa index, $n_\kappa = \int f d^3 v$,

$$\theta_\kappa^2 = \frac{2k_B T_\kappa}{m} \frac{\kappa - \frac{3}{2}}{\kappa}, \quad (12)$$

is the characteristic velocity, m is the electron mass, k_B is the Boltzmann constant, T_κ is the mean kinetic temperature and Γ is the Gamma function.

Similar to the calculation of the growth rate for the power-law distribution we assume the loss-cone type distribution according to Equation 1. However, in this case the function

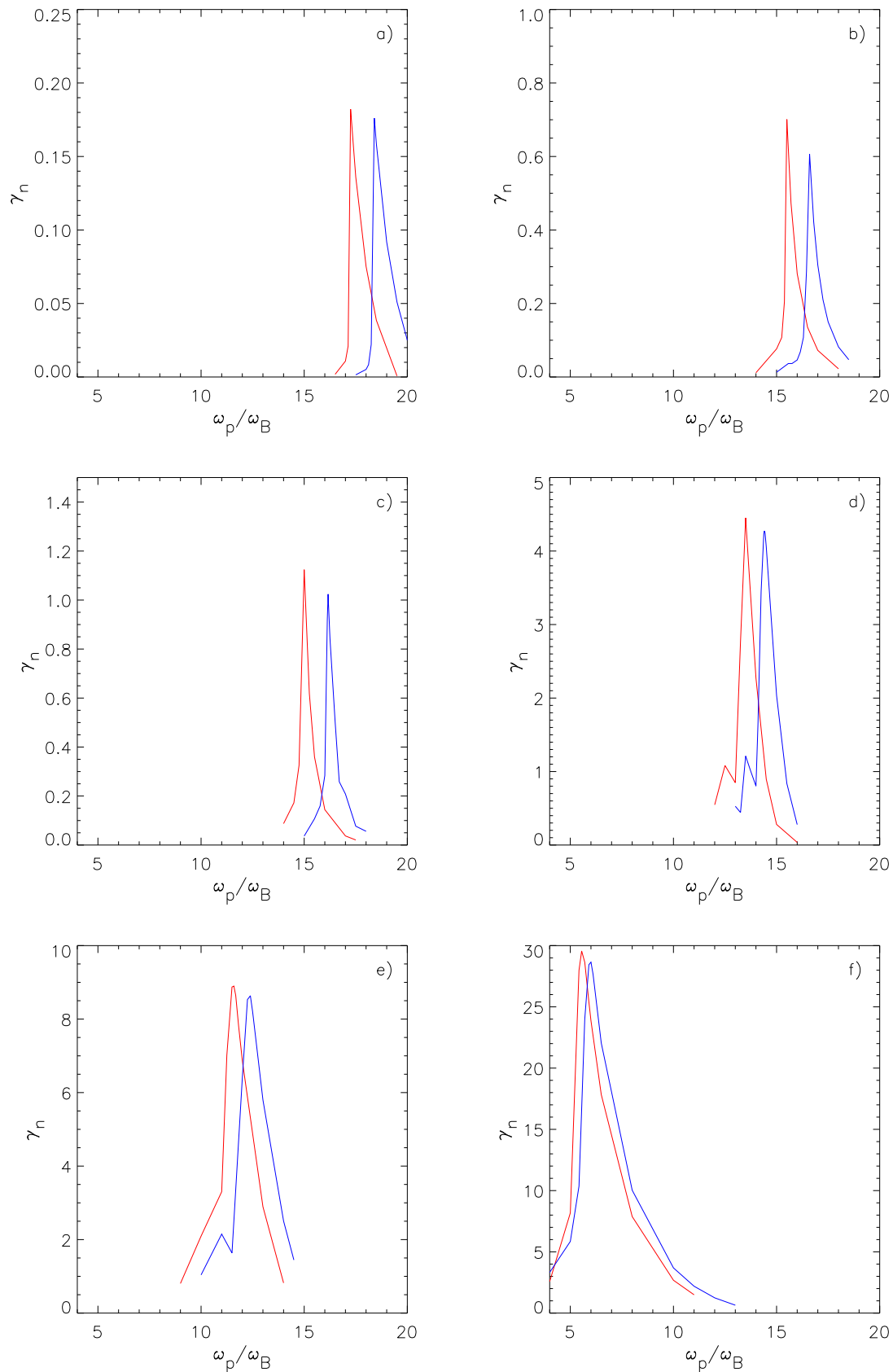
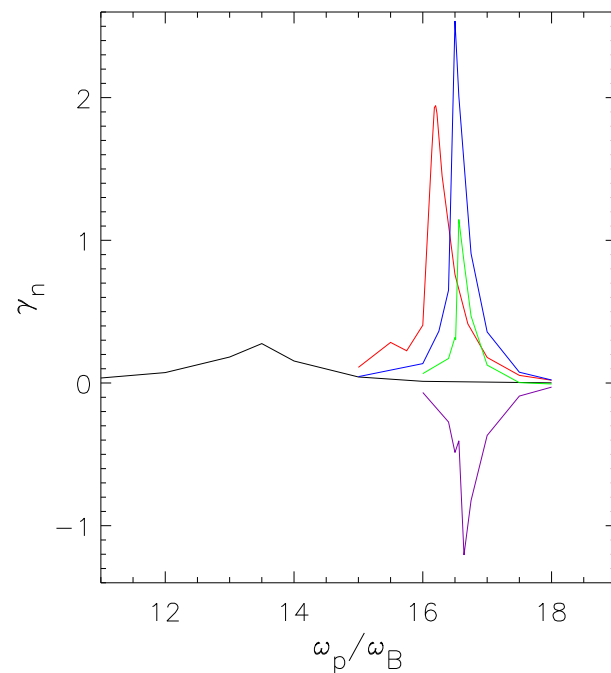


Figure 2 Maximum growth rate of the upper-hybrid waves for the power-law momentum distribution in dependence on the ratio ω_p/ω_B and the minimum electron momentum p_m for the gyro-harmonic number $s = 15$ (red line) and $s = 16$ (blue line). Plot **a)** is for p_m corresponding to the velocity $0.5 c$, **b)** for p_m corresponding to $0.3 c$, **c)** for p_m corresponding to $10 v_T$, **d)** for p_m corresponding to $5 v_T$, **e)** for p_m corresponding to $3 v_T$, and **f)** for p_m corresponding to v_T . The power-law index is $\delta = 5$ and the loss-cone is $\theta_c = 50^\circ$. Note that the scale on the y-axis increases from plot **a)** to **f)**.

Table 1 Frequency ratio of the growth rate maximum $(\omega_p/\omega_B)_m$ and the bandwidth of the growth rate peak $\Delta(\omega_p/\omega_B)$ for the harmonic number $s = 16$ in dependence on the minimum velocity v_m (corresponding to p_m) of the power-law distribution for two power-law indices ($\delta = 5$ and 10).

δ	v_m	0.5 c	0.3 c	10 v_T	5 v_T	v_T
5	$(\omega_p/\omega_B)_m$	18.41	16.60	16.16	14.42	5.98
5	$\Delta(\omega_p/\omega_B)$	0.73	0.56	0.46	0.84	1.90
10	$(\omega_p/\omega_B)_m$	18.43	16.50	15.95	14.41	6.00
10	$\Delta(\omega_p/\omega_B)$	0.40	0.26	0.25	0.61	1.19

Figure 3 Maximum growth rate of the upper-hybrid waves for the power-law momentum distribution in dependence on the ratio ω_p/ω_B and the loss-cone angle 10° (black line), 30° (red line), 50° (blue line), 65° (green line) and 80° (violet line). The power-law index of the power-law distribution is $\delta = 10$, the gyro-harmonic number is $s = 16$ and the minimum electron momentum p_m corresponds to the velocity 0.3 c, i.e. to the low-energy cut-off ≈ 30 keV.

$\varphi(p)$, derived from Equation 11, has the form

$$\varphi(p) = \frac{2\Gamma(\kappa + 1)}{\pi^{\frac{3}{2}} p_\kappa^3 \kappa^{\frac{3}{2}} \Gamma(\kappa - \frac{1}{2})(\pi - \theta_\kappa)} \left(1 + \frac{p^2}{\kappa p_\kappa^2}\right)^{-\kappa-1}, \quad (13)$$

where p is the electron momentum and $p_\kappa = m\theta_\kappa$.

Using these relations we compute the maximum growth rates for the kappa momentum distributions with the loss-cone anisotropy. The results are shown in Figures 4, 5 and 6. Figure 4 presents the growth rate in dependence on the ratio ω_p/ω_B for the kappa distribution with the kappa index $\kappa = 1.5$ (it corresponds to $\delta = 5$ for the power-law distribution) for the gyro-harmonic numbers $s = 15$ (red solid line) and 16 (red dashed line), $\theta_c = 30^\circ$, and p_κ corresponding to the velocity 0.3 c). The growth rate for the same parameters, but for $\kappa = 4$, are expressed by the blue solid line for $s = 15$ and by the blue dashed line for $s = 16$. As seen in this figure when the kappa index increases, i.e. the kappa distribution becomes closer to the Maxwellian one, the bandwidths of the growth rate peaks are broader. Furthermore, while the values of growth rates for $s = 15$ and 16 and $\kappa = 1.5$ are similar, the value of the growth rate for $s = 16$ and $\kappa = 4$ is much smaller than that with $s = 15$.

Figure 4 Maximum growth rate of the upper-hybrid waves for the kappa momentum distribution in dependence on the ratio ω_p/ω_B for the kappa index $\kappa = 1.5$ and the gyro-harmonic number $s = 15$ (red solid line), $k = 1.5$ and $s = 16$ (red dotted line), $k = 4$ and $s = 15$ (blue solid line), and $\kappa = 4$ and $s = 16$ (blue dotted line). The loss-cone is $\theta_c = 30^\circ$, and p_κ corresponds to the velocity $0.3 c$.

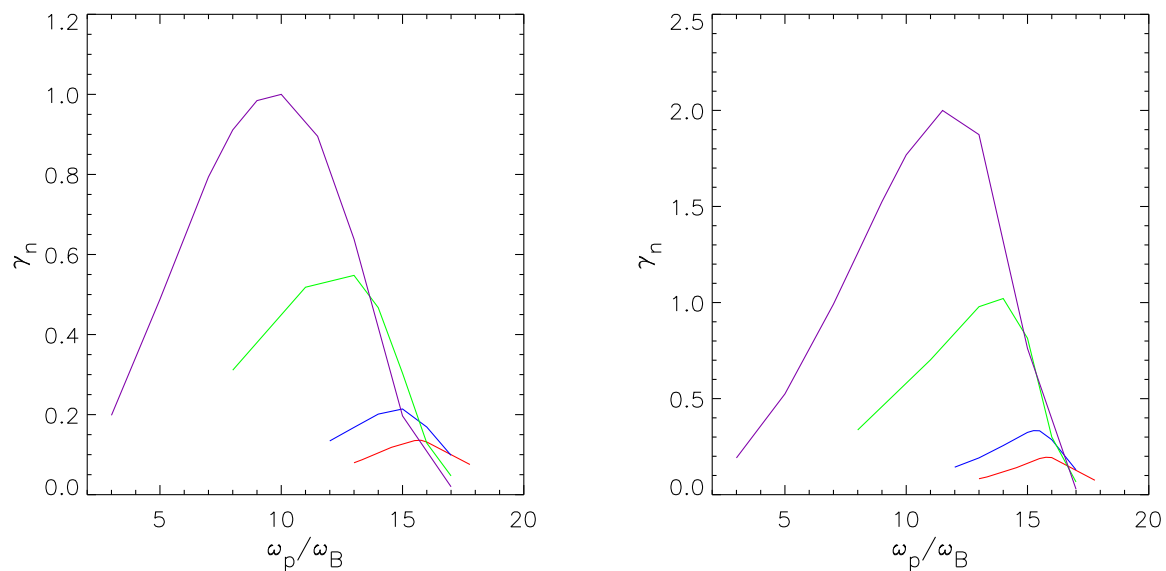
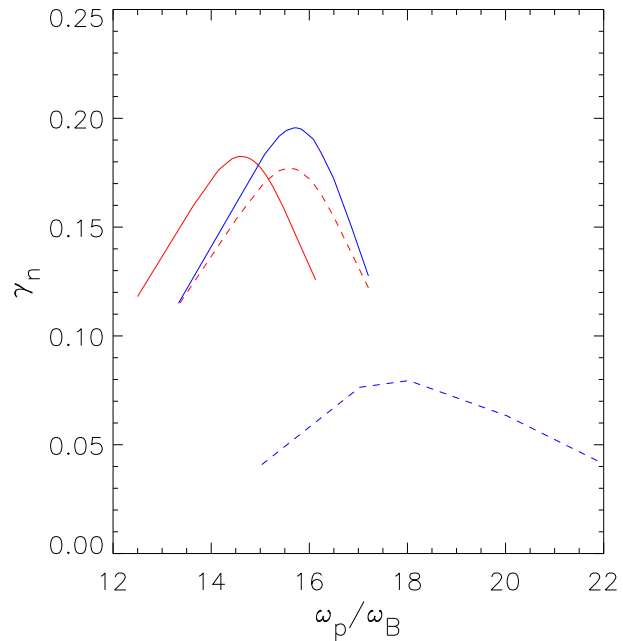
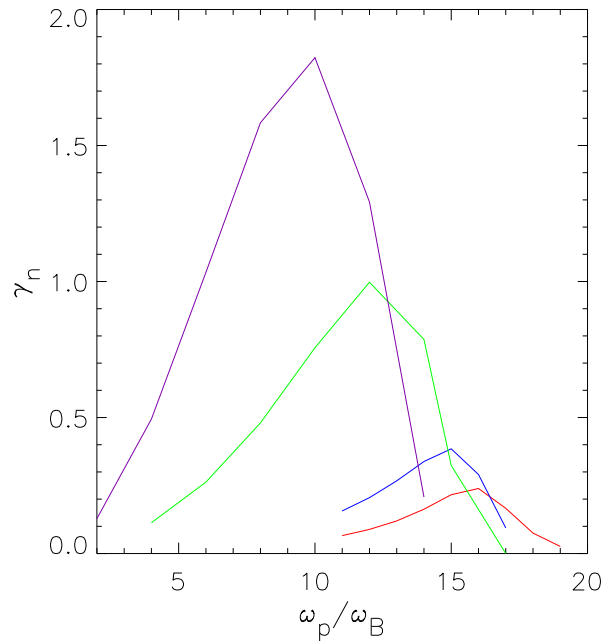


Figure 5 *Left:* Maximum growth rate of the upper-hybrid waves for the kappa momentum distribution in dependence on the ω_p/ω_B . The kappa index is $\kappa = 1.5$, the gyro-harmonic number is $s = 16$ and the loss-cone is $\theta_c = 30^\circ$. The red line is for p_κ corresponding to $0.3 c$, the blue line for p_κ corresponding to $10 v_T$, the green line for p_κ corresponding to $5 v_T$, and the violet line for p_κ corresponding to $3 v_T$. *Right:* The same, but for $\theta_c = 50^\circ$.

Furthermore, in Figure 5 we show the dependence of the growth rate for the kappa distribution in dependence on the ratio ω_p/ω_B and p_κ for two values of the loss-cone angle $\theta_c = 30^\circ$ and 50° . As seen in both these figures, when we decrease p_κ the maximum of the growth rate increases and shifts to lower values of the ratio ω_p/ω_B . The growth rates for $\theta_c = 50^\circ$ are greater than those for $\theta_c = 30^\circ$.

Finally, for comparison with Figure 5 left, in Figure 6 we added the growth rates for the kappa distribution in dependence on the ratio ω_p/ω_B for the kappa index $\kappa = \infty$. The plots of the growth rates are similar, but the values of the growth rates for $\kappa = \infty$ are higher.

Figure 6 Maximum growth rate of the upper-hybrid waves for the kappa momentum distribution in dependence on the ω_p/ω_B . The kappa index is $\kappa = \infty$, the gyro-harmonic number is $s = 16$ and the loss-cone is $\theta_c = 30^\circ$. The red line for p_κ corresponding to $0.3 c$, the blue line for p_κ corresponding to $10 v_T$, the green line for p_κ corresponding to $5 v_T$, and the violet line for p_κ corresponding to $3 v_T$.



In both Figures 5 and 6 in all cases the peaks of the growth rates are very broad. If we assume that the growth rate profiles correspond to radio emission, it means that in the case with the kappa momentum distribution distinct zebra stripes cannot be generated.

Therefore now we consider a more realistic case, namely, the kappa distribution in all momenta ($p > 0$), isotropic up to some large momentum p_m and anisotropic above this momentum p_m . Now the isotropic part of the kappa distribution plays a role of the dense background plasma and the anisotropic part with the kappa momentum distribution and loss-cone anisotropy plays a role of the low density hot component. Such a division of the distribution is possible due to the fact that only the anisotropic part of this distribution is important for the growth rate of the upper-hybrid waves. The isotropic part of the kappa distribution does not contribute to the growth rate. Therefore for the following computations only the anisotropic part with momenta above p_m needs to be expressed. For it we take the distribution, which is normalized to 1, as follows:

$$\varphi(p) = \begin{cases} \frac{(2\kappa-1) \left(\frac{p^2}{p_m^2} + \frac{\kappa p_\kappa^2}{p_m^2} \right)^{-\kappa-1}}{2\pi(\pi-\theta_c) p_m^3 {}_2F_1\left(\kappa-\frac{1}{2}; \kappa+1; \kappa+\frac{1}{2}; -\frac{\kappa p_\kappa^2}{p_m^2}\right)}, & p > p_m, \\ 0, & p \leq p_m, \end{cases} \quad (14)$$

where ${}_2F_1(\kappa - \frac{1}{2}; \kappa + 1; \kappa + \frac{1}{2}; -\kappa)$ is the hypergeometric function.

For this distribution function we computed the maximum growth rates of the upper-hybrid waves in dependence on the ratio ω_p/ω_B for $\theta_c = 50^\circ$, $\kappa = 1.5$, $s = 16$ and $s = 15$, and $p_\kappa = p_m$ corresponding to $0.3 c$.

Figure 7 shows that the kappa distribution, bounded at small momentum values, also yields peaks in the spectrum of the growth rate which are distinctly isolated, similar to the peaks for the power-law distribution (compare with Figure 2b).

4. Frequency Spectrum of Growth Rates

Zebras are observed in the spectrum in dependence on the radio frequency, not in the spectrum depending on the ratio ω_p/ω_B . Therefore, it is of interest to compute such a frequency

Figure 7 Maximum growth rate of the upper-hybrid waves for the kappa momentum distribution 14 in dependence on the ω_p/ω_B . The kappa index is $\kappa = 1.5$, the gyro-harmonic number $s = 15$ (red line) and $s = 16$ (blue line), the loss-cone is $\theta_c = 50^\circ$, $p_\kappa = p_m$ corresponds to 0.3 c.

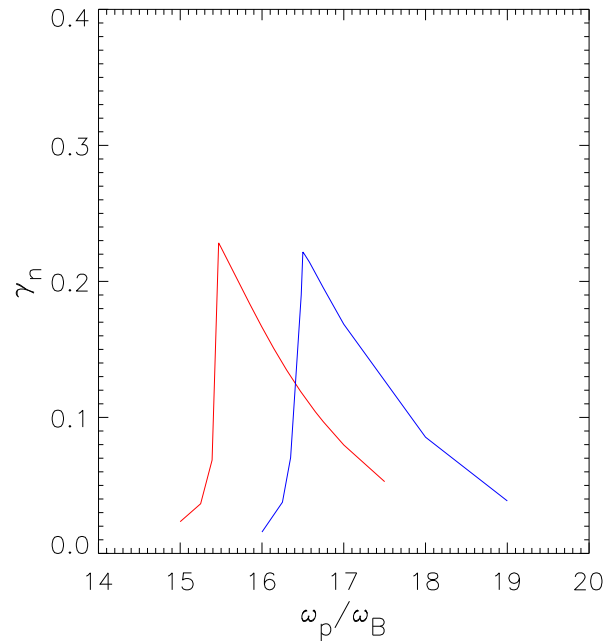
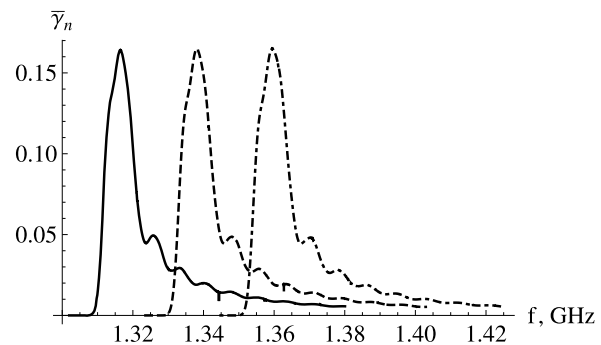


Figure 8 Dependence of the growth rate of the upper-hybrid waves on the frequency f for the distribution 14, with $\kappa = 1.5$, $\theta_c = 50^\circ$, p_m corresponds to the velocity 0.3 c. The solid line is for $s = 25$, the dashed line for $s = 26$ and the dot-dashed line for $s = 27$.



spectrum. For it we need to take the plasma frequency from some observed zebra stripes. In the following computations, we take them for three stripes of the zebra ($s = 25, 26$ and 27) observed in the 1 August flare (Yasnov, Karlický, and Stupishin, 2016): $f_p = 1.344 \times 10^9$ Hz for $s = 25$, $f_p = 1.323 \times 10^9$ Hz for $s = 26$ and $f_p = 1.301 \times 10^9$ Hz for $s = 27$. To obtain the frequency spectrum, it is necessary to integrate the above derived growth rates with respect to ω_p/ω_B , setting for each band its own plasma frequency,

$$\bar{\gamma}_n = \int \gamma_n d\left(\frac{\omega_p}{\omega_B}\right). \quad (15)$$

Figure 8 shows the dependence of the growth rate of the upper-hybrid waves on the frequency f for the distribution 14, with $\kappa = 1.5$, $\theta_c = 50^\circ$, p_m corresponds to the velocity 0.3 c. Here and in the following, the value of p_κ is taken as corresponding to the temperature of the thermal plasma ($T_e = 3 \times 10^6$ K). As seen here the spectrum shows distinct isolated peaks giving in the spectrum distinct stripes. An analogous result was also obtained for the power distribution, not shown here.

Now, let us check if the conclusion as regards the significant influence of the value of the pitch-angle boundary on the frequency spectra is valid. Figure 9 shows the frequency spectrum of the growth rate of the upper-hybrid waves for the distributions 14 with $\theta_c = 80^\circ$, $\kappa = 1.5$ and p_m corresponding to velocity 0.3 c. As seen here, similar to the case with the

Figure 9 Dependence of the growth rate of the upper-hybrid waves on the frequency f for the distribution 14, with $\kappa = 1.5$, $\theta_c = 80^\circ$, p_m corresponds to the velocity 0.3 c. The solid line is for $s = 25$, the dashed line for $s = 26$ and the dot-dashed line for $s = 27$.

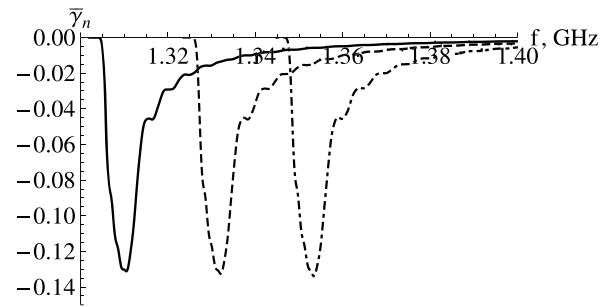


Figure 10 Dependence of the growth rate of the upper-hybrid waves on the frequency f for the distribution 14, with $\kappa = 1.5$, $\theta_c = 10^\circ$, p_m corresponds to the velocity 0.3 c. The solid line is for $s = 25$, the dashed line for $s = 26$ and the dot-dashed line for $s = 27$.

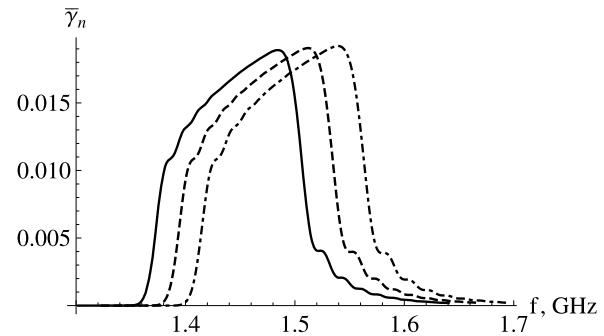


Table 2 Frequencies of the growth rate maxima and their frequency differences in dependence on θ_c and v_m for the gyro-harmonic numbers $s = 25, 26$ and 27 .

θ_c ($^\circ$)	v_m	$f_{\max}^{s=25}$ (GHz)	$f_{\max}^{s=26}$ (GHz)	$f_{\max}^{s=27}$ (GHz)	$\Delta f(s = 25 - 26)$ (GHz)	$\Delta f(s = 26 - 27)$ (GHz)
50	0.2 c	1.381	1.359	1.337	0.022	0.022
50	0.3 c	1.359	1.338	1.317	0.021	0.021
50	0.4 c	1.365	1.347	1.328	0.018	0.019
30	0.3 c	1.379	1.358	1.336	0.021	0.022
65	0.3 c	1.356	1.334	1.313	0.022	0.021

power-law distribution, the growth rates are negative. Note that the negative spectral peaks are well separated from each other.

Figure 10 shows the frequency spectrum of the growth rate of the upper-hybrid waves for the distribution 14 with $\theta_c = 10^\circ$, $\kappa = 1.5$ and p_m corresponding to velocity 0.3 c. Now the spectral bands are very broad. As a result, these bands merge and thus do not form isolated peaks, which are necessary for zebra stripe generation.

Finally, we compute the growth rate of the upper-hybrid waves for the distribution 14 in dependence on frequency with $\kappa = 1.5$, for different θ_c and p_m (corresponding to the velocity v_m). Other values in computations are taken the same as for Figure 8. In Table 2 we show the frequencies of the growth rate maxima and frequency differences of their maxima. It seems that for $\theta_c = 50^\circ$ the frequency difference slightly decreases with the increase of v_m . For fixed v_m this difference (within errors of computations corresponding to the last number in Δf) practically does not depend on θ_c .

5. Discussion and Conclusions

It was shown that the growth rate of the upper-hybrid waves for the power-law momentum distribution with the low-momentum cut-off and the loss-cone anisotropy strongly depends on the pitch-angle boundary. The maximum growth rate was found for the pitch angle $\theta_c \approx 50^\circ$. For small angles the growth rate is broad and flat and for high pitch angles even absorption occurs.

We made computations for two power-law indices for $\delta = 5$ and 10. While for the power-law index $\delta = 5$ the zebra structure can be formed only in a limited interval of v_m around the velocity $10 v_T = 6.75 \times 10^7 \text{ m s}^{-1}$, in the case with $\delta = 10$ the width of the growth rates are twice smaller and thus more favorable for the zebra pattern generation. The positions of the growth rate maxima in both cases are approximately the same. These results agree with those of Kuznetsov and Tsap (2007).

An analysis of the growth rate of the upper-hybrid waves for the anisotropic kappa momentum distribution for all electron momenta ($p > 0$) (which is a contribution to the dense background plasma) shows the following:

- i) When we decrease the characteristic momentum p_κ then the maximum of the growth rate is shifted to lower values of ω_p/ω_B .
- ii) The growth rates for the kappa distribution with $\kappa = 1.5$ and $\kappa = \infty$ shows a similar behavior, but values of the growth rates for $\kappa = \infty$ are a little bit higher. It is due to the fact that in this case the distribution with $\kappa = \infty$ has more electrons for low momentum values than that with $\kappa = 1.5$.
- iii) The frequency widths of the growth rate maxima are very broad.

We also found that the frequency difference between the frequencies of the growth rate maxima slightly decreases with the increase of v_m . For fixed v_m this difference practically does not depend on θ_c .

But if we take a more realistic distribution, namely, the single kappa distribution which is isotropic up to some large momentum p_m and anisotropic with loss-cone above this momentum, then distinct peaks of the growth rate appear and thus distinct zebra stripes can be generated. It means that the restriction for small momenta for the anisotropic part of distributions (power-law or kappa) is of principal importance for the zebra stripe generation.

For the first time, the dependence of the growth rate on the radio frequency was computed. In this case the spectral peaks are much more distinct than in the case of the dependence of the growth rate on the ratio of the plasma and cyclotron frequencies. Thus, analyzing the observed radio spectra, we can assume smaller values of the power-law or kappa indices.

Note that, for high values of the pitch-angle anisotropy, where the absorption occurs, the inverse zebra stripes can be produced on some radio continua.

Acknowledgements We thank an anonymous referee for valuable comments. M. Karlický acknowledges support from Grants 17-16447S and 18-09072S of the Grant Agency of the Czech Republic. L.V. Yasnov acknowledge support from Grant 18-29-21016-mk and partly from Grant 18-02-00045 of the Russian Foundation for Basic Research. This work was supported by The Ministry of Education, Youth and Sports from the Large Infrastructures for Research, Experimental Development and Innovations project IT4Innovations National Supercomputing Center LM2015070.

Disclosure of Potential Conflicts of Interest No potential conflict of interest was reported by the authors.

Publisher's Note Springer Nature remains neutral with regard to jurisdictional claims in published maps and institutional affiliations.

References

- Bárta, M., Karlický, M.: 2006, Interference patterns in solar radio spectra: high-resolution structural analysis of the corona. *Astron. Astrophys.* **450**, 359. DOI. ADS.
- Benáček, J., Karlický, M.: 2018, Double plasma resonance instability as a source of solar zebra emission. *Astron. Astrophys.* **611**, A60. DOI. ADS.
- Benáček, J., Karlický, M., Yasnov, L.: 2017, Temperature dependent growth rates of the upper-hybrid waves and solar radio zebra patterns. *Astron. Astrophys.* **598**, A106. DOI. ADS.
- Bian, N.H., Emslie, A.G., Stackhouse, D.J., Kontar, E.P.: 2014, The formation of Kappa-distribution accelerated electron populations in solar flares. *Astrophys. J.* **796**, 142. DOI. ADS.
- Chernov, G.P.: 1976, Microstructure in the continuous radiation of type IV meter bursts. Observations and model of the source. *Soviet Astron.* **20**, 449. ADS.
- Chernov, G.P.: 1990, Whistlers in the solar corona and their relevance to fine structures of type IV radio emission. *Solar Phys.* **130**, 75. DOI. ADS.
- Chernov, G.P.: 2010, Recent results of zebra patterns in solar radio bursts. *Res. Astron. Astrophys.* **10**, 821. DOI. ADS.
- Chernov, G.P., Yan, Y.-H., Fu, Q.-J.: 2014, The importance of source positions during radio fine structure observations. *Res. Astron. Astrophys.* **14**, 831. DOI. ADS.
- Chernov, G.P., Sych, R.A., Meshalkina, N.S., Yan, Y., Tan, C.: 2012, Spectral and spatial observations of microwave spikes and zebra structure in the short radio burst of May 29, 2003. *Astron. Astrophys.* **538**, A53. DOI. ADS.
- Dory, R.A., Guest, G.E., Harris, E.G.: 1965, Unstable electrostatic plasma waves propagating perpendicular to a magnetic field. *Phys. Rev. Lett.* **14**, 131. DOI. ADS.
- Holman, G.D., Sui, L., Schwartz, R.A., Emslie, A.G.: 2003, Electron bremsstrahlung hard X-ray spectra, electron distributions, and energetics in the 2002 July 23 solar flare. *Astrophys. J. Lett.* **595**, L97. DOI. ADS.
- Karlický, M.: 2013, Radio continua modulated by waves: zebra patterns in solar and pulsar radio spectra? *Astron. Astrophys.* **552**, A90. DOI. ADS.
- Kašparová, J., Karlický, M.: 2009, Kappa distribution and hard X-ray emission of solar flares. *Astron. Astrophys.* **497**, L13. DOI. ADS.
- Kontar, E.P., Dickson, E., Kašparová, J.: 2008, Low-energy cutoffs in electron spectra of solar flares: statistical survey. *Solar Phys.* **252**, 139. DOI. ADS.
- Kuijpers, J.: 1974, A coherent radiation mechanism for type IV DM radio bursts. *Solar Phys.* **36**, 157. DOI. ADS.
- Kuijpers, J.: 1975, A unified explanation of solar type IV DM continua and ZEBRA patterns. *Astron. Astrophys.* **40**, 405. ADS.
- Kuznetsov, A.A., Tsap, Y.T.: 2007, Loss-cone instability and formation of zebra patterns in type IV solar radio bursts. *Solar Phys.* **241**, 127. DOI. ADS.
- LaBelle, J., Treumann, R.A., Yoon, P.H., Karlický, M.: 2003, A model of zebra emission in solar type IV radio bursts. *Astrophys. J.* **593**, 1195. DOI. ADS.
- Laptukhov, A.I., Chernov, G.P.: 2009, Concerning mechanisms for the zebra pattern formation in the solar radio emission. *Plasma Phys. Rep.* **35**, 160. DOI. ADS.
- Ledenev, V.G., Yan, Y., Fu, Q.: 2006, Interference mechanism of “zebra-pattern” formation in solar radio emission. *Solar Phys.* **233**, 129. DOI. ADS.
- Oka, M., Ishikawa, S., Saint-Hilaire, P., Krucker, S., Lin, R.P.: 2013, Kappa distribution model for hard X-ray coronal sources of solar flares. *Astrophys. J.* **764**, 6. DOI. ADS.
- Oka, M., Krucker, S., Hudson, H.S., Saint-Hilaire, P.: 2015, Electron energy partition in the above-the-looptop solar hard X-ray sources. *Astrophys. J.* **799**, 129. DOI. ADS.
- Rosenberg, H., Tarnstrom, G.: 1972, Frequency separation in structure of solar continuum radio bursts. *Solar Phys.* **24**, 210. DOI. ADS.
- Saint-Hilaire, P., Benz, A.O.: 2005, Thermal and non-thermal energies of solar flares. *Astron. Astrophys.* **435**, 743. DOI. ADS.
- Slottje, C.: 1972, Peculiar absorption and emission microstructures in the type IV solar radio outburst of March 2, 1970. *Solar Phys.* **25**, 210. DOI. ADS.
- Stepanov, A.V.: 1974, A mechanism for generating type IV solar radio bursts. *Soviet Astron.* **17**, 781. ADS.
- Tan, B.: 2010, A physical explanation of solar microwave zebra pattern with the current-carrying plasma loop model. *Astrophys. Space Sci.* **325**, 251. DOI. ADS.
- Tan, B., Yan, Y., Tan, C., Sych, R., Gao, G.: 2012, Microwave zebra pattern structures in the X2.2 solar flare on 2011 February 15. *Astrophys. J.* **744**, 166. DOI. ADS.
- Tan, B., Tan, C., Zhang, Y., Mészáros, H., Karlický, M.: 2014, Statistics and classification of the microwave zebra patterns associated with solar flares. *Astrophys. J.* **780**, 129. DOI. ADS.

- White, S.M., Melrose, D.B., Dulk, G.A.: 1983, Electron cyclotron masers during solar flares. *Proc. Astron. Soc. Aust.* **5**, 188. [ADS](#).
- Winglee, R.M., Dulk, G.A.: 1986, The electron-cyclotron maser instability as a source of plasma radiation. *Astrophys. J.* **307**, 808. [DOI](#). [ADS](#).
- Yasnov, L.V., Benáček, J., Karlický, M.: 2017, Brightness temperature of radio zebras and wave energy densities in their sources. *Solar Phys.* **292**, 163. [DOI](#). [ADS](#).
- Yasnov, L.V., Karlický, M.: 2004, The growth rate of upper-hybrid waves and dynamics of microwave zebra structures. *Solar Phys.* **219**, 289. [DOI](#). [ADS](#).
- Yasnov, L.V., Karlický, M., Stupishin, A.G.: 2016, Physical conditions in the source region of a zebra structure. *Solar Phys.* **291**, 2037. [DOI](#). [ADS](#).
- Zheleznyakov, V.V., Zlotnik, E.Y.: 1975, Cyclotron wave instability in the corona and origin of solar radio emission with fine structure. III. Origin of zebra-pattern. *Solar Phys.* **44**, 461. [DOI](#). [ADS](#).
- Zheleznyakov, V.V., Zlotnik, E.Y., Zaitsev, V.V., Shaposhnikov, V.E.: 2016, Double plasma resonance and its manifestations in radio astronomy. *Phys. Usp.* **59**, 997. [DOI](#). [ADS](#).

Appendix E



Growth Rates of the Electrostatic Waves in Radio Zebra Models

Jan Benáček¹ and Marian Karlický²

¹ Department of Theoretical Physics and Astrophysics, Masaryk University, Kotlářská 2, CZ-61137 Brno, Czech Republic; jbenacek@physics.muni.cz

² Astronomical Institute of the Academy of Sciences of the Czech Republic, CZ-25165 Ondřejov, Czech Republic

Received 2019 April 23; revised 2019 June 19; accepted 2019 June 22; published 2019 August 8

Abstract

Zebras were observed not only in the solar radio emission but also in radio emissions of Jupiter and the Crab Nebula pulsar. In their models, growth rates of the electrostatic waves play an important role. Considering the plasma composed from the thermal background plasma and hot and rare component with the Dory–Guest–Harris distribution, we compute the growth rates γ and dispersion branches of the electrostatic waves in the $\omega - k_{\perp}$ domain. We show complexity of the electrostatic wave branches in the upper-hybrid band. In order to compare the results, which we obtained using the kinetic theory and particle-in-cell (PIC) simulations, we define and compute the integrated growth rate Γ , where the “characteristic width” of dispersion branches was considered. We found a very good agreement between the integrated growth rates and those from PIC simulations. For maximal and minimal Γ we showed locations of dispersion branches in the $\omega - k_{\perp}$ domain. We found that Γ has a maximum when the dispersion branches not only cross the region with high growth rates γ , but when the dispersion branches in this region are sufficiently long and wide. We also mentioned the effects of changes in the background plasma and hot component temperatures.

Key words: instabilities – methods: analytical – methods: numerical – planets and satellites: individual (Jupiter) – pulsars: individual (Crab Nebula pulsar) – Sun: radio radiation

1. Introduction

Solar radio zebras belong to the most important fine structures used in diagnostics of solar flare plasmas (Chen et al. 2011; Chernov 2011; Zlotnik 2013). Similarly, the zebras observed in the radio emission of Jupiter and the Crab Nebula pulsar (Hankins & Eilek 2007; Hankins et al. 2016; Panchenko et al. 2018) can also be used for diagnostics purposes. Among many models of all these zebras, the model based on the double plasma resonance (DPR) instability belongs to the most probable (Zheleznyakov & Zlotnik 1975b; Melrose & Dulk 1982; Zaitsev & Stepanov 1983; Winglee & Dulk 1986; Ledenev et al. 2001; Zlotnik 2013; Karlický & Yasnov 2015, 2018a, 2018b; Zlotnik et al. 2016).

In this model the DPR instability generates the upper-hybrid waves with the frequency

$$\omega^2 = \omega_{pe}^2 + \omega_{ce}^2 + 3k_{\perp}^2 v_{tb}^2, \quad (1)$$

when the resonance condition

$$\omega - \frac{k_{\parallel} u_{\parallel}}{\gamma_{rel}} - \frac{s\omega_{ce}}{\gamma_{rel}} = 0, \quad (2)$$

is fulfilled. Here ω , ω_{pe} , and ω_{ce} are the wave, electron-plasma, and electron-cyclotron frequency, $\mathbf{k} = (k_{\parallel}, k_{\perp})$ is the wave vector, v_{tb} is the thermal electron velocity of the background plasma, $\mathbf{u} = (u_{\perp}, u_{\parallel})$, $u_{\perp} = p_{\perp}/m_e$, and $u_{\parallel} = p_{\parallel}/m_e$ are the hot electron velocities perpendicular and parallel to the magnetic field; m_e is the electron mass, γ_{rel} is the relativistic Lorentz factor, s is the gyro-harmonic number, and c is the speed of light. For details, see, e.g., Benáček & Karlický (2018).

In theoretical models of the DPR instability, a two-component plasma with the background plasma having the Maxwellian distribution and hot and rare component with the Dory–Guest–Harris electron distribution for $j = 1$ (Dory et al.

1965)

$$f_{hot}(u_{\parallel}, u_{\perp}) = \frac{u_{\perp}^2}{2(2\pi)^{3/2} v_t^5} \exp\left(-\frac{u_{\perp}^2 + u_{\parallel}^2}{2v_t^2}\right), \quad (3)$$

is assumed. Here v_t we call the thermal velocity of hot electrons, although the distribution function in this relation is not Maxwellian.

In interpretations of zebra observations, which use this model, it is usually supposed that the electron-plasma frequency is related to the electron-cyclotron frequency as follows

$$\omega_{pe} \approx s\omega_{ce}. \quad (4)$$

However, Benáček et al. (2017) showed that there can be the frequency shift from this simple equation up to 16% for Dory–Guest–Harris velocity distribution and even higher for other velocity distributions (Yasnov et al. 2017).

Besides the zebra model based on DPR instability, there is the model that explains zebras by a nonlinear interaction of Bernstein modes (Kuznetsov 2005; Zlotnik & Sher 2009). This model was supported by zebra observations made by Altyntsev et al. (2005). In principle, Bernstein modes can also be generated in the upper-hybrid band. Both the upper-hybrid waves and Bernstein mode are the electrostatic (longitudinal) waves. Because in the upper-hybrid band in some cases it is difficult to distinguish these waves; therefore, in the following we use the general term—the electrostatic waves.

As will be shown in the following, in the upper-hybrid band (i.e., at frequencies close to the upper-hybrid frequency) there can be several dispersion branches of the unstable electrostatic waves in which energy can grow simultaneously. Therefore, we define the “characteristic width” of dispersion branches and compute the wave growth rates integrated over the upper-hybrid band. Thus, for the first time we compare the results obtained using the analytical kinetic theory with the results of

particle-in-cell (PIC) simulations. We study the integrated growth rate dependent on the ratio of the electron-plasma and electron-cyclotron frequency and in relation to positions of the wave dispersion branches in the $\omega - k_\perp$ domain. We use a three-dimensional PIC model. Note that PIC models naturally give the integrated growth rates.

The paper is structured as follows. In Section 2 we start with a theory of the electrostatic (longitudinal) waves perpendicular to the magnetic field. The integrated growth rates of these waves in the upper-hybrid band computed from the analytical relations are in Section 3. Section 4 includes the growth rates obtained numerically. A discussion of the results and our conclusions are in Section 5.

2. Electrostatic Waves in the Upper-hybrid Band and Their Growth Rates

Let us consider the plasma composed from the background Maxwellian plasma with the density n_e and the thermal velocity v_{tb} and hot plasma having the density n_h and the “thermal” velocity v_t , where $n_h \ll n_e$. Then the dispersion relation of the electrostatic (longitudinal) waves in such a plasma is given by the permittivity tensor

$$\epsilon_{\parallel} = \epsilon_{\parallel}^{(0)} + \epsilon_{\parallel}^{(1)} = 0, \quad (5)$$

where the term $\epsilon_{\parallel}^{(0)}$ corresponds to the background Maxwellian plasma and the term $\epsilon_{\parallel}^{(1)}$ is a correction to the hot and rare plasma component.

In our case with $n_h \ll n_e$ and in agreement with Chen (1974), Zheleznyakov (1996), and Fitzpatrick (2015) we can write

$$\epsilon_{\parallel}^{(0)} = 1 - 2\omega_{pe}^2 \frac{e^{-\lambda}}{\lambda} \sum_{l=1}^{\infty} \frac{l^2 I_l(\lambda)}{\omega^2 - l^2 \omega_{ce}^2} = 0, \quad (6)$$

$$\omega_{pe}^2 = \frac{n_e e^2}{m_e \epsilon_0}, \quad \lambda = \frac{k_\perp^2 v_{tb}^2}{\omega_{ce}^2}, \quad (7)$$

where ω_{pe} and ω_{ce} are the plasma frequency of the background plasma and the electron-cyclotron frequency, ϵ_0 is the permittivity of free space, λ is the dimensionless parameter, $I_l(\lambda)$ is the modified Bessel function of l th order, m_e is the electron mass, e is the electron charge, ω is the wave frequency, $\mathbf{k} = (k_\parallel, k_\perp)$ is the wave vector parallel and perpendicular to the direction of the magnetic field, respectively.

Solutions of the real part of Equation (6) are the dispersion relations for the upper-hybrid waves as well as for the Bernstein waves. Because in the present paper we are interested about these waves in the upper-hybrid band, where it sometimes is a problem to distinguish between these waves; therefore, in the following we use the common term for them: the electrostatic waves.

For the growth rate of these waves, we can write (Zheleznyakov & Zlotnik 1975a)

$$\gamma(\omega, k_\perp) = - \frac{\text{Im } \epsilon_{\parallel}^{(1)}}{\left[\frac{\partial \text{Re } \epsilon_{\parallel}^{(0)}}{\partial \omega} \right]_{\epsilon_{\parallel}^{(0)}=0}}. \quad (8)$$

Table 1
Parameters Used for Computing of the Growth Rates

Parameter	Value
v_{tb}	0.018 c (2 MK)
v_t	0.2 c
n_e/n_h	32
f_{hot}	DGH
ω_{pe}/ω_{ce}	4.0–5.3
$k_\perp c/\omega_{pe}$	0–15 range
ω/ω_{pe}	0–2 range

In accordance with Kuznetsov (2005, Appendix A) the nominator of Equation (8) can be written as

$$\text{Im}(\epsilon_{\parallel}^{(1)}) = -2\pi^2 m_e^4 \frac{\omega_{pe}^2}{k^2} \sum_{l=s+1}^{\infty} ab^2 \times \int_0^\pi J_l \left(\frac{\gamma_{\text{rel}} k_\perp v_\perp}{\omega_{ce}} \right) \frac{\gamma_{\text{rel}}^5 \sin \phi}{\frac{\partial \psi}{\partial \rho}} \frac{l \omega_{ce}}{\gamma_{\text{rel}} v_\perp} \frac{\partial f}{\partial p_\perp} d\phi, \quad (9)$$

$$\frac{\partial \psi}{\partial \rho} = \frac{\gamma_{\text{rel}}^2 l \omega_{ce}}{c^2} (v_\parallel^2 + v_\perp^2), \quad (10)$$

$$v_\parallel = -a \cos(\phi), \quad v_\perp = b \sin(\phi), \quad (11)$$

$$a^2 = \frac{l^2 \omega_{ce}^2 c^2 (l^2 \omega_{ce}^2 - \omega^2)}{l^4 \omega_{ce}^4}, \quad (12)$$

$$b^2 = \frac{c^2 (l^2 \omega_{ce}^2 - \omega^2)}{l^2 \omega_{ce}^2}, \quad (13)$$

where c is the speed of light, v_\parallel and v_\perp are the velocities on resonance ellipse in Equation (2). f is the electron velocity distribution function in the form

$$f(v_\perp, v_\parallel) = f_0(v_\perp, v_\parallel) + \frac{n_h}{n_e} f_{\text{hot}}(v_\perp, v_\parallel). \quad (14)$$

The f_0 means the background Maxwellian distribution for temperature v_{tb} , f_{hot} is in our case the Dory–Guest–Harris distribution given by Equation (3) described by the “thermal” velocity v_t and $J_l(\lambda)$ is the Bessel function.

Furthermore, the denominator of Equation (8) can be expressed as

$$\frac{\partial \epsilon_{\parallel}}{\partial \omega} = 4\omega \omega_{pe}^2 \frac{e^{-\lambda}}{\lambda} \sum_{l=1}^{\infty} \frac{l^2 I_l(\lambda)}{(\omega^2 - l^2 \omega_{ce}^2)^2}. \quad (15)$$

3. Analytical Growth Rates

In this section, we compute the growth rates using analytically derived equations expressed in the previous section. As an example we make computations for the ratio of the electron-plasma and electron-cyclotron frequency (ω_{pe}/ω_{ce}) in the 4.0–5.3 range. Namely, we want to determine the growth rates also for a noninteger ratio of ω_{pe}/ω_{ce} . The relatively low values of this ratio are chosen due to a comparison with the numerical simulations, where computations with the low values of ω_{pe}/ω_{ce} are more reliable.

If we do not mention explicitly, in our analytical computations and also in the following numerical simulations, we use the parameters shown in Table 1. Considering the propagation of waves in the strictly perpendicular direction to the magnetic

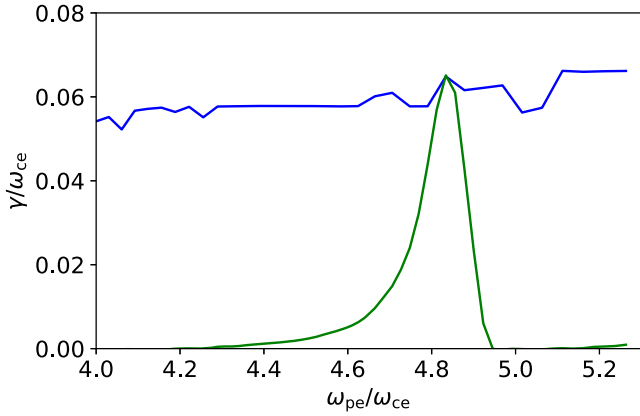


Figure 1. Maximal growth rate found at the upper-hybrid branch (Equation (1)) (green line), and at all electrostatic branches (Equation (6); blue line). The frequency and wave vector intervals are the same as for the integrated growth rate in Figure 2.

field ($k_{\parallel} = 0$) and using Equations (6) we compute their dispersion branches and growth rates in the $\omega - k_{\perp}$ domain.

Because we want the frequency precision of dispersion branches at least $10^{-8} \omega_{pe}$, we searched for a sufficient number l in relation 6. We increased l until the precision of a dispersion branch position was higher than $10^{-8} \omega_{pe}$. Thus, we got $l_{\max} = 40$ and in relation 6 we use the summation $\sum_{l=1}^{l_{\max}=40}$. The same number l is also used in the summation in Equation (9).

Roots of Equation (6) (dispersion branches) are searched numerically using the Levenberg–Marquardt damped root method (Levenberg 1944; Marquardt 1963; More et al. 1980; Press et al. 2007) from the SciPy package in Python. This method was selected for its good convergence properties and ability to find the most narrow branches. The minimization is made in variable ω . First, the $\omega - k_{\perp}$ domain is divided into the regular orthogonal grid, which gives starting values of ω and k_{\perp} for the algorithm. Typically, we use $10^3 - 10^4$ grid points in the ω direction and 20–40 grid points in k_{\perp} . In each step the method computes gradients in the Jacobian matrix and by the gradient descent method it proceeds until the required precision of ω is obtained. In our case we set this precision as $10^{-8} \omega_{pe}$. From the last step in this procedure we get the covariance matrix, which represents the gradient in a neighborhood of the found solution. We take the inverted absolute value of this gradient as the “characteristic width” of the dispersion branches, see the following. From a physical point of view the “characteristic width” of the dispersion branch is given by thermal fluctuations of the electron-plasma density. This “characteristic width” does not represent the actual relative frequency range occupied by the waves, but is rather proportional to that frequency range; the proportionality coefficient depends on many factors (fluctuations etc.), but its absolute value is unimportant for this study.

First, we compute the maxima of the growth rate γ at the upper-hybrid branch (Equation (1)) with dependance on ω_{pe}/ω_{ce} . The result is shown in Figure 1 by the green line. Then using Equation (6) we compute the maximal growth rate at all electrostatic branches in the $\omega - k_{\perp}$ domain, see the blue line in Figure 1. Note that these maximal growth rates are always taken in one specific point of the $\omega - k_{\perp}$ domain. While the growth rate at the upper-hybrid branch has distinct maximum ($\gamma/\omega_{ce} \approx 0.06$) at about $\omega_{pe}/\omega_{ce} = 4.8$, the growth

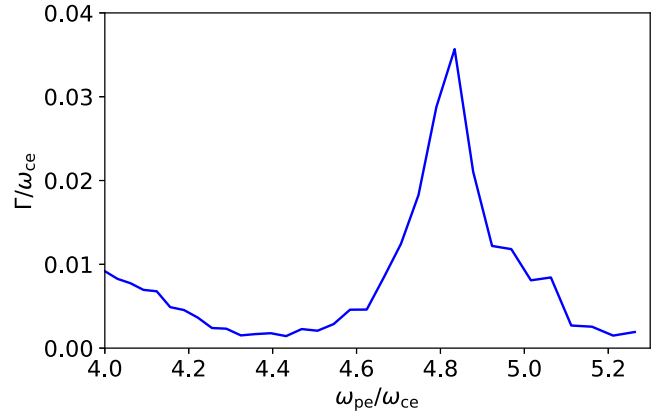


Figure 2. Integrated growth rate Γ computed from Equation (16) as a function of the ratio ω_{pe}/ω_{ce} normalized to ω_{ce} for the parameters given in Table 1. Its maximum is for $\omega_{pe}/\omega_{ce} = 4.8$ and minimum for $\omega_{pe}/\omega_{ce} = 4.4$.

rates for all branches are similar. This means that at almost all branches in the $\omega - k_{\perp}$ domain there are positive growth rates.

Because our main goal is to compare the results obtained from analytical relations with those from the following PIC simulations, where the growth rate is given by compositions of growth rates in the whole $\omega - k_{\perp}$ domain, we define a new quantity—the integrated growth rate Γ as

$$\Gamma = \frac{1}{\Gamma_0} \int \gamma(\omega, k_{\perp}) \sigma(\omega, k_{\perp}) \delta(\epsilon_{\parallel}^{(0)}(\omega, k_{\perp})) d\omega dk_{\perp}, \quad (16)$$

where δ is the Dirac delta function and $\gamma(\omega, k_{\perp})$ is the growth rate at the specific ω and k_{\perp} . This integral counts the growth rates over the dispersion branches of the electrostatic waves in the whole $\omega - k_{\perp}$ domain with their “characteristic width” σ . The function Γ_0 is the normalization factor

$$\Gamma_0 = \int \sigma(\omega, k_{\perp}) \delta(\epsilon_{\parallel}^{(0)}(\omega, k_{\perp})) d\omega dk_{\perp}. \quad (17)$$

In our case the integral is computed over the $\omega - k_{\perp}$ area with $\omega/\omega_{pe} \in (0, 2)$ and $k_{\perp}c/\omega_{pe} \in (0, 20)$. At higher frequencies the branches are very narrow and thus do not contribute effectively to the integrated growth rate and at higher values of the wave vectors $\gamma = 0$.

Using the plasma parameters from Table 1 we computed the integrated growth rates Γ (Equation (16)) for the ratios $\omega_{pe}/\omega_{ce} = 4.0 - 5.3$, see Figure 2. As can be seen in this figure, the maximum of Γ is for $\omega_{pe}/\omega_{ce} = 4.8$ and the minimum for $\omega_{pe}/\omega_{ce} = 4.4$.

Now, a question arises of how the integrated growth rate Γ is related to the positions of dispersion branches in the $\omega - k_{\perp}$ domain. To answer this question, we compute the dispersion branches in the $\omega - k_{\perp}$ domain for the maximal and minimal values of the integrated growth rate Γ . We also plot growth rates in the whole domain $\omega - k_{\perp}$, although growth rates outside dispersion branches are non-physical. It is because the growth rates are defined only for roots of Equation (6). But, we use this type of presentation to show a relation between positions of dispersion branches and regions favorable for the wave amplification.

The results are shown in Figure 3, where the growth rates and dispersion branches are in a broad area of $\omega - k_{\perp}$ (Plots a, b). The detailed views are from the upper-hybrid band (Plots c, d). We note that the parts of dispersion branches with the

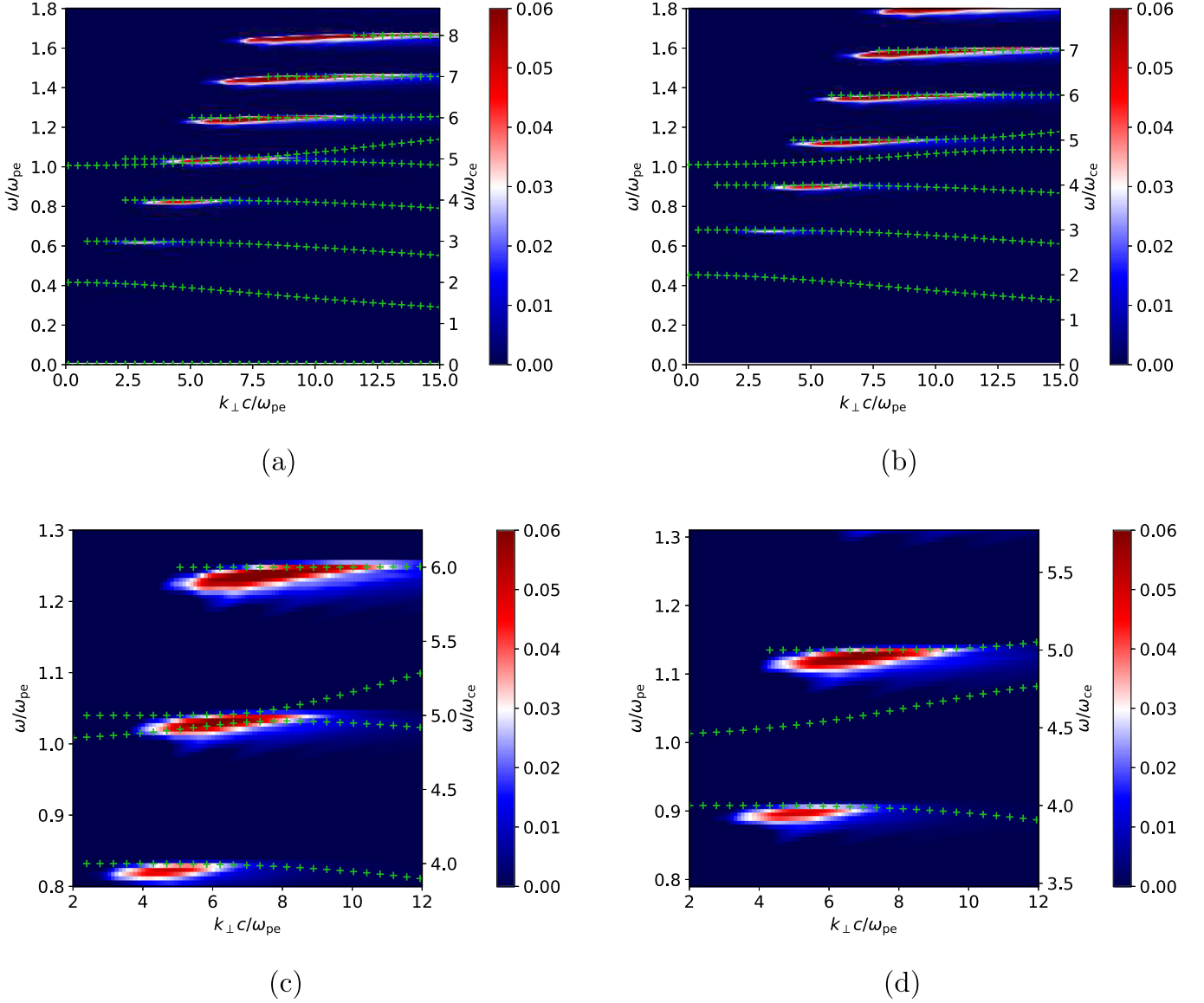


Figure 3. Analytical growth rates γ/ω_{ce} and dispersion branches in the $\omega - k_{\perp}$ domain (the blue–red scale) for the maximal value of Γ , i.e., for $\omega_{pe}/\omega_{ce} = 4.8$ (a, c) and for the minimal value of Γ , i.e., for $\omega_{pe}/\omega_{ce} = 4.4$ (b, d) taken from Figure 2. The green crosses show dispersion branches of the electrostatic waves. The growth rates and dispersion branches in a broad range of (ω, k_{\perp}) are in (a, b) and the same in a detailed view in the upper-hybrid band are in (c, d).

Table 2

“Characteristic Width” of the Dispersion Branches σ for the Maximum Γ with $\omega_{pe}/\omega_{ce} = 4.8$ (see Figure 2) and for the Minimal Γ with $\omega_{pe}/\omega_{ce} = 4.4$. ω_{branch} Means the Frequency of the Dispersion Branch for $k_{\perp}c/\omega_{pe} = 10$

Maximum			Minimum		
$\omega_{pe}/\omega_{ce} = 4.8$			$\omega_{pe}/\omega_{ce} = 4.4$		
$\omega_{branch}/\omega_{pe}$	$\omega_{branch}/\omega_{ce}$	σ	$\omega_{branch}/\omega_{pe}$	$\omega_{branch}/\omega_{ce}$	σ
0.334	1.603	7.4×10^{-3}	0.373	1.788	9.1×10^{-3}
0.593	2.846	1.0×10^{-2}	0.652	3.128	1.2×10^{-2}
0.821	3.943	1.2×10^{-2}	0.897	4.306	2.0×10^{-2}
1.030	4.945	9.9×10^{-2}	1.069	5.133	4.0×10^{-1}
1.076	5.164	3.4×10^{-1}	1.140	5.471	2.2×10^{-2}
1.250	6.001	6.6×10^{-4}	1.364	6.546	1.46×10^{-4}
1.456	6.989	1.5×10^{-5}	1.591	7.636	3.95×10^{-6}

“characteristic width” σ less than 10^{-6} are very narrow and thus they are not represented in the figure, see also the following and Table 2.

As seen here, in the $\omega - k_{\perp}$ domain there are the regions with the high growth rates. The maximal growth rate on dispersion curves in the field of view of Figure 3(c) is

$\gamma/\omega_{ce} \approx 0.06$. Comparing the cases with the maximal and minimal integrated growth rates Γ , we can see differences in distributions of the dispersion branches and growth rate regions. While in the case with the maximal Γ the dispersion branches in most cases cross the region with high growth rates γ , in the case with the minimal Γ the thickest branches are outside of these regions. Note that for the integrated growth rate not only is this crossing over these regions important but also the lengths and width (area) of the dispersion branches over these regions. Namely, the wave energy is given by the wave energy density in the area unit times the area. We suppose that the width of the dispersion branch is proportional to σ calculated during computations of the dispersion branches. Thus, there are the dispersion branches, which go through the high growth rate regions even for the minimal growth rate Γ (see Figure 3(b), e.g., the region $\omega/\omega_{pe} = 1.4$, $k = 6-15$), but their “characteristic widths” are very small and therefore do not significantly influence the integrated growth rate Γ .

In Table 2 we present the “characteristic width” of different dispersion branches σ . A difference in the “characteristic width” can be several orders. The maximal Γ appears, when the dispersion branch with the highest “characteristic width” crosses the high growth rate area around the plasma frequency, see Figure 3(c). It is interesting that in this case, two dispersion branches of the electrostatic waves are very close to each other.

To show how the dispersion branches change, in Figure 4 we present the dispersion branches for three values of the ratio $\omega_{pe}/\omega_{ce} = 4.925, 4.950$, and 4.975 . Here in the left part of the figure we can see that the dispersion branch, which is first under the plasma frequency, is going up to higher frequencies with decreasing ω_{pe}/ω_{ce} . During this shift it extrudes the upper dispersion branch up (Figure 4(c)). In the region where the branches meet, a knee is formed on the bottom dispersion branch; i.e., for lower k_{\perp} than this knee there is a part of the dispersion branch with the normal dispersion and for higher k_{\perp} is the part with the anomalous dispersion (Figure 4(c)). Thus, in some cases, the electrostatic waves are generated at the part with the normal dispersion and in others at that with the anomalous dispersion.

For the value of $v_{tb} = 0.018 c$ considered in Figures 4(a), (c), (e), this interplay of dispersion branches happens slightly out of the region with high growth rates; therefore, the integrated growth rate Γ does not have the maximal value. However, we found that for lower background thermal velocity ($v_{tb} = 0.007 c$), the dispersion branches not only meet, but they also are in the region with high growth rates (Figures 4(d), (f)) and thus for these plasma parameters the high integrated growth rate Γ can be expected.

We also studied the distribution of the growth rates γ and dispersion branches dependent on the background plasma temperature (Figure 5). With increasing the background plasma temperature the center of the region with the high growth rates remains at the same position, but the size of this region decreases. Moreover, the point where dispersion branches meet and cross the region with the high growth rates shifts to lower k_{\perp} . The reason is that for the constant $\lambda = k_{\perp}^2 v_{tb}^2 / \omega_{ce}^2$ the component of the wave vector k_{\perp} has to decrease when v_{tb} increases. It implies that for the dispersion branches close to the plasma frequency and $v_{tb} < 0.018 c$ the electrostatic waves are generated at the normal part of the dispersion branch, while for higher thermal velocities in its anomalous part.

On the other hand, Figure 6 shows the distribution of the growth rates and dispersion branches dependent on the “thermal” velocity of hot electrons v_t . With increasing this velocity the position of the region with high growth rates shifts to lower k_{\perp} . For a constant argument in the Bessel function in Equation (9), $\text{const} = \Gamma v_{\perp} k_{\perp} / \omega_{ce}$, k_{\perp} decreases as v_{\perp} increases. The region with high growth rates expands along the frequency axis with increasing v_t . However, the maximal values of γ in the region center decrease. The reason is that the value of the term $\partial f(v_{\perp}, v_{\parallel}) / \partial v_{\perp}$ decreases with increasing of v_t . For temperatures $v_t < 0.15 c$ the area of the region with high growth rates γ is so narrow that the integrated growth rate Γ is without a distinct peak.

4. Numerical Growth Rates in the PIC Model

We make simulations using a 3D PIC relativistic model (Buneman & Storey 1985; Matsumoto & Omura 1993; Karlický & Bárta 2008; Benáček & Karlický 2018) with multicore message passing interface (MPI) parallelization. Further details can be found in Matsumoto & Omura (1993, p. 67–84) and at the link below.³

The model size is $48\Delta \times 48\Delta \times 16\Delta$ in x -, y -, z -directions respectively. The generated electrostatic waves are in x - y plane, the z coordinate corresponds to the magnetic field direction. One run takes 80,000 time steps with the time step $\omega_{pe} t = 0.025$. The electron distribution function is DGH distribution, the number of electrons per cell is $n_e = 960$, the ratio of densities of the background plasma and hot electrons is $n_e/n_h = 32$, $\omega_{pe}/\omega_{ce} = 4-5.3$. Other parameters are the same as in Table 1.

Varying the ratio of ω_{pe}/ω_{ce} in the range 4.0–5.3 we made the PIC simulations and estimated the growth rates from the growth of the electrostatic wave energy (Figure 7). Note that these growth rates correspond to the integrated growth rates Γ in the analytical approach. The profile of the growth rate and the growth rate values are very similar to that presented in Figure 2. In the range of $\omega_{pe}/\omega_{ce} = 4.1-4.5$ the growth rate is very weak, and at $\omega_{pe}/\omega_{ce} = 4.88$ there is the growth rate maximum. It is at slightly higher values of ω_{pe}/ω_{ce} comparing with the maximum Γ shown in Figure 2.

5. Discussion and Conclusions

In this paper we computed two types of growth rates: (a) the growth rate γ that corresponds to one point in the $\omega - k_{\perp}$ domain, i.e., located at one specific dispersion branch and (b) the growth rate Γ integrated over the upper-hybrid band, where we took into account the fact that in real conditions as well as in PIC simulations the instability can start simultaneously not only at one point in the $\omega - k_{\perp}$ domain, but in some area in this domain and even on several dispersion branches. While the maximal growth rate γ/ω_{ce} is found to be about 0.06, the maximal integrated growth rate Γ/ω_{ce} is about 0.03. The maximal growth rate γ is similar to those presented by Zheleznyakov & Zlotnik (1975a), Winglee & Dulk (1986), and Benáček et al. (2017), but due to various thermal velocities, plasma densities, and magnetic fields used in these papers this comparison is not straightforward. For example, for the parameters as in our Table 1, Zheleznyakov & Zlotnik (1975a) and also Zlotnik & Sher (2009) found the maximal

³ <https://www.terrapub.co.jp/e-library/cspp/text/10.txt>

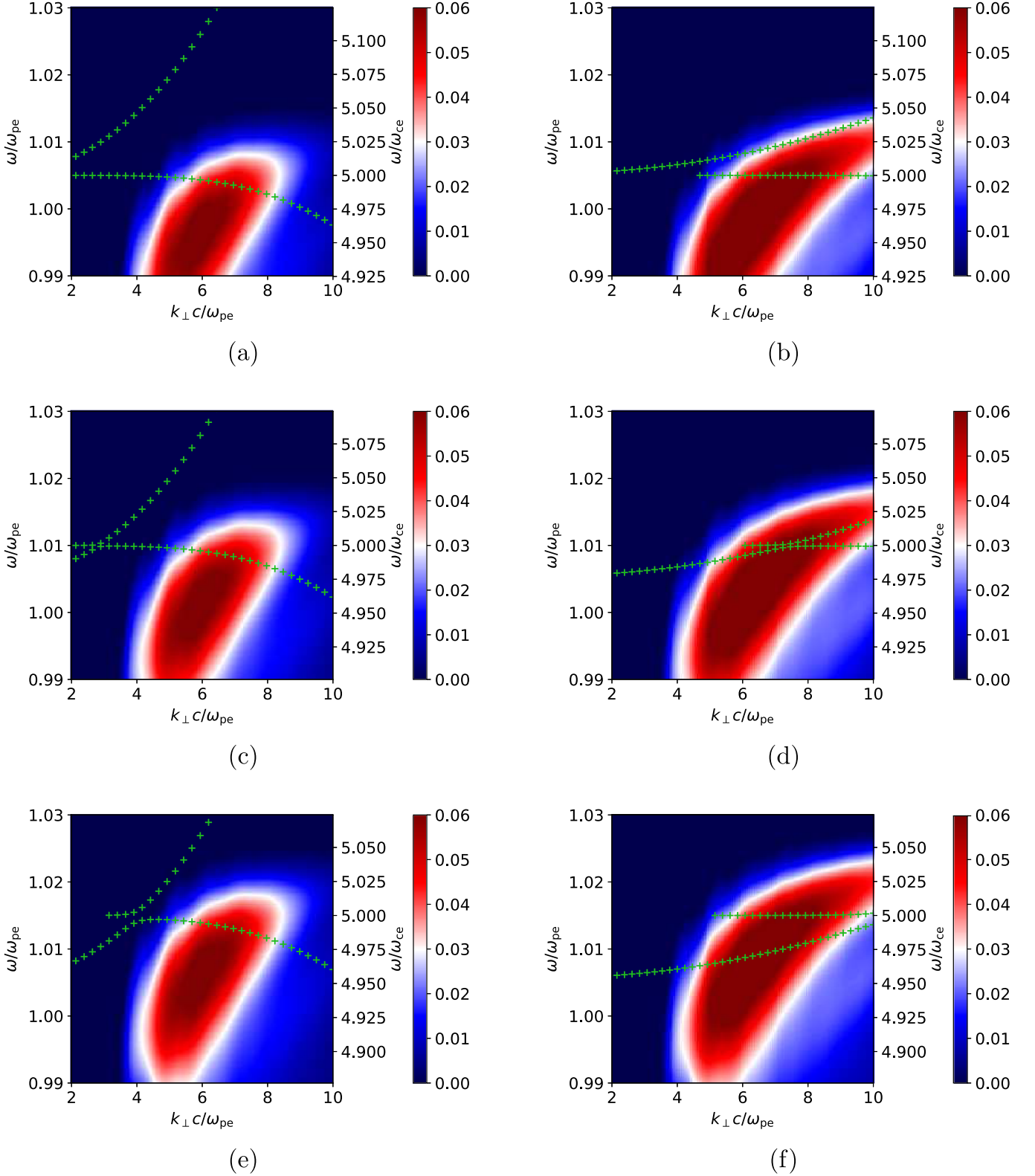


Figure 4. Analytical growth rates normalized to ω_{ce} and dispersion branches dependent on ratio ω_{pe}/ω_{ce} and 4.975 (a, b), 4.950 (c, d), and 4.925 (e, f) for two background temperatures: $v_{ib} = 0.018 c$ (a, c, e) and $v_{ib} = 0.007 c$ (b, d, f).

growth rate to be $\gamma/\omega_{ce} \approx 0.03$, which is twice smaller than our maximal growth rate $\gamma/\omega_{ce} \approx 0.06$. The difference in these values is probably due to different computational precisions in these studies.

The integrated growth rate is the parameter allowing a direct comparison with the PIC simulations, contrary to the growth rates at one branch of the electrostatic waves (Zheleznyakov & Zlotnik 1975a; Winglee & Dulk 1986; Kuznetsov 2005;

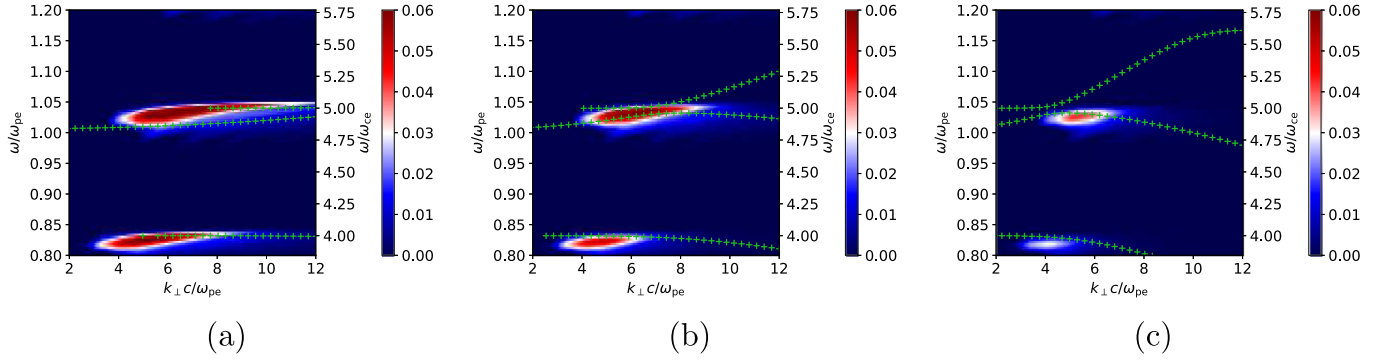


Figure 5. Analytical growth rates normalized to ω_{ce} (blue–red scale) and dispersion branches dependent on the background thermal velocity: (a) $v_{th} = 0.007 c$, (b) $v_{th} = 0.018 c$, and (c) $v_{th} = 0.030 c$. The thermal velocity of the hot component $v_t = 0.2 c$ and $\omega_{pe}/\omega_{ce} = 4.8$ are kept constant in all of these cases.

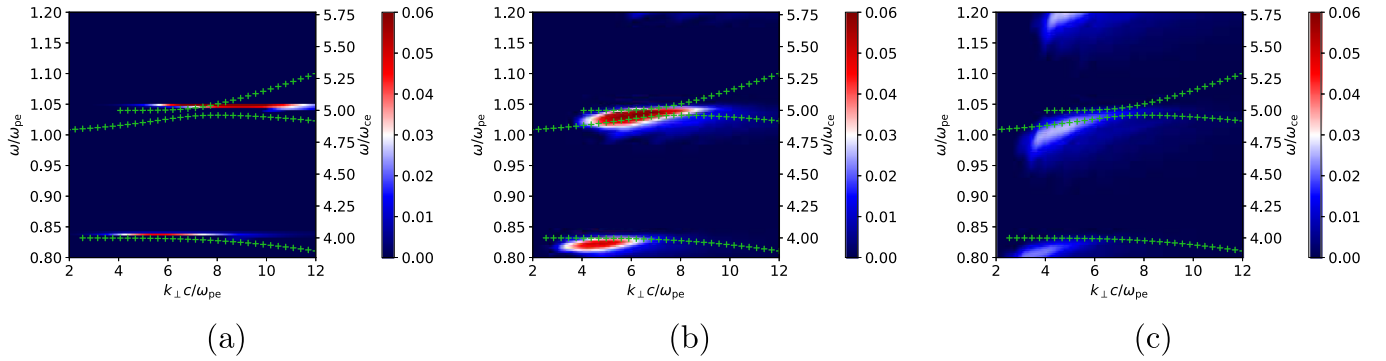


Figure 6. Analytical growth rates normalized to ω_{ce} and dispersion branches dependent on the hot electron velocity: (a) $v_t = 0.1 c$, (b) $v_t = 0.2 c$, and (c) $v_t = 0.3 c$. $v_{th} = 0.018 c$ and $\omega_{pe}/\omega_{ce} = 4.8$ are kept constant.

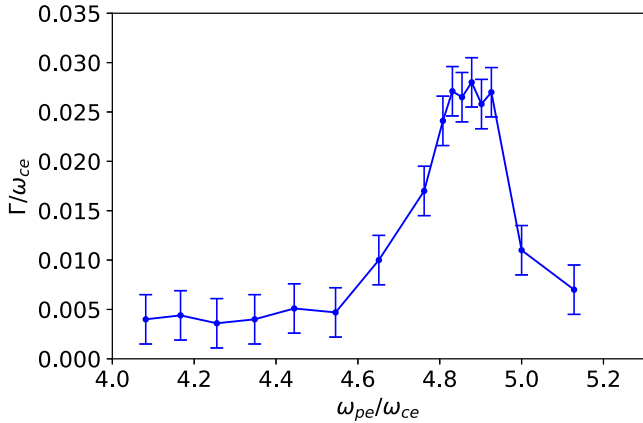


Figure 7. Growth rates from PIC simulations as a function of the ratio ω_{pe}/ω_{ce} for $v_t = 0.2 c$, $v_{th} = 0.018 c$. Compare it with Γ in Figure 2.

Zlotnik & Sher 2009; Benáček et al. 2017), see also Aschwanden (1990). In computations of the integrated growth rate we use the “characteristic width” of dispersion branches. We think that this “characteristic width” is a result of thermal fluctuations of the electron-plasma density. We found that the “characteristic width” can differ for different dispersion branches. Just these differences lead to the integrated growth rate Γ , which agrees to that computed by PIC simulations. When we would use the constant “characteristic width” of dispersion branches ($\sigma = 1$) then the integrated growth rate would be without peaks at resonances.

We found that the profile of the integrated growth rate Γ obtained by analytical calculations and that in PIC simulations are very similar and their maxima are at almost the same value of ω_{pe}/ω_{ce} . This difference can be explained by slightly different positions of dispersion branches in the analytical and numerical approaches. Namely, the condition $n_h \ll n_e$, which is used in the analytical approach, is difficult to fulfill in PIC simulations, where it has an impact on positions of dispersion branches in PIC model. We found that the growth rate peak in PIC simulations is broader than that in the analytical approach. We think that it is because in the PIC model there can also be the electrostatic waves with $k_{\parallel} \neq 0$.

We also compared the maximal Γ from the present PIC simulations with that in our previous paper (Benáček & Karlický 2018). We found that due to an error in the growth rate normalization in our previous paper the growth rate in this paper was overestimated 20 times. Considering this correction, the maximal growth rate Γ from the present paper agrees to that in the paper by Benáček & Karlický (2018).

In dispersion diagrams with dispersion branches, calculated analytically, we showed how the plasma parameters influence their positions in the $\omega - k_{\perp}$ domain. We found that when the dispersion branch with the sufficient “characteristic width” and length crosses the region with high growth rates then the integrated growth rate Γ is high.

Varying the plasma parameters, we showed that in some range of ω_{pe}/ω_{ce} the dispersion branches can meet and change the form to that with a knee. We found that sometimes a dominant contribution to the integrated growth rate Γ comes from the normal part of the dispersion branch and sometimes from the anomalous part. Moreover, when some branches meet

then it is sometimes difficult to distinguish the type of electrostatic wave.

We found that in the upper-hybrid band there can be several dispersion branches of the electrostatic waves perpendicular to the magnetic field with normal and anomalous dispersions. We showed that sometimes two branches can even meet in the $\omega - k_{\perp}$ domain. In the DPR models of radio zebras only the instability of the upper-hybrid waves with the normal dispersion (Equation (1)) is considered. Thus, in new zebra models, instabilities on all branches in the upper-hybrid band should be taken into account. Although it complicates the models, especially analytical ones, they will be more realistic than the present models. New zebra models need to describe the processes in the whole upper-hybrid band, because for the zebra emission the whole electrostatic wave energy, generated on different dispersion branches, is important. PIC models naturally solve this problem, but they also need to be improved.

We thank an anonymous referee for valuable comments. We acknowledge support from Grants 17-16447S, 18-09072S, and 19-09489S of the Grant Agency of the Czech Republic. This work was supported by The Ministry of Education, Youth and Sports from the Large Infrastructures for Research, Experimental Development and Innovations project “IT4Innovations National Supercomputing Center—“LM2015070.”

Software: Python, SciPy, Jupyter.

ORCID iDs

Jan Benáček  <https://orcid.org/0000-0002-4319-8083>

Marian Karlický  <https://orcid.org/0000-0002-3963-8701>

References

- Altynsev, A. T., Kuznetsov, A. A., Meshalkina, N. S., Rudenko, G. V., & Yan, Y. 2005, *A&A*, **431**, A1037
- Aschwanden, M. J. 1990, *A&AS*, **85**, 1141
- Benáček, J., & Karlický, M. 2018, *A&A*, **611**, A60
- Benáček, J., Karlický, M., & Yasnov, L. 2017, *A&A*, **555**, A1
- Buneman, O., & Storey, L. R. O. 1985, Simulations of fusion plasmas by A 3-D, E-M particle code, Tech. Rep., Stanford Univ.
- Chen, B., Bastian, T. S., Gary, D. E., & Jing, J. 2011, *ApJ*, **736**, 64
- Chen, F. F. 1974, Introduction to plasma physics (New York: Plenum)
- Chernov, G. 2011, Fine Structure of Solar Radio Bursts, Astrophysics and Space Science Library 375 (Heidelberg: Springer)
- Dory, R. A., Guest, G. E., & Harris, E. G. 1965, *PhRvL*, **14**, 131
- Fitzpatrick, R. 2015, Plasma physics: an introduction (Boca Raton, FL: CRC Press)
- Hankins, T. H., & Eilek, J. A. 2007, *ApJ*, **670**, 693
- Hankins, T. H., Eilek, J. A., & Jones, G. 2016, *ApJ*, **833**, 47
- Karlický, M., & Bárta, M. 2008, *SoPh*, **247**, 335
- Karlický, M., & Yasnov, L. V. 2015, *A&A*, **581**, A115
- Karlický, M., & Yasnov, L. V. 2018a, *ApJ*, **867**, 28
- Karlický, M., & Yasnov, L. V. 2018b, *A&A*, **618**, A60
- Kuznetsov, A. A. 2005, *A&A*, **438**, 341
- Ledenev, V. G., Karlický, M., Yan, Y., & Fu, Q. 2001, *SoPh*, **202**, 71
- Levenberg, K. A. 1944, *QApMa*, **2**, 164
- Marquardt, D. 1963, *SIAM J. Appl. Math.*, **11**, 431
- Matsumoto, H., & Omura, Y. 1993, Computer space plasma physics: simulation techniques and software (Tokyo: Terra Scientific Pub. Co), 305
- Melrose, D. B., & Dulk, G. A. 1982, *ApJ*, **259**, 844
- More, J. J., Garbow, B. S., & Hillstom, K. E. 1980, *User guide for MINPACK-1* Tech. Rep. No. ANL-80-74, Argonne National Lab.
- Panchenko, M., Rošker, S., Rucker, H. O., et al. 2018, *A&A*, **610**, A69
- Press, W. H., Teukolsky, S. A., Vetterling, W. T., & Flannery, B. P. 2007, Numerical Recipes 3rd Edition: The Art of Scientific Computing (New York: Cambridge Univ. Press)
- Winglee, R. M., & Dulk, G. A. 1986, *ApJ*, **307**, 808
- Yasnov, L. V., Benáček, J., & Karlický, M. 2017, *SoPh*, **292**, 163
- Zaitsev, V. V., & Stepanov, A. V. 1983, *SoPh*, **88**, 297
- Zheleznyakov, V. V. 1996, Radiation in Astrophysical Plasmas (), Vol. 204 (Berlin: Springer)
- Zheleznyakov, V. V., & Zlotnik, E. I. 1975a, *SoPh*, **43**, 431
- Zheleznyakov, V. V., & Zlotnik, E. Y. 1975b, *SoPh*, **44**, 461
- Zlotnik, E. Y. 2013, *SoPh*, **284**, 579
- Zlotnik, E. Y., Shaposhnikov, V. E., & Zaitsev, V. V. 2016, *JGRA*, **121**, 5307
- Zlotnik, E. Ya., & Sher, É. M. 2009, *R&QE*, **52**, 88

References

- ALMA. 2019, Atacama Large Millimeter/submillimeter Array, <https://www.almaobservatory.org/en/home/>
- Aschwanden, M. J. 1987, Sol. Phys., 111, 113
- Aschwanden, M. J., Benz, A. O., & Schwartz, R. A. 1993, ApJ, 417, 790
- Barrow, C. H. & Saunders, H. 1972, Astrophysical Letters, 12, 211
- Bárta, M. & Karlický, M. 2006, A&A, 450, 359
- Benáček, J., Karlický, M., & Yasnov, L. 2017, A&A, 555, A1
- Benáček, J., Karlický, M., & Yasnov, L. V. 2017, A&A, 598, A106
- Benz, A. O. & Mann, G. 1998, A&A, 333, 1034
- Bernold, T. E. X. & Treumann, R. A. 1983, ApJ, 264, 677
- Bespalov, P. & Trakhtenhertz, V. 1986, Rev. Plasma Phys., 10, 155
- Birdsall, C. K. & Langdon, A. B. 1991, Plasma Physics via Computer Simulation (New York: Taylor and Francis)
- Boischoat, A. 1958, Annales d'Astrophysique, 21, 273
- Buneman, O. & Storey, L. R. O. 1985, Simulations of fusion plasmas by A 3-D, E-M particle code, Tech. rep.
- Chen, F. 1984, Introduction to Plasma Physics and Controlled Fusion, Introduction to Plasma Physics and Controlled Fusion No. sv. 1 (Springer)
- Chernov, G., Sych, R., Tan, B.-L., et al. 2016, Research in Astronomy and Astrophysics, 16, 28
- Chernov, G. P. 1976, Soviet Ast., 20, 582
- Chernov, G. P. 1990, Sol. Phys., 130, 75
- Chernov, G. P. 2006, Space Sci. Rev., 127, 195
- Chernov, G. P. 2010, Research in Astronomy and Astrophysics, 10, 821
- Chernov, G. P. 2011, Fine structure of solar radio bursts, Astrophysics and space science library No. v. 375 (Springer), OCLC: ocn723107988
- Chernov, G. P. 2018, arXiv e-prints, arXiv:1807.08818

- Chernov, G. P., Fomichev, V. V., & Sych, R. A. 2018, *Geomagnetism and Aeronomy*, 58, 394
- Chernov, G. P., Klein, K. L., Zlobec, P., & Aurass, H. 1994, *Sol. Phys.*, 155, 373
- Chernov, G. P., Sych, R. A., Meshalkina, N. S., Yan, Y., & Tan, C. 2012, *A&A*, 538, A53
- Chernov, G. P., Yan, Y.-H., & Fu, Q.-J. 2014, *Research in Astronomy and Astrophysics*, 14, 831
- Courant, R., Friedrichs, K., & Lewy, H. 1928, *Mathematische Annalen*, 100, 32
- Dabrowski, B. P., Krankowski, A., Blaszkiewicz, L., & Rothkaehl, H. 2016, *Acta Geophysica*, 64
- Dabrowski, B. P., Rudawy, P., Falewicz, R., Siarkowski, M., & Kus, A. J. 2005, *A&A*, 434, 1139
- Dawson, J. M. 1983, *Reviews of Modern Physics*, 55, 403
- Denisse, J. F., Boischot, A., & Pick-Gutmann, M. 1960, in *Space Research*, 637
- Dory, R. A., Guest, G. E., & Harris, E. G. 1965, *Physical Review Letters*, 14, 131
- Droege, F. 1977, *A&A*, 57, 285
- Dulk, G. A. 1985, *ARA&A*, 23, 169
- Dulk, G. A., Melrose, D. B., & White, S. M. 1979, *ApJ*, 234, 1137
- Elgaroy, E. O. 1977, *Oxford Pergamon Press International Series on Natural Philosophy*, 90
- Elgarøy, Ø. 1961, *Astrophysica Norvegica*, 7, 123
- ESO. 2019, *ALMA Receiver Bands*, <https://www.eso.org/public/czechrepublic/teles-instr/alma/receiver-bands/>
- Fitzpatrick, R. 2015, *Plasma physics: an introduction* (CRC Press)
- Fleishman, G. D. & Mel'nikov, V. F. 1998, *Physics Uspekhi*, 41, 1157
- Ginzburg, V. L. & Zhelezniakov, V. V. 1958, *Soviet Ast.*, 2, 653
- Ginzburg, V. L. & Zhelezniakov, V. V. 1959, in *IAU Symposium, Vol. 9, URSI Symp. 1: Paris Symposium on Radio Astronomy*, ed. R. N. Bracewell, 574
- Hankins, T. H. & Eilek, J. A. 2007, *ApJ*, 670, 693
- Hey, J. S. 1946, *Nature*, 157, 47
- HiRAS. 2012, *Hiraiso Radio Spectrograph*, <http://sunbase.nict.go.jp/solar/denpa/>
- Hockney, R. W. & Eastwood, J. W. 1981, *Computer Simulation Using Particles*
- Jiříčka, K., Karlický, M., Mészárosóvá, H., & Snížek, V. 2001, *A&A*, 375, 243
- Kaneda, K., Misawa, H., Iwai, K., et al. 2018, *ApJ*, 855, L29
- Kaneda, K., Misawa, H., Iwai, K., Tsuchiya, F., & Obara, T. 2015, *ApJ*, 808, L45
- Karlický, M. 2013, *A&A*, 552, A90

- Karlický, M. 2014, *A&A*, 561, A34
- Karlický, M. & Bárta, M. 2011, in *IAU Symposium*, Vol. 274, *Advances in Plasma Astrophysics*, ed. A. Bonanno, E. de Gouveia Dal Pino, & A. G. Kosovichev, 252–254
- Karlický, M., Mészáros, H., & Jelínek, P. 2013, *A&A*, 550, A1
- Karlický, M. & Yasnov, L. V. 2015, *A&A*, 581, A115
- Karlický, M. & Yasnov, L. V. 2018, *ApJ*, 867, 28
- Kong, X., Chen, Y., Guo, F., et al. 2015, *ApJ*, 798, 81
- Kruger, A. 1979, *Introduction to Solar Radio Astronomy and Radio Physics*, Geophysics and astrophysics monographs No. 16 (Dordrecht. Holland: D. Reidel publishing company)
- Kuijpers, J. 1975, *Sol. Phys.*, 44, 173
- Kuijpers, J. 1980, in *IAU Symposium*, Vol. 86, *Radio Physics of the Sun*, ed. M. R. Kundu & T. E. Gergely, 341–360
- Kuznetsov, A. A. 2005, *A&A*, 438, 341
- Kuznetsov, A. A. 2006, *Sol. Phys.*, 237, 153
- Kuznetsov, A. A. & Kontar, E. P. 2015, *Sol. Phys.*, 290, 79
- Kuznetsov, A. A. & Tsap, Y. T. 2007, *Sol. Phys.*, 241, 127
- LaBelle, J., Treumann, R. A., Yoon, P. H., & Karlický, M. 2003, *ApJ*, 593, 1195
- Laptukhov, A. I. & Chernov, G. P. 2009, *Plasma Physics Reports*, 35, 160
- Ledenev, V. G., Yan, Y., & Fu, Q. 2006, *Sol. Phys.*, 233, 129
- Lesovoi, S., Altyntsev, A., Kochanov, A., et al. 2017, *Solar-Terrestrial Physics*, 3, 3
- LOFAR. 2019, LOFAR, <http://www.lofar.org/>
- Matsumoto, H. & Omura, Y. 1993, *Computer space plasma physics: simulation techniques and software*, Terra Scientific Pub. Co, p.305
- McLean, D. J. 1959, *Australian Journal of Physics*, 12, 404
- Melrose, D. B. 1980, *Space Sci. Rev.*, 26, 3
- Melrose, D. B. 1983, *Sol. Phys.*, 87, 359
- Melrose, D. B. 1987, *Sol. Phys.*, 111, 89
- Melrose, D. B. 1991, *ApJ*, 380, 256
- NRA. 2019, Nançay Radio Heliograph – Radiotation de astronomie de Nançay , <https://www.obs-nancay.fr/-Radioheliographie-.html>
- Ondřejov radiospectrograph. 2018, Ondřejov solar radio archive RT5 (0.8-2.0 GHz) 2017, http://www.asu.cas.cz/~radio/rt5_2018.htm

- Panchenko, M., Rošker, S., Rucker, H. O., et al. 2018, *A&A*, 610, A69
- Panchenko, M., Rucker, H. O., Kaiser, M. L., et al. 2010, *Geophys. Res. Lett.*, 37, L05106
- Payne-Scott, R. & Little, A. G. 1951, *Australian Journal of Scientific Research A Physical Sciences*, 4, 508
- Raoult, A., Mangeney, A., & Vlahos, L. 1990, *A&A*, 233, 229
- Reber, G. 1944, *ApJ*, 100, 279
- Reid, H. A. S. & Kontar, E. P. 2018a, *A&A*, 614, A69
- Reid, H. A. S. & Kontar, E. P. 2018b, *ApJ*, 867, 158
- Reiner, M. J., Karlický, M., Jiříčka, K., et al. 2000, *ApJ*, 530, 1049
- Roberts, B., Edwin, P. M., & Benz, A. O. 1984, *ApJ*, 279, 857
- Rosenberg, H. & Tarnstrom, G. 1972, *Sol. Phys.*, 24, 210
- Shaposhnikov, E. V., Zaitsev, V., & Litvinenko, G. 2018, *Journal of Geophysical Research: Space Physics*
- SKA. 2019, Square Kilometer Array, <https://www.skatelescope.org/>
- Slottje, C. 1972, *Sol. Phys.*, 25, 210
- Slottje, C. 1982, PhD thesis, Utrecht, Rijksuniversiteit
- Southworth, G. 1945, *Journal of the Franklin Institute*, 239, 285
- Staehli, M. & Magun, A. 1986, *Sol. Phys.*, 104, 117
- Sturrock, P. A., Kaufman, P., Moore, R. L., & Smith, D. F. 1984, *Sol. Phys.*, 94, 341
- Tan, B. 2010, *Astrophys. Space Sci.*, 325, 251
- Tan, B., Tan, C., Zhang, Y., Mészáros, H., & Karlický, M. 2014, *ApJ*, 780, 129
- Tan, B., Yan, Y., Tan, C., & Liu, Y. 2007, *ApJ*, 671, 964
- Tan, B., Yan, Y., Tan, C., Sych, R., & Gao, G. 2012, *ApJ*, 744, 166
- Thejappa, G. 1991, *Sol. Phys.*, 132, 173
- Tidman, D. A. & Dupree, T. H. 1965, *Physics of Fluids*, 8, 1860
- Treumann, R. A., Guedel, M., & Benz, A. O. 1990, *A&A*, 236, 242
- Tsytoich, V. N. 1966, *Soviet Physics Uspekhi*, 9, 370
- Vasanth, V., Umapathy, S., Vršnak, B., Žic, T., & Prakash, O. 2014, *Sol. Phys.*, 289, 251
- Villasenor, J. & Buneman, O. 1992, *Computer Physics Communications*, 69, 306
- Vitkevich, V. V. & Gorelova, M. V. 1960, *AZh*, 37, 622

- VLA. 2019, Very Large Array - National Radio Astronomy Observatory, <https://public.nrao.edu/telescopes/vla/>
- Wang, M. & Xie, R.-x. 2000, *Chinese Astron. Astrophys.*, 24, 95
- White, S. M. 2001, *Stellar Coronae in the Chandra and XMM-Newton Era ASP Conference Series*, 12
- Wild, J. P. 1951, *Australian Journal of Scientific Research A Physical Sciences*, 4, 36
- Wild, J. P., Sheridan, K. V., & Neylan, A. A. 1959, *Australian Journal of Physics*, 12, 369
- Wild, J. P., Smerd, S. F., & Weiss, A. A. 1963, *ARA&A*, 1, 291
- Winglee, R. M. & Dulk, G. A. 1986, *ApJ*, 307, 808
- Yasnov, L. V. & Karlický, M. 2004, *Sol. Phys.*, 219, 289
- Yu, S., Nakariakov, V. M., & Yan, Y. 2016, *ApJ*, 826, 78
- Zaitsev, V. V. & Stepanov, A. V. 1983, *Sol. Phys.*, 88, 297
- Zaitsev, V. V., Stepanov, A. V., & Sterlin, A. M. 1985, *Soviet Astronomy Letters*, 11, 192
- Zhang, P. J., Wang, C. B., & Ye, L. 2018, *A&A*, 618, A165
- Zhelezniakov, V. V. 1997, *Radiation in astrophysical plasmas* [in Russian]; Original Russian Title — “Izlucheniye v astrofizicheskoy plasme”
- Zhelezniakov, V. V. & Zaitsev, V. V. 1975, *A&A*, 39, 107
- Zhelezniakov, V. V. & Zlotnik, E. I. 1975a, *Sol. Phys.*, 43, 431
- Zhelezniakov, V. V. & Zlotnik, E. I. 1975b, *Sol. Phys.*, 44, 447
- Zhelezniakov, V. V. & Zlotnik, E. Y. 1975c, *Sol. Phys.*, 44, 461
- Zheleznyakov, V. V., Zlotnik, E. Y., Zaitsev, V. V., & Shaposhnikov, V. E. 2016, *Physics Uspekhi*, 59, 997
- Zlotnik, E. Y. 2009, *Central European Astrophysical Bulletin*, 33, 281
- Zucca, P., Morosan, D. E., Rouillard, A. P., et al. 2018, *A&A*, 615, A89

